Doctoral Dissertation
博士論文

Study of Semiclassical Periodic Orbits in Kinetically Constrained Quantum Many-Body Systems

（運動論的拘束のある量子多体系における半古典的周期軌道の研究）

A Dissertation Submitted for the Degree of Doctor of Philosophy
December 2021

令和 3 年 12 月博士 (理学) 申請

Department of Physics, Graduate School of Science,
The University of Tokyo

東京大学大学院理学系研究科物理学専攻

Hayate Nakano

中野 颯

Acknowledgement

I am deeply grateful to my supervisor, Synge Todo, for his valuable suggestions, comments, discussions, and assistance in my life in graduate school. His deep knowledge and insights about computational physics and condensed matter physics were essential for my research.

I would like to thank all my collaborators during my doctoral program, Takashi Mori, Tatsuhiko Shirai, Professor Hosho Katsura, and Hong Yang. Dr. Mori and Dr. Shirai gave me a lot of knowledge and advice as a leading professional of non-equilibrium quantum many-body physics and statistical mechanics. Professor Katsura taught me a ton of excellent knowledge of quantum many-body scar through discussions and his wonderful web page.

I also appreciate the help of the other members of the Todo group. Project Associate Professor Tsuyoshi Okubo gave me many advice and crucial questions as a professional of statistical physics and tensor network algorithms. His advice improved my understanding of the topics. I would like to thank my colleagues and staff in the Todo group, Assistant Professor Hidemaro Suwa, Visiting Researcher Daiki Adachi, Takuya Yamamoto, Chihiro Kondo, Ruixiao Cao, RuQing Xu, Taito Kutsuzawa, and Xun Zhao. I discussed various topics with them.

I am grateful to Assistant Professor Ken Nakanishi, my former colleague in the Todo group. I made many work calls with him when I worked from home during the COVID-19 pandemic.

I also extend my gratitude to all the people who have been involved with me, such as secretariats of the department of science, secretaries in the Todo group, alumni of the Todo group, and my friends. I would not have passed my research life without their support.

Emeritus Professor Seiji Miyashita taught me the basics of being a researcher as a supervisor of my master's program. I would like to express my gratitude to him once again.

I acknowledge the financial support of the Advanced Leading Graduate Course for Photon Science (ALPS). Furthermore, I express my appreciation to Professor Masato Koashi as a mentor from the ALPS program.

Finally, I would like to express my most profound appreciation to my parents, Masaru Nakano and Akiko Nakano. Without their support and encouragement, I would not have written this thesis. I express my heartfelt gratitude for their support.

Abstract

Thermalization is one of the essential hypotheses in thermodynamics, which asserts that a macroscopic system relaxes to a thermal equilibrium state characterized by a few thermodynamic variables. The eigenstate thermalization hypothesis (ETH) gives a microscopic justification of the thermalization and has been believed to hold for non-integrable quantum many-body systems. Quantum many-body scar (QMBS), a new kind of ETH-violating mechanism, refers to the phenomenon of non-integrable Hamiltonians having non-thermal eigenstates in the middle of the spectrum.

From the viewpoint of quantum-classical correspondence, periodic orbits play an essential role in the QMBS. In the previous studies, a semiclassical dynamical system derived by the time-dependent variational principle (TDVP) for the matrix product state (MPS) has been discussed. However, the bond dimension of the MPS was very restricted, and there was no extrapolation for the thermodynamic limit.

In this thesis, we solve this problem by developing an algorithm to search for periodic orbits for a dynamical system obtained by TDVP for MPS with general bond dimensions. By applying our algorithm to the PXP model, we find the existence of periodic orbits on a general-bond-dimensional manifold. Our results also suggest that the periodic orbits are meaningful in the infinite-bond-dimension limit. Furthermore, we point out that the non-thermal energy eigenstates can be approximately reconstructed by taking their superposition. We quantitatively discuss the accuracy by evaluating the energy variance. This fact eliminates the arbitrariness of a choice of a variational manifold and allows us to discuss QMBS more accurately and mechanically from the semiclassical approximation and quantum-classical correspondence. We expect this method to be applied to a broad class of many-body Hamiltonians exhibiting QMBS and to contribute significantly to a deeper understanding of ETH and QMBS.

Contents

List of Figures

1 | Introduction

Deriving thermodynamics, a macroscopic empirical law, from quantum mechanics, a microscopic fundamental law, is one of the crucial challenges in physics. Thermalization is one of the essential hypotheses in thermodynamics, which asserts that a macroscopic system relaxes to a thermal equilibrium state characterized by a few thermodynamic variables.

In recent years, the thermalization of isolated quantum many-body systems has been studied in detail [1–5]. These researches have been motivated by the development of experimental techniques in cold atom systems, which made it possible to observe the thermalization directly [6–9]. In a theoretical aspect, the eigenstate thermalization hypothesis (ETH) has been reaffirmed and well investigated [1, 10–12].

ETH claims that the expectation values of local observables are indistinguishable between the energy eigenstates and the microcanonical ensembles. It is known that ETH provides a sufficient condition of thermalization [13, 14]. Since it is tough to prove ETH theoretically for a specific model, verification of ETH has been done by numerical experiments by exact diagonalization and finite-size scaling [15, 16].

As a result, it has been confirmed that ETH holds in most cases except integrable systems [1, 17–20] and strongly disordered many-body localized systems (MBL) [5, 21–26]. Such ETH-violating systems have an extensive number of (quasi-)local conserved quantities, which restrict the time evolution of the systems. Therefore, the system relaxes to a state called the generalized Gibbs ensemble, which is characterized by a set of generalized temperatures corresponding to each conserved quantity [27–30].

On the other hand, it has been believed that ETH holds for non-integrable quantum many-body systems which have no local conserved quantities except a few arising from global symmetry. However, T. Mori and N. Shiraishi showed that it is possible to construct a quantum many-body model that is non-integrable and yet violates ETH [31, 32]. Through experiments on cold atom systems, H. Bernien et al. discovered a non-integrable system called the PXP model, which does not show thermalization but exhibits long-lived oscillations when the dynamics starts from some specific initial states [33]. The PXP model also has ETH-violating eigenstates in the middle of the spectrum. A deep relationship among these models has been discovered [34]. Such quantum many-body systems, non-integrable and containing a few ETH-violating states, are called the quantum many-body scar (QMBS) [35–38] and have attracted interest in recent years [39–66].

In QMBS, kinetic constraints play an important role. For example, the PXP model is derived by taking the strong limit of the nearest-neighbor interaction called the Rydberg blockade [33, 67–71], in which atoms can excite only when both atoms in the neighboring sites are in the ground state. It is also known that kinetic constraints can produce another kind of ergodicity breaking. Fractons [72–74], quasiparticles with restricted motion, can shutter the Hilbert space and make them into fragments [75–83]. This fragmentation phenomenon can induce strong ergodicity breaking similar to MBL. These examples suggest that not only the conserved quantities but also the dynamic constraints can affect the thermalization phenomena.

Kinetic constraints affect the relaxation phenomena also in classical many-body systems.

Kinetically constrained models (KCMs), classical stochastic many-body models with constraints, have been investigated in detail as models of glasses [84]. Grassy slow relaxation and jamming transitions have been found in KCMs. Some quantum many-body models have been derived inspired by KCMs, and anomalous thermalization has been discovered [85–92]. A better understanding of the relationship between classical and quantum constraints will help us understand thermalization deeply.

The quantum-classical correspondence becomes even more critical in QMBS since the quantum (*not* many-body) scar, the origin of the name QMBS, is a quantum phenomenon of a classically chaotic system [93, 94]. Let us quantize the Hamiltonian of a single-particle classically chaotic system like a stadium billiard [95] and consider the motion of the wave packet. The typical wave packet spreads over the whole space with time evolution and eventually reaches a uniform probability distribution. However, it has been discovered that there are some peculiar initial states for which the wave packets exhibit extremely long-lived oscillations, corresponding to unstable periodic orbits [96] of classical systems. This phenomenon is related to a few special energy eigenstates with high probability density around the periodic orbit.

Although the anomalous dynamics of the PXP model is similar to the quantum scar, it is a non-trivial question of whether physical correspondence exists beyond mere analogy. In order to answer this, it is necessary to derive the corresponding classical dynamical system for the PXP model and to understand QMBS from the properties of the dynamical system. For this task, the tensor-network-based approach has been very successful [36, 37, 97–100].

Tensor-network (TN) states are obtained by approximating the quantum many-body states by a network of products of small tensors [101–103]. The matrix product state (MPS) is the most fundamental TN state, and its properties have been investigated in great detail. TN has been widely used in recent years both for numerical calculations and constructions of exact solutions. Of course, TN states have played an essential role in the study of QMBS. In particular, many examples of exact scar states have been constructed by using MPS [43, 47, 53, 104].

TN state can also be used as a semiclassical approximation method to extract a dynamical system from a quantum many-body system. Time-dependent variational principle (TDVP) [105–109] is a numerical method to project the original quantum dynamics onto a manifold of variational states. We can obtain semiclassical dynamics on the TN manifold by adopting TDVP [110–115]. This method has been used to study quantum many-body chaos.

For example, the Lyapunov exponents of semiclassical dynamical systems on MPS have been investigated for non-integrable and ETH satisfying one-dimensional quantum many-body systems [116]. For the PXP model, several studies have pointed out the existence of periodic orbits corresponding to the anomalous long-life oscillation in the MPS manifold, which makes the correspondence between the single-particle scar and QMBS clearer.

The derivation of semiclassical dynamical systems using TDVP is applicable for general variational states. One of the significant advantages of TN states is that the expressive ability of the variational states can be controlled by a parameter called the bond dimension. Making the bond dimension to unity corresponds to the mean-field approximation, and taking the infinite bond dimension limit reproduces the original quantum dynamics in the thermodynamic limit. It is essential to discuss the behavior in the thermodynamic limit by scaling the bond dimension. Indeed, such an analysis has been done in previous studies dealing with non-integrable systems [116, 117].

However, in the previous studies for the PXP model, the bond dimension of MPS was fixed entirely to two since MPS was constructed by applying a matrix product operator (MPO) that describes the kinetic constraints on the product state. In this thesis, we find and investigate periodic orbits in the MPS manifold with general bond dimensions and solve this problem.

For this purpose, we use the TDVP algorithm conserving non-local symmetry represented by MPO.

Compared to the analysis of the Lyapunov exponents, the search for periodic orbits in a manifold is a difficult task, having blocked previous researchers. We have solved this problem by using automatic differentiation [118–126] and continuous optimization on manifolds [122, 127]. These techniques have been actively studied in the context of machine learning in recent years. Furthermore, we directly construct the anomalous eigenstates by superposition of the obtained semiclassical periodic orbits. Then, we give a more precise interpretation of the quantum-classical correspondence.

This thesis is organized as follows. First, in Chapter 2, we review the concepts of ETH and QMBS. Although there are quite a few proposed models of QMBS and various physical mechanisms behind them, we will concentrate our discussion on the PXP model and its background. In Chapter 3, we review the TDVP algorithm for the MPS. We also review in detail the previous work in which quantum many-body chaos and QMBS were discussed by TDVP-based semiclassical analysis. In Chapter 4, we discuss details of the algorithm that we use and our results. In Chapter 5, we clarify the relations between periodic orbits and ETH-violating eigenstates by eigenstate construction. Finally, in Chapter 6, we give a summary and discuss prospects.

2 | Eigenstate Thermalization Hypothesis and Quantum Many-Body Scar

In this chapter, we review the quantum many-body scar, mainly focusing on the PXP model. In Section 2.1, we review the basics of the thermalization phenomena and its breaking in quantum many-body systems. In Section 2.2, we introduce a quantum many-body scar, a new type of counterexample of thermalization.

2.1 Thermalization of isolated quantum many-body system

In recent years, motivated by the experimental progress in cold atoms, theoretical descriptions of thermalization in isolated quantum many-body systems have been greatly developed. We review the basics about it in this section. In Section 2.1.1, we introduce the eigenstate thermalization hypothesis (ETH), which gives a sufficient condition of thermalization. We give an exact definition of ETH and discuss its consequences. In Section 2.1.2, we discuss the condition for a quantum many-body system to satisfy ETH. ETH holds for a vast class of non-integrable quantum many-body Hamiltonians. On the other hand, as a counterexample of ETH, quantum integrable systems and many-body localized systems have been well investigated. Here, we introduce the quantum many-body scar as a new type of ETH violating mechanism.

2.1.1 Eigenstate thermalization hypothesis

In quantum mechanics, thermal equilibrium states are characterized by density matrices like microcanonical ensemble or canonical ensemble. On the other hand, the time evolution of the pure state in an isolated quantum system is described by a unitary operator $\exp(-\mathrm{i}\hat{H})$, and the state is written as a time-dependent state vector. If any measurement of the system is possible, we can distinguish between these states in any case.

In thermodynamics and statistical mechanics, we are only interested in local operators and the sum of it like magnetization, density, and correlation. Thus, in the discussion of the thermalization of quantum many-body systems, we consider the time evolution of the expectation value of local operators. We divide the problem into two parts: (i) Does the expectation value of any local operator exhibit the relaxation? (ii) Are the equilibrated values equal to the thermal average?

Now, let us consider a quantum many-body Hamiltonian $\hat{H}$ and its spectral decomposition $\hat{H} = \sum_\alpha E_\alpha |\phi_\alpha\rangle\langle\phi_\alpha|$. We take an arbitrary local Hermitian operator $\hat{O}$. Eigenstate thermalization hypothesis (ETH) [1, 10–12], arguing *all* energy eigenstates in the middle of the spectrum satisfy the following equation

$$\langle\phi_\alpha|\hat{O}|\phi_\beta\rangle = \mathcal{O}(E)\delta_{\alpha,\beta} + e^{-S(E)/2} f(E,\omega) R_{\alpha,\beta}, \tag{2.1.1}$$

is known to be a sufficient condition of thermalization [4, 13]. Here, $\mathcal{O}(E)$ is a smooth function of energy consistent with the prediction of canonical ensemble. In the second term, E denotes

the average energy $(E_\alpha + E_\beta)/2$, ω denotes the energy difference $E_\alpha - E_\beta$, S denotes the thermodynamic entropy, and f denotes a size-independent smooth function exponentially decaying with ω. The last factor $R_{\alpha,\beta}$ is a random number with zero mean and unit variance. The first term corresponding to the diagonal parts is called the diagonal ETH, while the second term is called the off-diagonal ETH.

First, we consider question (i). We make the initial state $|\psi\rangle$ a superposition of energy eigenstates as $|\psi\rangle = \sum_\alpha c_\alpha |\phi_\alpha\rangle$. Here, we assume that the energy eigenvalues are non-degenerated, i.e., $\alpha \neq \beta \Rightarrow E_\alpha \neq E_\beta$. Under this assumption, the long-time average of the expectation value of $\hat{O}$ can be written as

$$\overline{O} \coloneqq \overline{\langle\psi(t)|\hat{O}|\psi(t)\rangle} = \sum_{\alpha,\beta} c_\beta^* c_\alpha \overline{e^{\mathrm{i}(E_\alpha - E_\beta)t}} \langle\phi_\alpha|\hat{O}|\phi_\beta\rangle = \sum_\alpha |c_\alpha|^2 \langle\phi_\alpha|\hat{O}|\phi_\alpha\rangle. \tag{2.1.2}$$

Here, non-diagonal terms vanish because of the oscillation. The right-hand side is called a diagonal ensemble. The relaxation is characterized by the time fluctuation defined as

$$\delta O^2 \coloneqq \overline{(\langle\psi(t)|\hat{O}|\psi(t)\rangle - \overline{O})^2} = \sum_{\alpha\neq\beta}\sum_{\gamma\neq\delta} c_\alpha^* c_\beta c_\gamma c_\delta^* \overline{e^{\mathrm{i}((E_\alpha - E_\beta)-(E_\gamma - E_\delta))t}} \langle\phi_\alpha|\hat{O}|\phi_\beta\rangle\langle\phi_\delta|\hat{O}|\phi_\gamma\rangle. \tag{2.1.3}$$

By assuming non-resonance condition

$$E_\alpha - E_\beta = E_\gamma - E_\delta \neq 0 \Rightarrow (\alpha,\beta) = (\gamma,\delta), \tag{2.1.4}$$

we can obtain

$$\delta O^2 = \sum_{\alpha\neq\beta} |c_\alpha|^2 |c_\beta|^2 |\langle\phi_\alpha|\hat{O}|\phi_\beta\rangle|^2 \leq \max_{\alpha\neq\beta} |\langle\phi_\alpha|\hat{O}|\phi_\beta\rangle|^2. \tag{2.1.5}$$

By using the off-diagonal ETH in this equation, we can conclude that the time fluctuation is exponentially small with respect to the system size in many cases. Thus, the off-diagonal ETH is a sufficient condition of (i).

Hereafter, we assume that the energy variance of the initial state is small. Then, combining the diagonal ETH and Eq. (2.1.2), we can conclude that the equilibrated value is nothing but the thermal equilibrium value. This is the answer to (ii).

The diagonal ETH means that each energy eigenstate is equivalent to the canonical state for any measurement of local observables. We consider a small subsystem X and its complement X^c. The diagonal ETH suggests that

$$\mathrm{Tr}_{X_c}[|\phi_\alpha\rangle\langle\phi_\alpha|] \approx \mathrm{Tr}_{X_c}[\hat{\rho}_{\mathrm{mc}}] \approx \frac{e^{-\beta\hat{H}_X}}{\mathrm{Tr}_X[e^{-\beta\hat{H}_X}]} \tag{2.1.6}$$

holds for any small X. Here, $\hat{H}_X$ denotes a part of $\hat{H}$ acting on X. The density operator $\hat{\rho}_{\mathrm{mc}}$ denotes the microcanonical ensemble corresponding to the energy shell $E_\alpha - \Delta E < E < E_\alpha$, where ΔE is large in the microscopic scale and small in the macroscopic scale. The effective temperature β is determined by the energy E_α. By taking the von Neumann entropy of this equation, we can obtain a correspondence between entanglement entropy of the pure state and the thermal entropy of the reduced density matrix. For highly excited states, $\beta \to 0$ holds, and the entropy of the right-hand side scales proportionally to the volume of X. Thus, ETH predicts a volume law for the entanglement entropy of highly excited eigenstates.

	ETH	Ergodicity	Entanglement	Level statistics
Non-integrable	All	Yes	Volume	Wigner-Dyson
QMBS	Almost All	Weak	Volume/SubVolume	Wigner-Dyson
Integrable	Almost All	No	Volume/SubVolume	Poisson
MBL	No	No	Area	Poisson

Table 2.1: Taxonomy of quantum many-body Hamiltonians.

2.1.2 ETH breaking in integrable systems

The relation between ETH and integrability is essential. It has been believed that the ETH holds for a broad class of non-integrable quantum many-body systems. The results of numerical calculations for several non-integral models strongly suggest the ETH [15, 16].

Conversely, integrable systems like a non-interacting system or a Bethe-ansatz solvable system do not satisfy ETH. Almost all eigenstates satisfy the ETH in these systems, but not all eigenstates. Such behavior is called the weak ETH and proved for a broad class of translational invariant quantum many-body systems [19, 128, 129]. The integrable system is mainly characterized by the existence of an extensive number of conserved quantities and the Poisson statistics of its energy level spacing. In contrast, those of non-integrable systems obey the Wigner-Dyson statistics.

Another counterexample of ETH is many-body localization (MBL) in the system with strong disorder [5, 21–26]. MBL system also has conserved quantities called l-bit and shows Poisson level statistics. Integrable and MBL systems also violate thermalization, i.e., show strong ergodicity breaking.

Non-integrable quantum many-body systems with quantum many-body scars (QMBS) are a new type of ETH-violating system [35–38]. These models show characteristic relaxation phenomena depending on the initial state, called weak ergodicity breaking. We discuss it in the next section. The existence of QMBS means that non-integrability is not a sufficient condition of ETH. In Table 2.1, we show the characters of each system.

2.2 Quantum many-body scar

In this section, we review the recent development of the theory of quantum many-body scars (QMBS). Today, roughly speaking, QMBS is defined as the quantum many-body system which violates ETH but is neither integrable nor many-body localized. Many models meeting this definition have been found these days. Here, we avoid discussing the general theory of QMBS and focus on the PXP model [104, 130–134].

The PXP model is one of the earliest models of QMBS. In the first place, the name of QMBS comes from the analogy between the PXP model and quantum scar, a phenomenon of the quantum system obtained by quantizing a classically chaotic dynamical system.

In Section 2.2.1, we introduce the PXP model Hamiltonian and discuss the detail like the scarred eigenstate, weak ergodicity breaking, and periodic oscillation. In Section 2.2.2, we discuss the relation between QMBS and quantum scar by using semiclassical approximation.

2.2.1 PXP model

The PXP model is a quantum many-body system that is non-integrable but breaks thermalization. It was derived as an effective Hamiltonian of the Rydberg-atom system in experiments. Here, we explain the derivation of the PXP model from the original experimental Hamiltonian

for one-dimensional Rydberg-atom chains. The state at site i is either the local ground state $|\bigcirc\rangle_i$ or the excited state $|\bullet\rangle_i$. The Hamiltonian of the Rydberg-atom system can be written as

$$\hat{H}_{\mathrm{Ryd}} = \sum_{j=1}^{N} \left(\frac{\Omega}{2} (|\bigcirc\rangle\langle\bullet|_i + |\bullet\rangle\langle\bigcirc|_i) - \Delta |\bullet\rangle\langle\bullet|_i \right) + \sum_{i<j}^{N} (V_{i,j} |\bullet\rangle\langle\bullet|_i \otimes |\bullet\rangle\langle\bullet|_j), \tag{2.2.1}$$

where Ω denotes the Rabi frequency, Δ denotes the detuning parameter, and $V_{i,j} \propto |i-j|^{-6}$ denotes the van der Waals interaction. By taking the limit $V = V_{i,i+1} \gg \Omega$ and $\Delta = 0$, we can rewrite the Hamiltonian as

$$\frac{1}{V} \hat{H}_{\mathrm{Ryd}} = \sum_i (|\bullet\rangle\langle\bullet|_i \otimes |\bullet\rangle\langle\bullet|_{i+1}) + \frac{\Omega}{2V} \sum_i (|\bigcirc\rangle\langle\bullet|_i + |\bullet\rangle\langle\bigcirc|_i). \tag{2.2.2}$$

The first term, which counts the number of the adjacent excited state, is a dominant term of this Hamiltonian. Here, let us consider the effective low-energy dynamics. The low-energy subspace is the space without adjacent excitation. This phenomenon is called Rydberg blockade (RB) and represented by the projector

$$\hat{\mathcal{P}}_{\mathrm{RB}} = \prod_j (\hat{1}_{j,j+1} - |\bullet\rangle\langle\bullet|_j \otimes |\bullet\rangle\langle\bullet|_{j+1}). \tag{2.2.3}$$

We can obtain the low-energy effective Hamiltonian by using this projector as

$$\begin{aligned} \hat{H}_{\mathrm{PXP}} &= \hat{\mathcal{P}}_{\mathrm{RB}} \left(\sum_i |\bigcirc\rangle\langle\bullet|_i + |\bullet\rangle\langle\bigcirc|_i \right) \hat{\mathcal{P}}_{\mathrm{RB}} \\ &= \sum_j |\bigcirc\rangle\langle\bigcirc|_{j-1} \otimes (|\bigcirc\rangle\langle\bullet|_j + |\bullet\rangle\langle\bigcirc|_j) \otimes |\bigcirc\rangle\langle\bigcirc|_{j+1} \end{aligned} \tag{2.2.4}$$

We can check that the Hamiltonian of the PXP model is non-integrable and chaotic in the aspect of level statistics [99]. However, this Hamiltonian does not satisfy ETH. Thus, this is a new type of ETH violation with neither integrability nor disorder.

Scarred eigenstates

Here, we discuss the structure of the eigenstate of the PXP model Hamiltonian. In Fig. 2.1, we show the scattering plot of the eigenstate obtained by the exact diagonalization of a finite-size system.

In Fig. 2.1a, we show the comparison of the expectation value of a local operator. We can see that almost all eigenstates have expectation values close to the one obtained from the canonical ensemble. Here, the effective inverse temperature of the canonical ensemble is determined by the energy E. In Ref. [132], it is also shown that the probability distribution of differences of the expectation values between eigenstates adjacent in eigenvalue becomes narrow around zero in the thermodynamic limit. The average of the differences decays with an exponential with the system size. Thus, the eigenstates distributed around the canonical ensemble prediction in Fig. 2.1a would concentrate in the thermodynamic limit. This phenomenon is expected by the diagonal ETH. Simultaneously, we can see a band of special eigenstates away from the blue line marked by red crosses even in the middle of the spectrum. We call these exceptional eigenstates scarred eigenstates or scar states. The existence of scarred eigenstates indicates that the strong ETH does not hold in the PXP model.

In Fig. 2.1b, we show the bipartite entanglement entropy (EE) of the eigenstates. We can see that the EE of scarred eigenstates is smaller than that of non-scarred eigenstates. By using finite-size scaling analysis, we can see that the EE of scarred eigenstates shows logarithmic scaling with the system size instead of the volume law predicted by ETH.

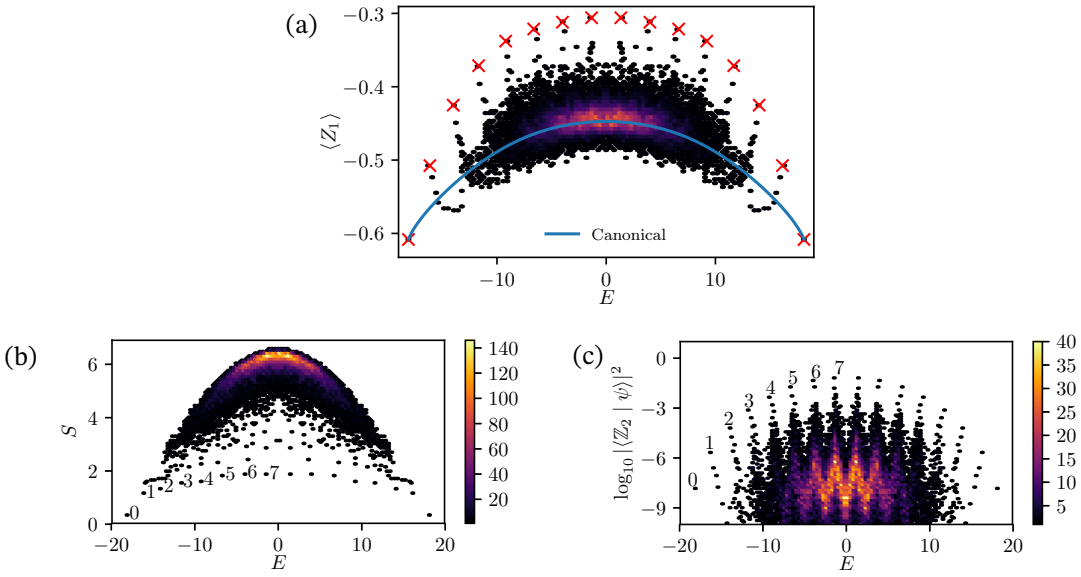

Figure 2.1: Scattering plots of eigenstates of the PXP model obtained by exact diagonalization of $N = 30$ system. Color scales denote the density of the eigenstates. (a) Comparison of expectation values of a local operator $\hat{Z}_1 = |\bullet\rangle\langle\bullet|_1 - |\circ\rangle\langle\circ|_1$ between the canonical ensembles (blue line) and the eigenstates (dots). A series of special eigenstates with equal energy separation, which we call scarred eigenstates, are indicated by crosses. (b) Bipartite entanglement entropies of the eigenstates. (c) Overlaps with $|\mathbb{Z}_2\rangle$ state defined in Eq. (2.2.5). In (b) and (c), scarred eigenstates are labeled by common integers 0, ..., 7. Reprinted figure with permission from Ref. [132]. Copyright © (2018) by the American Physical Society.

We can also see the equal energy separation between the scarred eigenstates. This is another essential point of QMBS. This "tower" structure breaks the non-resonance condition defined in Eq. (2.1.4) and causes a long-life coherent oscillation.

Weak ergodicity breaking and periodic oscillation

This violation of ETH actually affects the relaxation dynamics of the PXP model. Now, we define three kinds of product states as

$$|\mathbf{0}\rangle := |\circ_1\circ_2\circ_3\circ_4 \ldots\rangle, \quad |\mathbb{Z}_2\rangle := |\circ_1\bullet_2\circ_3\bullet_4 \ldots\rangle, \quad |\mathbb{Z}_2'\rangle := |\bullet_1\circ_2\bullet_4\circ_3 \ldots\rangle. \tag{2.2.5}$$

As we can see in Fig. 2.1c, $|\mathbb{Z}_2\rangle$ states have a large overlap with the scarred eigenstates. In Fig. 2.2, we show the time evolution of the expectation value of local operators with different initial states $|\mathbf{0}\rangle$ and $|\mathbb{Z}_2\rangle$. We can see the rapid relaxation towards the thermal value when we take the initial state $|\mathbf{0}\rangle$. In contrast, the system shows long-life oscillations from the initial state $|\mathbb{Z}_2\rangle$. We can see that non-local quantities like EE also show oscillating phenomena. Although the EE has a slowly increasing term, its speed is very slow compared to typical quantum many-body dynamics. In other words, this oscillation occurs in a low-entangled "classical" regime. This long-life oscillation is what was initially found in the Rydberg-atom experiment [33]. These results suggest that the system violates thermalization only when starting from some special initial states. Thus, this phenomenon is called weak ergodicity breaking in contrast with strong (initial-state independent) ergodicity breaking occurs in integrable systems.

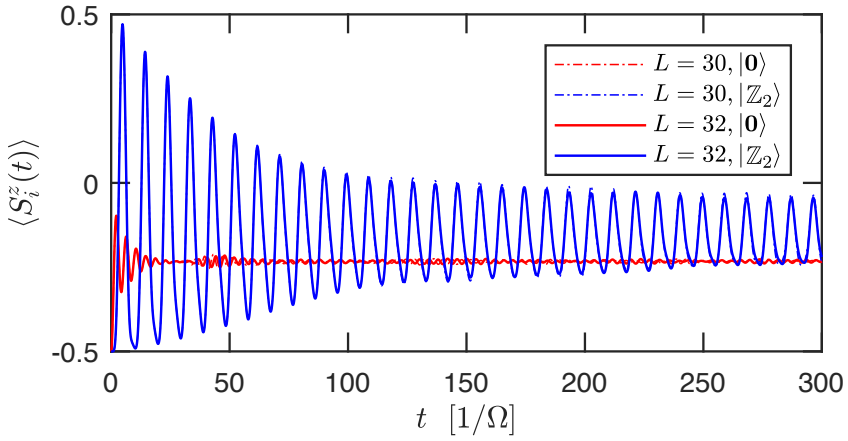

Figure 2.2: Time evolutions of the PXP model with two kinds of initial states. Here S_i^z denotes $(|\bullet\rangle\langle\bullet|_i - |\circ\rangle\langle\circ|_i)/2$ and Ω denotes the global energy scale. The Hamiltonian defined in Eq. (2.2.4) is reproduced by taking $\Omega = 2$. Reprinted figure with permission from Ref. [99]. The expectation value shows the long-life oscillation only when the dynamics starts from the special initial state $|\mathbb{Z}_2\rangle$, which has a large overlap with the scarred eigenstates. Copyright © (2018) by the American Physical Society.

2.2.2 Quantum scar and classical periodic orbits

The PXP model has two peculiar properties, long-lived periodic oscillations and a few non-thermal eigenstates, which are related to each other by the large overlap with the special initial state $|\mathbb{Z}_2\rangle$ and the scarred eigenstates. A similar relationship has been known in the research of single-particle quantum chaos [135] as the quantum scar [93, 94, 136, 137]. The name of quantum many-body scar originates from it.

Quantum scar is a phenomenon of the eigenstate properties of a single-particle quantum system obtained by quantizing a chaotic system. Although almost all highly excited eigenstates of this kind of system show the uniformly distributed probability distribution, we can find a few exceptional eigenstates which have a high probability around the unstable periodic orbits of the corresponding classical system. In the original paper on the quantum scar [93], the author considered a free particle in the stadium billiards. We define the set of coordinates in the billiards as Ω. By canonical quantization, we can obtain its stationary-state Schrödinger equation as

$$-\hbar^2\Delta\psi(q) = \lambda\psi(q), \quad q \in \partial\Omega \Rightarrow \psi(q) = 0. \tag{2.2.6}$$

In Fig. 2.3, we show the probability distribution of the result of the Schrödinger equation. We discretize the space into 200×100 and add a potential of 10^6 in the complement of Ω to emulate the boundary condition. We take two eigenstates from the middle of the spectrum. Typically, the probability distribution of the eigenstate is uniformly distributed as in the upper plot. However, we can find some special eigenstates with clear patterns like the lower plot. The area with a high probability overlaps with the short-period periodic orbits of the original classical system depicted by the green arrow. Thus, this phenomenon can be regarded as a "scar" of classical periodic orbits on the quantum eigenstate.

We can see the analogy between quantum scar and the phenomenon of the PXP model, existence of a few number of special eigenstates and the corresponding periodic phenomenon. However, in contrast to the quantum scar of the single-particle system, where the corresponding classical system is obtained by the $\hbar \to 0$ limit, there is no simple way to obtain the corresponding classical system of the PXP model. Thus, it is a problem whether the QMBS can be

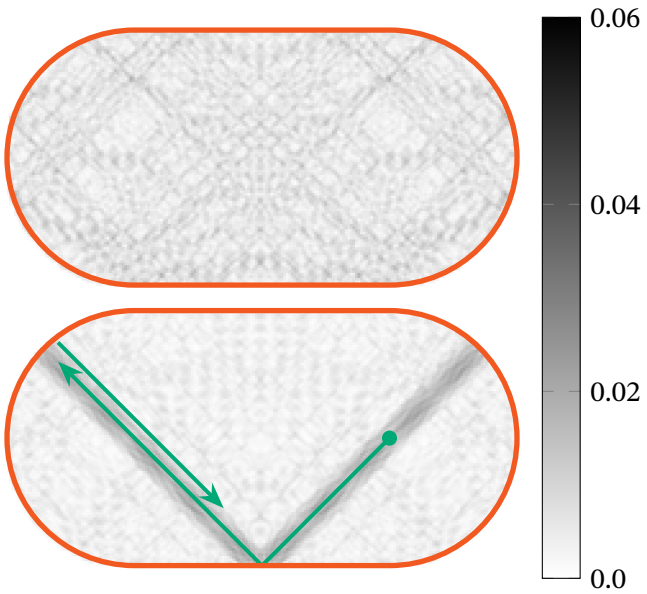

Figure 2.3: Quantum scar in stadium billiard system. The upper plot is the probability distribution of typical eigenstate obtained by solving Eq. (2.2.6). The lower plot is the probability distribution of scar. The pattern in the scar overlap with the unstable periodic orbit of the original classical system denoted by the green arrow.

understood in the same manner of the quantum scar. Here, we introduce previous researches approaching this problem by deriving a semiclassical dynamical system from the quantum Hamiltonian, following Ref. [99].

Let us consider a translational invariant product state with a two-site unit cell. Then, the state can be written as

$$|\varphi(\{\tilde{\theta}\}_{\mathrm{o,e}},\{\widetilde{\phi}\}_{\mathrm{o,e}})\rangle = \bigotimes_{j=1}^{N} \exp\left(\mathrm{i}\widetilde{\phi}_{\mu_j}|\bullet\rangle\langle\bullet|_j\right)\exp\left(\frac{-\mathrm{i}\tilde{\theta}_{\mu_j}}{2}(|\circ\rangle\langle\bullet|_j+|\bullet\rangle\langle\circ|_j)\right)|\circ\rangle_j, \tag{2.2.7}$$

where $\mu_j = \mathrm{e/o}$ if j is even/odd. Combining this state and the matrix product operator representation of $\hat{\mathcal{P}}_{\mathrm{RB}}$

$$\hat{\mathcal{P}}_{\mathrm{RB}} = \mathrm{Tr}\left[\begin{pmatrix}|\circ\rangle\langle\circ|_1 & |\bullet\rangle\langle\bullet|_1\\ |\circ\rangle\langle\circ|_1 & 0\end{pmatrix}\begin{pmatrix}|\circ\rangle\langle\circ|_2 & |\bullet\rangle\langle\bullet|_2\\ |\circ\rangle\langle\circ|_2 & 0\end{pmatrix}\cdots\begin{pmatrix}|\circ\rangle\langle\circ|_N & |\bullet\rangle\langle\bullet|_N\\ |\circ\rangle\langle\circ|_N & 0\end{pmatrix}\right], \tag{2.2.8}$$

we can obtain the matrix product states (MPS) parameterized by four parameters $\tilde{\theta}_{\mathrm{e/o}}, \widetilde{\phi}_{\mathrm{e/o}}$ as

$$\begin{aligned}&\hat{\mathcal{P}}_{\mathrm{RB}}|\varphi(\{\tilde{\theta}\},\{\widetilde{\phi}\})\rangle\\ &= \mathrm{Tr}\left[\begin{pmatrix}\cos(\tilde{\theta}_{\mathrm{o}}/2)|\circ\rangle_1 & -\mathrm{i}e^{\mathrm{i}\widetilde{\phi}_{\mathrm{o}}}\sin(\tilde{\theta}_{\mathrm{o}}/2)|\bullet\rangle_1\\ \cos(\tilde{\theta}_{\mathrm{o}}/2)|\circ\rangle_1 & 0\end{pmatrix}\begin{pmatrix}\cos(\tilde{\theta}_{\mathrm{e}}/2)|\circ\rangle_2 & -\mathrm{i}e^{\mathrm{i}\widetilde{\phi}_{\mathrm{e}}}\sin(\tilde{\theta}_{\mathrm{e}}/2)|\bullet\rangle_2\\ \cos(\tilde{\theta}_{\mathrm{e}}/2)|\circ\rangle_2 & 0\end{pmatrix}\cdots\right].\end{aligned} \tag{2.2.9}$$

By using a gauge transformation, inserting a product of the invertible matrix and its inverse XX^{-1} between two sites, we can obtain another MPS representation which is normalized in the thermodynamic limit

$$\begin{aligned}&|\psi(\{\theta\},\{\phi\})\rangle\\ &= \mathrm{Tr}\left[\begin{pmatrix}\cos(\theta_{\mathrm{o}}/2)|\circ\rangle_1 & -\mathrm{i}e^{\mathrm{i}\phi_{\mathrm{o}}}\sin(\theta_{\mathrm{o}}/2)|\bullet\rangle_1\\ |\circ\rangle_1 & 0\end{pmatrix}\begin{pmatrix}\cos(\theta_{\mathrm{e}}/2)|\circ\rangle_2 & -\mathrm{i}e^{\mathrm{i}\phi_{\mathrm{e}}}\sin(\theta_{\mathrm{e}}/2)|\bullet\rangle_2\\ |\circ\rangle_2 & 0\end{pmatrix}\cdots\right]\end{aligned} \tag{2.2.10}$$

satisfying

$$|\psi(\{\theta\},\{\phi\})\rangle = \hat{\mathcal{P}}_{\mathrm{RB}}|\varphi\{\tilde{\theta}\},\{\tilde{\phi}\}\rangle / \|\hat{\mathcal{P}}_{\mathrm{RB}}|\varphi\{\tilde{\theta}\},\{\tilde{\phi}\}\rangle\|. \tag{2.2.11}$$

All initial states defined in Eq. (2.2.5) can be represented in this form. Our goal is to derive the equations of motion of the parameters $\theta_{\mathrm{e/o}}$ and $\phi_{\mathrm{e/o}}$ that imitate the Schrödinger equation and regard it as a semiclassical system corresponding to the PXP model.

For this purpose, we consider the Lagrangian introduced by Dirac [108]

$$\mathcal{L}(|\psi\rangle, |\dot{\psi}\rangle) = \frac{\mathrm{i}}{2}(\langle\psi|\dot{\psi}\rangle - \langle\dot{\psi}|\psi\rangle) - \langle\psi|\hat{H}_{\mathrm{PXP}}|\psi\rangle, \tag{2.2.12}$$

where the corresponding Euler-Lagrange equation is the Schrödinger equation. We can obtain the Lagrangian in terms of $\theta_{\mathrm{e/o}}$ and $\phi_{\mathrm{e/o}}$ by substituting $|\psi(\{\theta\},\{\phi\})\rangle$ into Eq. (2.2.12). The equations of motion of $\theta_{\mathrm{e/o}}$ and $\phi_{\mathrm{e/o}}$ are obtained by the Euler-Lagrange equation. This method is called the time-dependent variational principle (TDVP) [105–109], since we consider the quantum dynamics on a set of variational states parameterized by classical variables.

In the case of the PXP model, it holds that $\phi = 0 \Rightarrow \dot{\phi} = 0$. Under this condition, the energy expectation value of $|\psi(\theta_{\mathrm{e}}, \theta_{\mathrm{o}})\rangle$ is always equal to zero, and $\dot{\theta}$ can be written as $\dot{\theta}_{\mathrm{e}} = f(\theta_{\mathrm{e}}, \theta_{\mathrm{o}})$ and $\dot{\theta}_{\mathrm{o}} = f(\theta_{\mathrm{o}}, \theta_{\mathrm{e}})$ with

$$f(x,y) = 2(\tan(y/2)\sin(x/2)\cos^2(x/2) + \cos(y/2)). \tag{2.2.13}$$

The dynamics on the variational manifold

$$\frac{\mathrm{d}}{\mathrm{d}t}|\psi(\theta_{\mathrm{e}},\theta_{\mathrm{o}})\rangle = f(\theta_{\mathrm{e}},\theta_{\mathrm{o}})\frac{\partial}{\partial\theta_{\mathrm{e}}}|\psi(\theta_{\mathrm{e}},\theta_{\mathrm{o}})\rangle + f(\theta_{\mathrm{o}},\theta_{\mathrm{e}})\frac{\partial}{\partial\theta_{\mathrm{o}}}|\psi(\theta_{\mathrm{e}},\theta_{\mathrm{o}})\rangle \tag{2.2.14}$$

is not perfectly equal to the true quantum dynamics $-\mathrm{i}\hat{H}_{\mathrm{PXP}}|\psi(\theta_{\mathrm{e}},\theta_{\mathrm{o}})\rangle$. We define the difference between them as the error vector

$$|\gamma\rangle \coloneqq \frac{\mathrm{d}}{\mathrm{d}t}|\psi(\theta_{\mathrm{e}},\theta_{\mathrm{o}})\rangle + \mathrm{i}\hat{H}_{\mathrm{PXP}}|\psi(\theta_{\mathrm{e}},\theta_{\mathrm{o}})\rangle, \tag{2.2.15}$$

which characterizes the accuracy of the semiclassical dynamics that we obtained. The norm of $|\gamma\rangle$ per site is called quantum leakage [98–100].

In Fig. 2.4a, we show the flow plot of the dynamics of θ. Each point on the plane represents a quantum state of the variational manifold, and the arrow means the trajectory obtained by TDVP. We mark the initial states defined in Eq. (2.2.5) by dots. The intensity of the background color denotes quantum leakage. The TDVP dynamics is accurate as long as the state is moving in a region with a small leakage, but it breaks down once it enters a region with a large leakage.

We can see the existence of a periodic orbit starting from $|\mathbb{Z}_2\rangle$ state. The existence of periodic orbits in the corresponding classical system is the key feature of the quantum scar of the single-particle system. Thus, the periodic orbit in Fig. 2.4 suggests the correspondence between the quantum scar and QMBS.

We can see that the leakage along the periodic orbits is small compared to the other states. It means that the dynamics starting from $|\mathbb{Z}_2\rangle$ stays on the low-entangled variational manifold and oscillates for a long time. This is compatible with the result shown in Fig. 2.2. We show the leakage of each point on the periodic orbit in Fig. 2.4b. On the other hand, the dynamics starting from $|\mathbf{0}\rangle$ goes to the large-leakage area immediately. It means that our TDVP-based approximation rapidly collapses in this case. This is compatible with the thermalization. Since no point in the variational manifold can represent a thermal equilibrium state, the state must escape from the manifold to exhibit the thermalization.

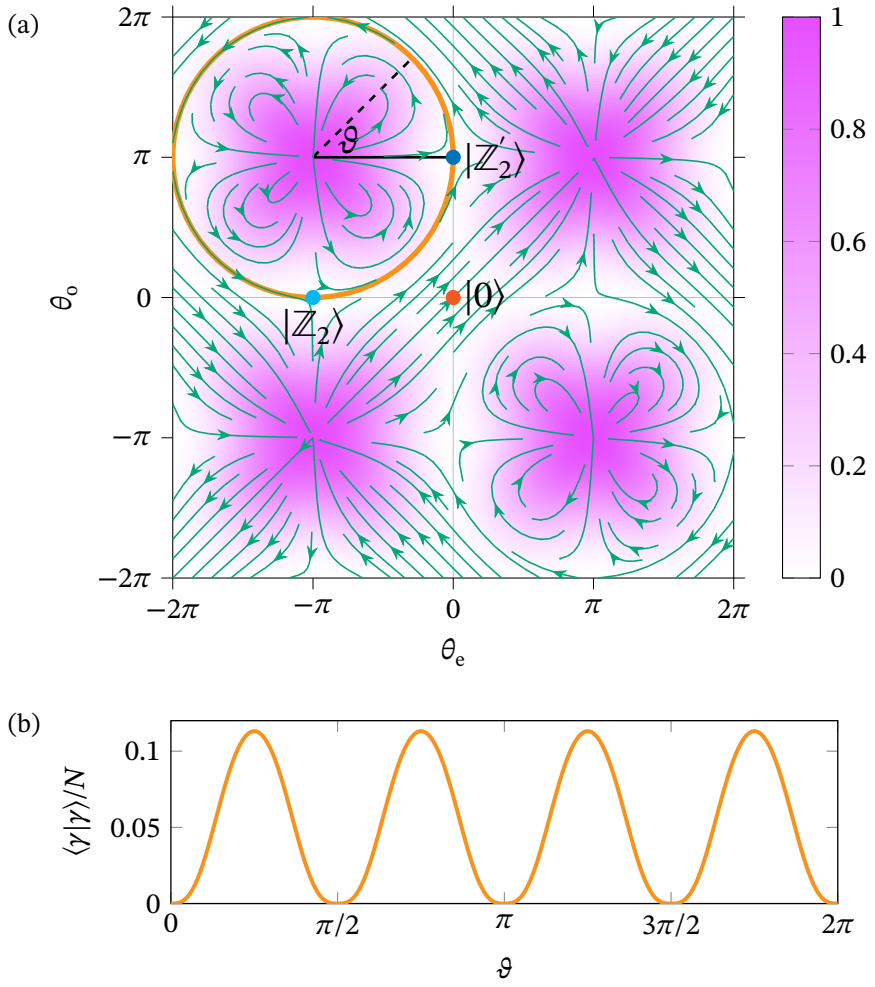

Figure 2.4: TDVP dynamics and leakage: (a) Stream plot of the TDVP dynamics. The background color map denotes the leakage. (b) Time evolution of the leakage along the periodic orbit.

	TDVP (classical)	Crossover	Eigenstate (quantum)
Non-integrable	Chaotic dynamics	Already discussed	Strong ETH
QMBS	Periodic orbit	**This study**	Scarred eigenstates

Table 2.2: Target of the present thesis.

Although the TDVP-based approach presented in this section is a powerful method to derive the corresponding classical system from a quantum many-body Hamiltonian, there is a qualitative difference from the quantum-classical correspondence in single-particle quantum mechanics. In single-particle systems, we can discuss the connection between the quantum and classical mechanics by considering the limit of $\hbar \to 0$. However, the dynamical system obtained in this section is defined on the artificial variational manifold, and it is difficult to see a smooth connection with the original quantum mechanics.

To overcome this problem, we have to stop fixing the expressive power of the variational manifold. The expressive power of the MPS is determined by a parameter called the bond dimension. When the bond dimension is small, the quantum correlation characterized by entanglement entropy is also small, and the state can be regarded as being in the classical regime. In this case, the dynamics obtained by TDVP becomes highly nonlinear. As the bond dimension is increased, the TDVP dynamics approaches the true Schrödinger equation, which is linear. In the limit of infinite bond dimension, it perfectly reproduces the results of quantum mechanics. Hence, by analyzing the bond-dimension dependence, we can discuss the crossover between the quantum and classical picture. For non-integrable quantum many-body systems, this crossover has been investigated by TDVP for MPS in the previous study [116], which is reviewed in Section 3.4. On the other hand, the variational state considered in this section is always in a subset of the MPS with bond dimension two, since the state is derived by applying the matrix product operator with bond dimension two onto the product state.

The fixed dimension of the variational manifold poses other problems as well. To see the exciting behavior of continuous dynamical systems, including chaos, we need to consider three or more spatial dimensions. In this sense, it is fair to say that the system that we have considered here is too simple. There are approaches to deal with higher-dimensional manifolds by changing the size of the unit cell [98]. However, it is still a problem that the simplest situation, relaxation from the $|\mathbb{Z}_2\rangle$ state, cannot be handled.

As depicted in Table 2.2, the aim of the present thesis is to discuss the periodic orbits in larger bond dimensions and fill the gap between the classical and quantum picture of the QMBS.

3 | Semiclassical Approximation of Quantum Many-Body Dynamics

In this chapter, we review the time-dependent variational principle (TDVP), which enables us to construct a semiclassical equation of motion systematically from a quantum Hamiltonian. Combining it with the matrix product state (MPS) representation, we can obtain semiclassical dynamics of a quantum many-body system in the thermodynamic limit. In Section 3.1, we introduce the general formulation of TDVP based on the projection operator onto the tangent space. In Section 3.2, we define MPS in the thermodynamic limit and its diagram representation. In Section 3.3, we describe the details of the TDVP algorithm for MPS. In Section 3.4, we review previous studies that analyzed thermalization and quantum many-body chaos by using TDVP for MPS.

3.1 Time-dependent variational principle

In this section, we introduce the time-dependent variational principle (TDVP) [105–109], a generic method to derive semiclassical nonlinear dynamics from a quantum Hamiltonian. We give a basic derivation based on the projection operator onto the tangent space in Section 3.1.1 and discuss the symmetries and conservation laws in Section 3.1.2.

3.1.1 TDVP derivation based on projection operator

Let us consider a set of quantum states $\{|\psi(\mathbf{x})\rangle\}$ parameterized by classical numbers $\mathbf{x} \in \mathbb{R}^N$. For simplicity, we assume that the states $|\psi(\mathbf{x})\rangle$ are normalized, i.e., $\langle\psi(\mathbf{x})|\psi(\mathbf{x})\rangle = 1$ holds. We regard this set as a manifold $\mathcal{M}$ embedded in the total Hilbert space $\mathcal{H}$. Our goal is to obtain $\dot{\mathbf{x}}$ as a function of $\mathbf{x}$, which defines the variational time evolution $(\mathrm{d}/\mathrm{d}t)|\psi(\mathbf{x})\rangle = \dot{x}^i|\partial_i\psi(\mathbf{x})\rangle$ as a good approximation of the true quantum dynamics described by the Schrödinger equation $\mathrm{i}(\mathrm{d}/\mathrm{d}t)|\psi\rangle = \hat{H}|\psi\rangle$. In Section 2.2.2, we considered the Lagrangian

$$\mathcal{L}(\mathbf{x}, \dot{\mathbf{x}}) = \mathrm{Re}\langle\psi(\mathbf{x})|\mathrm{i}\dot{x}^i|\partial_i\psi(\mathbf{x})\rangle - \langle\psi(\mathbf{x})|\hat{H}|\psi(\mathbf{x})\rangle \tag{3.1.1}$$

and used the Euler-Lagrange equation to obtain the equation of motion of $\mathbf{x}$. It is called the Dirac-Frenkel variational principle [109] since it can be regarded as a generalization of the Dirac principle [108], a variational principle of quantum real-time dynamics with the following Lagrangian

$$\mathcal{L} = \mathrm{Re}\langle\psi|\left(\mathrm{i}\frac{\mathrm{d}}{\mathrm{d}t} - \hat{H}\right)|\psi\rangle. \tag{3.1.2}$$

In this section, we introduce another derivation of TDVP based on a projector onto the tangent space. We define the tangent vectors of $\mathcal{M}$ at $|\psi(\mathbf{x})\rangle$ as $|v_i(\mathbf{x})\rangle \coloneqq |\partial_i\psi(\mathbf{x})\rangle$. The tangent space is a linear subspace spanned by the tangent vectors: $T_{\psi(\mathbf{x})}\mathcal{M} \coloneqq \mathrm{span}_{\mathbb{R}}\{|v_i(\mathbf{x})\rangle\}$. We define a projector onto $T_\psi\mathcal{M}$ as $\hat{P}_{T_\psi\mathcal{M}} \coloneqq 2|v_i\rangle G^{ij}\,\mathrm{Re}\langle v_j|$, where G^{ij} is the inverse of the metric

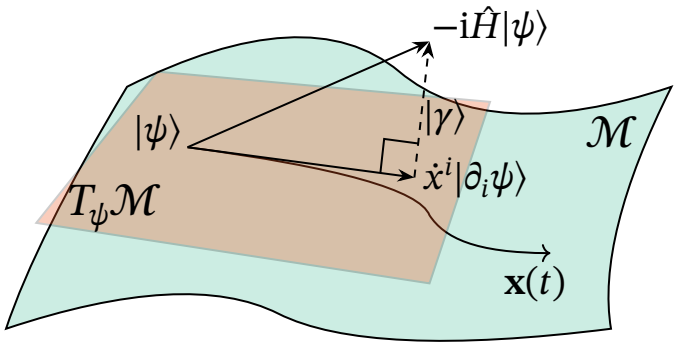

Figure 3.1: A schematic picture of TDVP. The variational manifold $\mathcal{M}$ is parameterized by the classical parameter $\mathbf{x}$ as $\mathcal{M} = \{|\psi(\mathbf{x})\rangle\}$. We project the original quantum dynamics $-\mathrm{i}\hat{H}|\psi\rangle$ onto the tangent space $T_\psi\mathcal{M}$ and obtain the dynamics $\dot{\mathbf{x}}$. $|\gamma\rangle$ denotes the difference between them.

$g_{ij} \coloneqq 2\,\mathrm{Re}\langle v_i|v_j\rangle$. By applying $\hat{P}_{T_\psi\mathcal{M}}$ onto the true quantum dynamics $-\mathrm{i}\hat{H}|\psi\rangle$, we obtain the variational time evolution

$$\dot{x}^i = -2G^{ij}\,\mathrm{Re}\langle v_j|\mathrm{i}\hat{H}|\psi\rangle = 2G^{ij}\,\mathrm{Im}\langle v_j|\hat{H}|\psi\rangle. \tag{3.1.3}$$

We depict a schematic picture of TDVP in Fig. 3.1. In this way, we obtain the time evolution that minimizes the norm of local error vector [138]

$$|\gamma\rangle \coloneqq \frac{\mathrm{d}}{\mathrm{d}t}|\psi\rangle + \mathrm{i}\hat{H}|\psi\rangle \tag{3.1.4}$$

by solving $\hat{P}_{T_\psi\mathcal{M}}|\gamma\rangle = 0$. In Section 2.2.2, we called the norm of $|\gamma\rangle$ the quantum leakage [98–100]. It is called the McLachlan minimal error principle [107]. In contrast, the Dirac-Frenkel variational principle is a result of $\hat{P}_{T_\psi\mathcal{M}}(\mathrm{i}\frac{\mathrm{d}}{\mathrm{d}t} - \hat{H})|\psi\rangle = \hat{P}_{T_\psi\mathcal{M}}\mathrm{i}|\gamma\rangle = 0$. Although the difference is only the complex factor i, these two principles can produce different results. In quantum mechanics, states are defined as rays in the Hilbert space. The ray is defined as an equivalence class of the Hilbert space corresponding to the equivalence relation $\sim$ where $|\psi\rangle \sim |\widetilde{\psi}\rangle :\Leftrightarrow \exists c \in \mathbb{C}\setminus\{0\}\,(|\psi\rangle = c|\widetilde{\psi}\rangle)$. However, the tangent space $T_\psi\mathcal{M}$ can ignore this structure since the variational manifolds are defined by a set of state vectors parameterized by classical real numbers. A variational manifold that reflects this structure is called a Kähler manifold. We can determine whether the variational manifold $\mathcal{M}$ is a Kähler manifold by considering the projection of the imaginary unit multiplication $J^i{}_j = \langle v_i|\hat{P}_{T_\psi\mathcal{M}}\mathrm{i}|v_j\rangle$. When $J^2 = -1_{D\times D}$ holds corresponding to $\mathrm{i}^2 = -1$, the variational manifold is a Kähler manifold. In this case, the Dirac-Frenkel and McLachlan principles give the same results [105]. We can check that the variational manifold considered in Section 2.2.2 is a Kähler manifold.

If the parameterization is given by a complex holomorphic function, the corresponding manifold becomes Kähler. In this case, we consider $\hat{P}_{T_\psi\mathcal{M}} = |v_i\rangle G^{ij}\langle v_j|$ instead where the tangent space is defined as $T_\psi\mathcal{M} \coloneqq \mathrm{span}_{\mathbb{C}}\{|\partial_i\psi(\mathbf{z})\rangle\}$ and G is defined as the inverse of the Gram matrix $g_{ij} = \langle v_i|v_j\rangle$. The matrix product state (MPS), which we discuss in the next section, is an example of this case [114].

3.1.2 Symmetries and conservation laws

In quantum dynamics, the expectation value of any symmetry generator, i.e., a Hermitian operator $\hat{A}$ that commutes with $\hat{H}$, does not change along the time evolution. This is a fundamental relationship between symmetry and conservation law. In the TDVP dynamics, the expectation values of some of the symmetry generators, including the Hamiltonian itself, conserve.

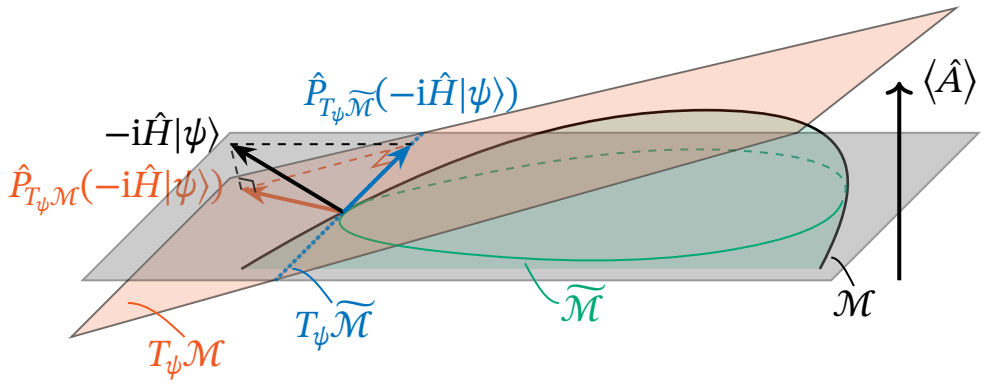

Figure 3.2: Enforcing conservation laws of TDVP.

However, the conservation is not guaranteed for all symmetry generators [105]. We illustrate it schematically in Fig. 3.2, where the horizontal plane denotes a contour of the expectation value $\langle\hat{A}\rangle$ and the original dynamics $-\mathrm{i}\hat{H}|\psi\rangle$ denoted by the black arrow has no component vertical to the contour. However, the projected vector $\hat{P}_{T_\psi\mathcal{M}}(-\mathrm{i}\hat{H}|\psi\rangle)$ denoted by the orange arrow has a finite component vertical to the contour. Roughly speaking, this is because the contour and the tangent space are not parallel. Conversely, if $\hat{A}|\psi\rangle$ does not have any vertical component to $T_\psi\mathcal{M}$, $\langle\hat{A}\rangle$ conserves in the TDVP dynamics.

We have two choices to obtain a TDVP dynamics conserving $\langle\hat{A}\rangle$. The first one is to enlarge the manifold to satisfy the conservation law. If $\hat{A}$ corresponds to important symmetry for physics, any manifolds on which TDVP dynamics does not conserve $\langle\hat{A}\rangle$ is an unnatural choice in the first place. Therefore, enlarging manifolds can be regarded as an extension to a more natural parameterization. However, there is no general guide to obtaining such an extended manifold, and sometimes it is impossible to find it.

The second choice is to enforce the conservation laws by hand. In this approach, we consider a submanifold of $\mathcal{M}$ defined as

$$\widetilde{\mathcal{M}} \coloneqq \{|\psi\rangle \in \mathcal{M} \,:\, \langle\psi|\hat{A}|\psi\rangle = \langle\psi_0|\hat{A}|\psi_0\rangle\} \tag{3.1.5}$$

instead of the original manifold $\mathcal{M}$. As depicted in Fig. 3.2, the difference between $\hat{P}_{T_\psi\mathcal{M}}(-\mathrm{i}\hat{H}|\psi\rangle)$ and $\hat{P}_{T_\psi\widetilde{\mathcal{M}}}(-\mathrm{i}\hat{H}|\psi\rangle)$ is parallel to the direction of the steepest decent of $\langle\hat{A}\rangle$. This direction is spanned by $\hat{P}_{T_\psi\mathcal{M}}(\hat{A}|\psi\rangle)$ and $\hat{P}_{T_\psi\mathcal{M}}(\mathrm{i}\hat{A}|\psi\rangle)$. Thus, we can obtain the TDVP dynamics corresponding to $\widetilde{\mathcal{M}}$ by shifting $\hat{P}_{T_\psi\mathcal{M}}(-\mathrm{i}\hat{H}|\psi\rangle)$ along $\hat{P}_{T_\psi\mathcal{M}}(\hat{A}|\psi\rangle)$ and $\hat{P}_{T_\psi\mathcal{M}}(\mathrm{i}\hat{A}|\psi\rangle)$. In this scheme, we can obtain TDVP with conservation systematically. However, this shift may break the conservation laws of other essential quantities such as energy.

3.2 Matrix product state in the thermodynamic limit

In this section, we introduce the matrix product state (MPS) representation for one-dimensional quantum many-body systems [101, 103, 139–144]. We also describe useful diagram representations. Each point of the lattice is labeled by integer $i \in [1, N] \cap \mathbb{Z}$, where N denotes the system size. The local Hilbert space $\mathcal{H}_i$ at site i is spanned by local basis $\{|s_i\rangle\}_{s_i=1}^{d_i}$. The total Hilbert space is defined as $\mathcal{H} = \bigotimes_{i=1}^{N} \mathcal{H}_i$. Any quantum state in $\mathcal{H}$ can be written as

$$\sum_{s_1=1}^{d_1} \cdots \sum_{s_N=1}^{d_N} c_{s_1,\ldots,s_N} \bigotimes_{j=1}^{N} |s_j\rangle, \tag{3.2.1}$$

where $c \in \mathbb{C}^{d_1 \times \cdots \times d_N}$ is a rank-N tensor with an exponentially large number of elements with the system size N. The fundamental idea of tensor networks (including MPS) is approximating this tensor c by the product of small rank tensors to reduce the number of parameters to a polynomial of order N.

An MPS with open boundary conditions (OBC) is defined as

$$
\begin{aligned}
|\psi(\mathbb{A})\rangle &= \sum_{\{s_j\}_{j=1}^N, \{i_j\}_{j=0}^N} (v_{\mathrm{L}})_{i_0} A[1]^{s_1}_{i_0,i_1} A[2]^{s_2}_{i_1,i_2} \cdots A[N]^{s_N}_{i_{N-1},i_N} (v_{\mathrm{R}})_{i_N} \bigotimes_{j=1}^N |s_j\rangle \\
&= \sum_{\{s_j\}_{j=1}^N} \quad \text{(diagram)} \quad \bigotimes_{j=1}^N |s_j\rangle \qquad (3.2.2) \\
&= \sum_{\{s\}} \mathbf{v}_{\mathrm{L}}^\dagger \left(\prod_{i=1}^N A[i]^{s_i} \right) \mathbf{v}_{\mathrm{R}} |\{s\}\rangle,
\end{aligned}
$$

where $A[j]$ is a complex-valued rank-three tensor with dimensions $D_{j-1} \times D_j \times d_j$, $\mathbf{v}_{\mathrm{L}}$ and $\mathbf{v}_{\mathrm{R}}$ are complex-valued vectors with dimensions D_0 and D_N, respectively, $\mathbb{A}$ denotes the set of $A[i]$ and $\mathbf{v}$. These D are called the bond dimensions, which control the expressive power of MPS. In the second line in Eq. (3.2.2), we introduce a diagram representation of MPS, where rank-k tensors are represented by nodes with k legs, each corresponding to a tensor index. Connected legs in the diagram mean taking the summation of the corresponding indices. Sometime, we omit to write $\sum_{\{s\}}$ and $\bigotimes_j |s_j\rangle$ explicitly in the diagram representation. The third line in Eq. (3.2.2) denotes an abbreviated expression. We can similarly define an MPS with periodic boundary conditions (PBC) by using this abbreviation as

$$
|\psi(\mathbb{A})\rangle = \sum_{\{s\}} \mathrm{Tr} \left[\prod_{i=1}^N A[i]^{s_i} \right] |\{s\}\rangle. \qquad (3.2.3)
$$

The transfer operator plays a central role in calculating physical quantities from MPS. We define the transfer operator $\mathcal{T}$ from a pair of tensors as

$$
\mathcal{T}_B^A := \sum_s A^s \otimes \bar{B}^s = \quad \text{(diagram)}, \qquad (3.2.4)
$$

where $\bar{B}$ denotes the complex conjugate of B. We similarly define the transfer operator for a pair of matrices $X, Y \in \mathbb{C}^{D \times D'}$ as $\mathcal{T}_Y^X = X \otimes \bar{Y}$. The only difference is the absence of the summation $\sum_s$. We introduce the notation of matrices as

$$
[|x)]_{i,j} = \quad \text{(diagram)}, \quad [(y|]_{i,j} = \quad \text{(diagram)}, \qquad (3.2.5)
$$

on which the transfer operator $\mathcal{T}_B^A$ acts as

$$
[\mathcal{T}_B^A |x)]_{i,j} = \sum_{s,k,l} A^s_{i,k} x_{k,l} \bar{B}^s_{j,l} = \quad \text{(diagram)}, \qquad (3.2.6)
$$

$$
[(y|\mathcal{T}_B^A]_{i,j} = \sum_{s,k,l} \bar{B}^s_{k,i} y_{k,l} A^s_{l,j} = \quad \text{(diagram)}. \qquad (3.2.7)
$$

We note that $(y|x) = \mathrm{Tr}[yx]$ holds. The notation $|x)$ and $(y|$ can be regarded as the notation of the vectorization of matrices. Under this interpretation, the transfer operator is regarded as the transfer matrix.

Physical quantities can be represented in terms of the transfer matrices. For example, the inner product of two MPSs can be written as

$$\langle\psi(\widetilde{\mathbb{A}})|\psi(\mathbb{A})\rangle = \begin{cases} \left(\tilde{\mathbf{v}}_{\mathrm{L}}\mathbf{v}_{\mathrm{L}}^{\dagger}\middle|\prod_i \mathcal{T}_{\widetilde{A}[i]}^{A[i]}\middle|\mathbf{v}_{\mathrm{R}}\tilde{\mathbf{v}}_{\mathrm{R}}^{\dagger}\right) & (\mathrm{OBC}) \\ \mathrm{Tr}\left[\prod_i \mathcal{T}_{\widetilde{A}[i]}^{A[i]}\right] & (\mathrm{PBC}) \end{cases}. \tag{3.2.8}$$

Any expectation value of the product of onsite operators $\langle\psi(\mathbb{A})|\hat{o}_{j_1}\ldots\hat{o}_{j_k}|\psi(\mathbb{A})\rangle$ can be obtained by replacing $\mathcal{T}_{A[j]}^{A[j]}$ in Eq. (3.2.8) by operator transfer matrices defined by

$$\sum_{s,t}\langle t|\hat{o}_j|s\rangle A[j]^s \otimes \bar{A}[j]^t. \tag{3.2.9}$$

Next, we define the uniform MPS [110, 112, 114, 145] by letting all $A[i]$ equal and taking the $N\to\infty$ limit as

$$|\psi(A)\rangle = \sum_{\{s\}}\mathbf{v}_{\mathrm{L}}^{\dagger}\left(\prod_{i\in\mathbb{Z}}A^{s_i}\right)\mathbf{v}_{\mathrm{R}}|\{s\}\rangle, \tag{3.2.10}$$

where $A\in\mathbb{C}^{D\times D\times d}$ and $\mathbf{v}\in\mathbb{C}^D$. The uniform MPS is a good variational state for translation invariant state in the thermodynamic limit. Since the choice of boundary conditions and boundary vectors $\mathbf{v}$ does not change the physics in this limit, we take OBC here. The correspondence between A and $|\psi(A)\rangle$ is not one-to-one. For any $c\in\mathbb{C}\setminus\{0\}$ and $X\in\mathbb{C}^{D\times D}$ s.t. $\det X\neq 0$, A^s and cXA^sX^{-1} represent the same quantum state. We choose $c=1/\sqrt{\lambda_{\mathrm{LM}}(\mathcal{T}_A^A)}$ for MPS to satisfy the normalization condition $\langle\psi(A)|\psi(A)\rangle=1$, where λ_{LM} denotes the eigenvalue of the transfer matrix with the largest magnitude. Here, we assume that λ_{LM} is not degenerate. This condition is called injectivity, which means that the state does not have a long-range order. Hereafter, we always consider normalized and injective MPSs if not mentioned otherwise. The transformation $A^s\to XA^sX^{-1}$ is called a gauge transformation. We introduce gauge fixing conditions called canonical conditions, to remove these gauge degrees of freedom. The left canonical condition is characterized by the equation

$$(1_{D\times D}|\mathcal{T}_A^A = (1_{D\times D}|, \tag{3.2.11}$$

where $1_{D\times D}$ denotes a $D\times D$ unit matrix. We can transform A to satisfy the left canonical condition as $A_{\mathrm{L}}^s=\sqrt{l}A^s\sqrt{l}^{-1}$, where l denotes a matrix with its vectorization being the dominant left eigenvector $(l|\mathcal{T}_A^A=(l|$ and $\sqrt{l}$ satisfies $\sqrt{l}^{\dagger}\sqrt{l}=l$. We introduce a special shape for a node representing a left canonical tensor A_{L}:  . Similarly, we define the right canonical condition and special shape for the right canonical tensor $A_{\mathrm{R}}^s=\sqrt{r}^{-1}A^s\sqrt{r}$:  , where $\mathcal{T}_A^A|r)=|r)$. We also introduce center-site tensor $A_{\mathrm{C}}^s=\sqrt{l}A^s\sqrt{r}$:  and center bond matrix $C=\sqrt{l}\sqrt{r}$:  . With these, we define the left canonical MPS and two kinds of mixed canonical MPS as

$$\begin{aligned} |\psi(A)\rangle &= \sum_{\{s\}}\mathbf{v}_{\mathrm{L}}^{\dagger}\left(\prod_i A_{\mathrm{L}}^{s_i}\right)\mathbf{v}_{\mathrm{R}}|\{s\}\rangle && = \text{- -}\!\!\rightarrow\!\!\rightarrow\!\!\rightarrow\!\!\rightarrow\!\!\rightarrow\!\!\rightarrow\!\!\rightarrow\text{- -} \\ &= \sum_{\{s\}}\mathbf{v}_{\mathrm{L}}^{\dagger}\left(\prod_{i<j} A_{\mathrm{L}}^{s_i}\right)A_{\mathrm{C}}^{s_j}\left(\prod_{j<i} A_{\mathrm{R}}^{s_i}\right)\mathbf{v}_{\mathrm{R}}|\{s\}\rangle && = \text{- -}\!\!\rightarrow\!\!\rightarrow\!\!\rightarrow\!\!\diamond\!\!\leftarrow\!\!\leftarrow\!\!\leftarrow\text{- -} \\ &= \sum_{\{s\}}\mathbf{v}_{\mathrm{L}}^{\dagger}\left(\prod_{i\le j} A_{\mathrm{L}}^{s_i}\right)C\left(\prod_{j<i} A_{\mathrm{R}}^{s_i}\right)\mathbf{v}_{\mathrm{R}}|\{s\}\rangle && = \text{- -}\!\!\rightarrow\!\!\rightarrow\!\!\rightarrow\!\!\rightarrow\!\!\leftarrow\!\!\leftarrow\!\!\leftarrow\text{- -}. \end{aligned} \tag{3.2.12}$$

Note that the position j does not change the state.

For a mixed canonical uniform MPS, any expectation value of on-site operator $\hat{o}$ can be written in a compact local form as

$$\langle\psi(A)|\hat{o}_i|\psi(A)\rangle = (1_{D\times D}|\left[\sum_{s_i,t_i}\langle t_i|\hat{o}_i|s_i\rangle A_{\mathrm{C}}^{s_i}\otimes\bar{A}_{\mathrm{C}}^{t_i}\right]|1_{D\times D}). \tag{3.2.13}$$

We can similarly obtain the expectation values of nearest-neighbor operators and so on. The bipartite entanglement entropy of $|\psi(A)\rangle$ is defined as

$$\mathcal{S} = -\sum_{i=1}^{D}\sigma_i^2\ln\sigma_i^2 \leq \ln D, \tag{3.2.14}$$

where σ_i denotes the coefficients of the Schmidt decomposition, which are equal to the singular values of C.

3.3 TDVP for uniform MPS

In this section, we discuss the TDVP algorithm for the uniform MPS [110–115]. In Section 3.3.1, we consider the time derivative of the uniform MPS. In Section 3.3.2, we introduce numerical integration techniques to obtain accurate time evolution. In Sections 3.3.3 and 3.3.4, we discuss the symmetry and leakage of TDVP for MPS.

3.3.1 Time derivative

To consider the tangent vector, we take the left canonical form and take the derivative with respect to A_{L} as

$$|\phi(A;B)\rangle \coloneqq \sum_k B_k\frac{\partial|\psi(A)\rangle}{\partial(A_{\mathrm{L}})_k} = \sum_j\sum_{\{s\}}\mathbf{v}_{\mathrm{L}}\left(\prod_{i<j}A_{\mathrm{L}}^{s_i}\right)B^{s_j}\left(\prod_{j<i}A_{\mathrm{L}}^{s_i}\right)\mathbf{v}_{\mathrm{R}}|\{s\}\rangle, \tag{3.3.1}$$

where k denotes the three tensor indices of A_{L}. It can be regarded as the parameterization of the tangent vector by the tensor $B\in\mathbb{C}^{D\times D\times d}$. We can obtain the time derivative of A_{L} by solving

$$|\phi(A;\dot{A}_{\mathrm{L}})\rangle = \hat{P}_{T_\psi\mathcal{M}}(-\mathrm{i}\hat{H}|\psi(A)\rangle) \tag{3.3.2}$$

where $\hat{P}_{T_\psi\mathcal{M}}$ denotes the projection operator onto the tangent space.

Let us discuss the details of the projector $\hat{P}_{T_\psi\mathcal{M}}$. The derivative shown in Eq. (3.3.1) suggests that the dimension of the tangent space is that of the tensor B. However, since the gauge transformation $B^s\to B^s+A_{\mathrm{L}}^sX-XA_{\mathrm{L}}^s$ for $\forall X\in\mathbb{C}^{D\times D}$ does not change the tangent vector $|\phi\rangle$, the true degrees of freedom is $D\times D\times d-D\times D=D\times D\times(d-1)$. To avoid the over-parameterization, we impose a gauge fixing condition $(1_{D\times D}|\mathcal{T}_B^{A_{\mathrm{L}}}=0$. Under this condition, we can derive a good parameterization of B. We consider an orthogonal basis of the null space of $(\mathcal{A}_{\mathrm{L}})_{(l,s),r}=(A_{\mathrm{L}})_{l,r}^s=$ denoted as $\mathcal{V}_{\mathrm{L}}\in\mathbb{C}^{Dd\times D(d-1)}$. Here, $\mathcal{A}_{\mathrm{L}}^\dagger\mathcal{V}_{\mathrm{L}}=0$ and $\mathcal{V}_{\mathrm{L}}^\dagger\mathcal{V}_{\mathrm{L}}=1_{D(d-1)\times D(d-1)}$ hold. We define $V_{\mathrm{L}}\in\mathbb{C}^{D\times D(d-1)\times d}$ by reshaping $\mathcal{V}_{\mathrm{L}}$ and let it be denoted by a diagram  . We note that the index going out from the right has $D(d-1)$ degrees of freedom, not D. The tensor V_{L} satisfies the following properties:

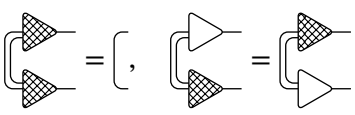 (3.3.3)

We consider parameterization of the tangent space based on V_{L} as $B^s(X) = V_{\mathrm{L}}^s X C^{-1}$, where $X \in \mathbb{C}^{D(d-1)\times D}$. Now we can rewrite Eq. (3.3.1) as

$$\begin{aligned}|\phi(A;B(X))\rangle &= \sum_j \sum_{\{s\}} \mathbf{v}_{\mathrm{L}} \left(\prod_{i<j} A_{\mathrm{L}}^{s_i}\right) V_{\mathrm{L}}^{s_j} X C^{-1} \left(\prod_{j<i} A_{\mathrm{L}}^{s_i}\right) \mathbf{v}_{\mathrm{R}} |\{s\}\rangle \\ &= \sum_j \sum_{\{s\}} \mathbf{v}_{\mathrm{L}} \left(\prod_{i<j} A_{\mathrm{L}}^{s_i}\right) V_{\mathrm{L}}^{s_j} X \left(\prod_{j<i} A_{\mathrm{R}}^{s_i}\right) \mathbf{v}_{\mathrm{R}} |\{s\}\rangle.\end{aligned} \tag{3.3.4}$$

Now let us consider the Gram matrix $g_{YX} \coloneqq \langle \phi(A;B(Y))|\phi(A;B(X))\rangle$. Since $(1_{D\times D}|\mathcal{T}_{V_{\mathrm{L}}}^{A_{\mathrm{L}}} = 0$ and $(1_{D\times D}|\mathcal{T}_{A_{\mathrm{L}}}^{V_{\mathrm{L}}} = 0$, it can be written as

$$\begin{aligned}g_{YX} &= |\mathbb{Z}|(1_{D\times D}|\mathcal{T}_{V_{\mathrm{L}}Y}^{V_{\mathrm{L}}X}|1_{D\times D}) \\ &= |\mathbb{Z}|(1_{D(d-1)\times D(d-1)}|\mathcal{T}_Y^X|1_{D\times D}) \\ &= |\mathbb{Z}|\,\mathrm{Tr}[Y^\dagger X],\end{aligned} \tag{3.3.5}$$

where $|\mathbb{Z}|$ is the notation of the divergent term in the thermodynamic limit corresponding to the system size. The last form is proportional to the Euclidean inner product of the vectorized matrices X and Y. Thus, by using this parameterization, we can ignore calculating the inverse of g, and the projector onto the tangent space can be written as

$\hat{P}_{T_\psi\mathcal{M}} = \sum_i$ 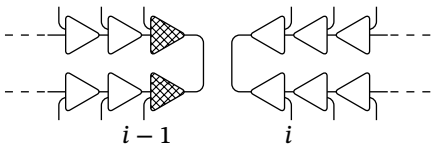

$= \sum_i$ 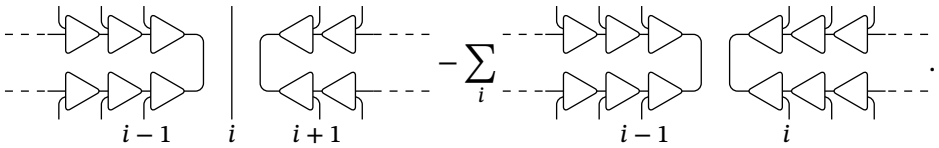

(3.3.6)

To obtain the expression in the last line, we use the relation between A_{L} and V_{L} depicted by the following diagram:

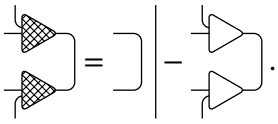

(3.3.7)

Now, we consider the vector $\hat{P}_{T_\psi\mathcal{M}}(-\mathrm{i}\hat{H})|\psi(A)\rangle$. Let us define H_{eff} acting on A_{C} and C to satisfy the following diagrams:

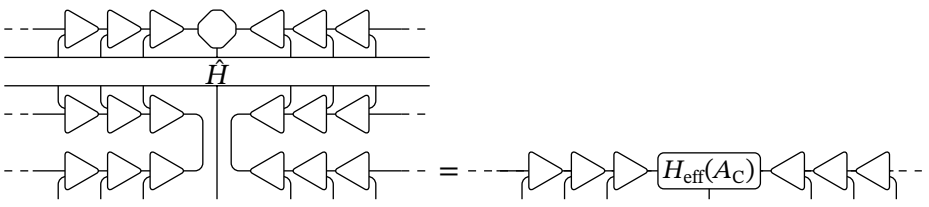

(3.3.8)

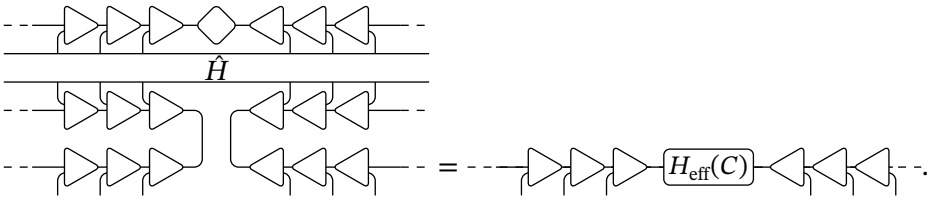

(3.3.9)

Then, we obtain

$$\begin{aligned}\hat{P}_{T_\psi\mathcal{M}}(-\mathrm{i}\hat{H})|\psi(A)\rangle &= -\mathrm{i}\sum_j\sum_{\{s\}}\mathbf{v}_\mathrm{L}\left(\prod_{i<j}A_\mathrm{L}^{s_i}\right)H_\mathrm{eff}(A_\mathrm{C})^{s_j}\left(\prod_{j<i}A_\mathrm{R}^{s_i}\right)\mathbf{v}_\mathrm{R}|\{s\}\rangle \\ &\quad+\mathrm{i}\sum_j\sum_{\{s\}}\mathbf{v}_\mathrm{L}\left(\prod_{i\le j}A_\mathrm{L}^{s_i}\right)H_\mathrm{eff}(C)\left(\prod_{j<i}A_\mathrm{R}^{s_i}\right)\mathbf{v}_\mathrm{R}|\{s\}\rangle \\ &= -\mathrm{i}\sum_j\sum_{\{s\}}\mathbf{v}_\mathrm{L}\left(\prod_{i<j}A_\mathrm{L}^{s_i}\right)(H_\mathrm{eff}(A_\mathrm{C})^{s_j}-A_\mathrm{L}^{s_j}H_\mathrm{eff}(C))C^{-1}\left(\prod_{j<i}A_\mathrm{L}^{s_i}\right)\mathbf{v}_\mathrm{R}|\{s\}\rangle.\end{aligned} \tag{3.3.10}$$

We thereby arrive at the time derivative of A_L as

$$\dot{A}_\mathrm{L} = -\mathrm{i}(H_\mathrm{eff}(A_\mathrm{C})^{s_j}-A_\mathrm{L}^{s_j}H_\mathrm{eff}(C))C^{-1}. \tag{3.3.11}$$

Let us consider the detail of H_eff. In general, if $\hat{H}$ can be represented in the form of a matrix product operator, we can obtain a simple form of H_eff. Hereafter, for simplicity, we assume that the Hamiltonian is the sum of nearest-neighbor interactions as $\hat{H}=\sum_i\hat{h}_{i,i+1}$. We shift the origin of the energy to zero as $\hat{h}\to\hat{h}-\langle\hat{h}\rangle$. Let us define the infinite boundary conditions L and R. We introduce L_h and R_h defined as

$(L_h|=$ 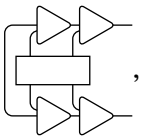 , $|R_h)=$ 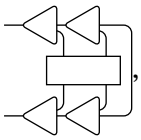 , (3.3.12)

where the rectangles denote $\hat{h}-\langle\hat{h}\rangle$. The infinite boundary conditions [146] are defined as

$$(L|\coloneqq(L_h|\sum_{n=0}^{\infty}(\mathcal{T}_{A_\mathrm{L}}^{A_\mathrm{L}})^n,\quad |R)\coloneqq\sum_{n=0}^{\infty}(\mathcal{T}_{A_\mathrm{R}}^{A_\mathrm{R}})^n|R_h). \tag{3.3.13}$$

We can obtain them without calculating the infinite summation because L and R satisfy the following linear equations:

$$(L|(1-\mathcal{T}_{A_\mathrm{L}}^{A_\mathrm{L}}+|CC^\dagger)(1_{D\times D}|)=(L_h|,\quad(1-\mathcal{T}_{A_\mathrm{R}}^{A_\mathrm{R}}+|1_{D\times D})(C^\dagger C|)|R)=|R_h). \tag{3.3.14}$$

To derive the equation of $(L|$, let us consider eigendecomposition of $\mathcal{T}_{A_\mathrm{L}}^{A_\mathrm{L}}$:

$$\mathcal{T}_{A_\mathrm{L}}^{A_\mathrm{L}}=\sum_{i=1}^{D^2}\lambda_i|r_i)(l_i|=|CC^\dagger)(1_{D\times D}|+\sum_{i=2}^{D^2}\lambda_i|r_i)(l_i|, \tag{3.3.15}$$

where l_i, r_i, and λ_i satisfy

$$\begin{gathered}(l_i|\mathcal{T}_{A_\mathrm{L}}^{A_\mathrm{L}}=\lambda_i(l_i|,\quad\mathcal{T}_{A_\mathrm{L}}^{A_\mathrm{L}}|r_i)=\lambda_i|r_i),\quad(l_i|r_k)=\delta_{i,k},\quad\lambda_1>\lambda_2\ge\lambda_3\ge\dots, \\ l_1=1_{D\times D},\quad r_1=CC^\dagger,\quad\lambda_1=1.\end{gathered} \tag{3.3.16}$$

Since $(L_h|r_1)=\langle\hat{h}-\langle\hat{h}\rangle\rangle=0$ holds, we can consider

$$\sum_{n=0}^{\infty}(\mathcal{T}_{A_\mathrm{L}}^{A_\mathrm{L}}-|CC^\dagger)(1_{D\times D}|)^n=\sum_{i=2}^{D^2}\sum_n\lambda_i^n|r_i)(l_i|=\sum_{i=2}^{D^2}\frac{1}{1-\lambda_i}|r_i)(l_i|=:(1-\mathcal{T}_{A_\mathrm{L}}^{A_\mathrm{L}})^P \tag{3.3.17}$$

instead of the infinite summation in Eq. (3.3.13), where P denotes the pseudo-inverse (the Moore-Penrose inverse). We can calculate the multiplication of the pseudo-inverse matrix on $(L_h|$ by solving the linear equation defined in Eq. (3.3.14) since the equations

$$\begin{aligned}\frac{1}{|CC^\dagger)(1_{D\times D}| + 1 - \mathcal{T}_{A_\mathrm{L}}^{A_\mathrm{L}}} &= \frac{1}{|CC^\dagger)(1_{D\times D}| + \sum_{i=2}^{D^2}(1-\lambda_i)|r_i)(l_i|} \\ &= |CC^\dagger)(1_{D\times D}| + \sum_{i=2}^{D^2}\frac{1}{1-\lambda_i}|r_i)(l_i| \\ &= |CC^\dagger)(1_{D\times D}| + (1-\mathcal{T}_{A_\mathrm{L}}^{A_\mathrm{L}})^P\end{aligned} \tag{3.3.18}$$

and $(L_h|CC^\dagger) = 0$ hold. We can derive the linear equation of $|R)$ in a similar way.

By combining the infinite boundary conditions and the diagrams in Eqs. (3.3.8) and (3.3.9), we obtain the local form of H_eff as follows:

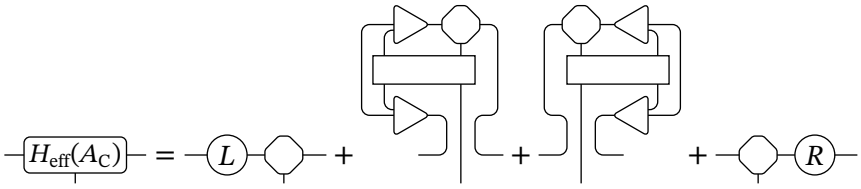

(3.3.19)

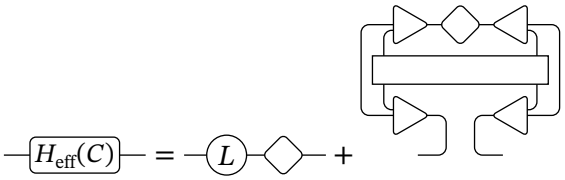

(3.3.20)

3.3.2 Numerical integration

The simplest way to calculate the real-time dynamics of a uniform MPS is the Euler method: calculating $\dot{A}_\mathrm{L}$ by Eq. (3.3.11) at each time step and updating the state as $A_\mathrm{L} \to A_\mathrm{L} + \delta t \dot{A}_\mathrm{L}$, where δt denotes a small time step. However, this update conserves the canonical condition only in the first order of δt. Thus, we have to re-canonicalize the state at each time step. As we discussed at the end of Section 3.2, we can obtain the canonical form of MPS by solving a dominant eigenvalue problem of the transfer matrix.

In this algorithm, we have to consider the inverse of matrices C^{-1}, $\sqrt{l}^{-1}$, and $\sqrt{r}^{-1}$ to calculate $\dot{A}_\mathrm{L}$ by using Eq. (3.3.11) and to canonicalize the state. However, matrix inverse calculation can cause large numerical errors. Here, we construct an inverse-free algorithm to obtain precise results. In the inverse-free algorithm, instead of calculating $\dot{A}_\mathrm{L}$ explicitly, we consider $\dot{A}_\mathrm{C} \coloneqq -\mathrm{i}H_\mathrm{eff}(A_\mathrm{C})$ and $\dot{C} \coloneqq -\mathrm{i}H_\mathrm{eff}(C)$. First, we update A_C and C as $A_\mathrm{C} \to A'_\mathrm{C} = A_\mathrm{C} + \delta t \dot{A}_\mathrm{C}$ and $C \to C' = C + \delta t \dot{C}$. Then, we obtain the updated $A'_\mathrm{L} \in S_\mathrm{L}$ by solving minimization problem of $\|A'_\mathrm{C} - A'_\mathrm{L}C\|$, where $S_\mathrm{L} = \{A \in \mathbb{C}^{D\times D\times d} : (1_{D\times D}|\mathcal{T}_A^A = (1_{D\times D}|\}$. We can solve this optimization problem by using the Singular Value Decomposition (SVD) or the QR decomposition. The SVD-based algorithm gives an exact result in principle. We define $(\mathcal{A}'_\mathrm{C})_{(l,s),r} \coloneqq (A'_\mathrm{C})^s_{l,r}$ and consider its SVD $\mathcal{A}'_\mathrm{C}(C')^\dagger = U\Sigma V^\dagger$. Then, $(\mathcal{A}'_\mathrm{L})_{(l,s),r} \coloneqq (A'_\mathrm{L})^s_{l,r}$ is obtained as $\mathcal{A}'_\mathrm{L} = UV^\dagger$. However, Σ can contain very small values near the machine precision since Σ is approximately equal to the square of singular values of an almost normalized matrix C'. It makes the numerical calculation unstable. On the other hand, the algorithm based on the QR decomposition gives a better result without this problem. The QR-based algorithm gives the exact result in the $\delta t \to 0$ limit. Here, we consider the QR decompositions $\mathcal{A}'_\mathrm{C} = Q_{\mathcal{A}'_\mathrm{C}} R_{\mathcal{A}'_\mathrm{C}}$ and $(C')^\dagger = Q_{(C')^\dagger} R_{(C')^\dagger}$,

where $Q_{\mathcal{A}'_{\mathrm{C}}}$ and $Q_{(C')^\dagger}$ are unitary matrices and $R_{\mathcal{A}'_{\mathrm{C}}}$ and $R_{(C')^\dagger}$ are upper triangle matrices. We take the signs of the diagonal elements of $R_{\mathcal{A}'_{\mathrm{C}}}$ and $R_{(C')^\dagger}$ positive to make the decomposition unique. The approximated $\mathcal{A}'_{\mathrm{L}}$ is obtained as $Q_{\mathcal{A}'_{\mathrm{C}}} Q_{(C')^\dagger}$.

The QR decomposition is also helpful to obtain the canonical form of the uniform MPS without using matrix inversion. First, we prepare some initial matrix $X^{(0)}$ and consider QR decomposition $\widetilde{\mathcal{A}}^{(0)}_{(l,s),r} = X^{(0)}_{l,i} A^s_{i,r}$ as $\widetilde{\mathcal{A}}^{(0)} = \mathcal{A}^{(0)}_{\mathrm{L}} X^{(1)}$. By repeating this process after replacing $X^{(i-1)}$ by $X^{(i)}$ until $X^{(i)} \approx X^{(i+1)}$ holds, we obtain a pair of X and A_{L} satisfying $XA = A_{\mathrm{L}} X \Leftrightarrow XAX^{-1} = A_{\mathrm{L}}$, where A_{L} satisfies the left canonical condition. This iteration converges because we consider the unique QR decomposition by fixing the signs of diagonal elements. We can also obtain the dominant eigenvector as $X^\dagger X$. We can obtain A_{R} similarly by considering the LQ decomposition instead.

In many cases, the solutions obtained by the Euler method are not accurate enough. Although we can improve the accuracy by using the higher-order Runge-Kutta method, unphysical solutions that violate important properties such as the energy-conservation law can be obtained. We can improve the results by using a symplectic integrator for Hamiltonian systems. However, it is difficult to apply it to TDVP for MPS because there is no simple separation between the kinetic term and the potential term in the Lagrangian. Instead, we use a symmetric integrator to obtain accurate energy-conserving results. In the simple Euler method, time-reversal symmetry breaks in the second order of δt, i.e., $A_{\mathrm{L}}(t)$ and $A'_{\mathrm{L}}(t)$ are not equivalent to each other if $A'_{\mathrm{L}}(t)$ is obtained by the following time step: $A_{\mathrm{L}}(t) \xrightarrow[\text{Euler}]{+\delta t} A_{\mathrm{L}}(t+\delta t) \xrightarrow[\text{Euler}]{-\delta t} A'_{\mathrm{L}}(t)$. In symmetric integration, we obtain the midpoint $\widetilde{A_{\mathrm{L}}}(t+\delta t/2)$ satisfying $\widetilde{A_{\mathrm{L}}}(t+\delta t/2) \xrightarrow[\text{Euler}]{-\delta t/2} A_{\mathrm{L}}(t)$ and calculate $\widetilde{A_{\mathrm{L}}}(t+\delta t/2) \xrightarrow[\text{Euler}]{+\delta t/2} A_{\mathrm{L}}(t+\delta t)$. In this scheme, we obtain results satisfying the time reversal symmetry. To obtain the midpoint, we use an iterative algorithm. As a starting point, we calculate the time evolution over $+\delta t/2$ by the Euler method denoted as $A_{\mathrm{L}} \to \widetilde{A_{\mathrm{L}}}^{(0)}$. Next, we calculate the backward time evolution over $-\delta t/2$ from it and define it as $A^{(0)}_{\mathrm{L}}$. Then, we calculate $\Delta A^{(0)}_{\mathrm{L}} = A_{\mathrm{L}} - A^{(0)}_{\mathrm{L}}$ and its norm. If the norm is under the threshold, we adopt $\widetilde{A_{\mathrm{L}}}^{(0)}$ as $\widetilde{A_{\mathrm{L}}}$. If not, we update $\widetilde{A_{\mathrm{L}}}^{(1)} = \widetilde{A_{\mathrm{L}}}^{(0)} + \Delta A^{(0)}_{\mathrm{L}}$ and calculate $A^{(1)}_{\mathrm{L}}$ again. Repeating this process until convergence, we finally obtain $\widetilde{A_{\mathrm{L}}}$.

3.3.3 Symmetry

In TDVP for MPS, it is guaranteed to conserve the expectation values of any local symmetry generators, i.e., Hermitian operators satisfying $[\hat{H}, \hat{A}] = 0$ and $\hat{A} = \sum_i \hat{a}_i$, where $\hat{a}_i$ acts on $\mathcal{H}_i$ [112]. This is a great advantage of the TDVP algorithm over the other MPS-based algorithms, such as the time-dependent density matrix renormalization group [147] and the time-evolving block decimation [148]. In many cases, physically important symmetries are written in this local form.

On the other hand, the conservation of non-local symmetry is not guaranteed. Thus, we have to consider the conservation enforcing technique discussed in Section 3.1.2 for systems with important non-local symmetry. For example, in the studies of QMBS, the importance of non-local deformed symmetry denoted by a matrix product operator, such as $\hat{\mathcal{P}}_{\mathrm{RB}}$ defined in Eq. (2.2.3), has been pointed out [65].

3.3.4 Leakage

The quantum leakage of TDVP is defined as the norm of the error vector defined in Eq. (3.1.4). In TDVP for the MPS with the nearest-neighbor interacting Hamiltonian, we can obtain a

simple local form for the error vector [149]. Similarly to V_{L}, we consider $V_{\mathrm{R}} \in \mathbb{C}^{D(d-1)\times D\times d}$ satisfying $\mathcal{T}^{V_{\mathrm{R}}}_{V_{\mathrm{R}}}|1_{D\times D}) = |1_{D(d-1)\times D(d-1)})$ and $\mathcal{T}^{A_{\mathrm{R}}}_{V_{\mathrm{R}}}|1_{D\times D}) = \mathcal{T}^{V_{\mathrm{R}}}_{A_{\mathrm{R}}}|1_{D\times D}) = 0$. By using V_{L} and V_{R}, the identity operator of the Hilbert space can be written as

$\hat{1} = |\psi\rangle\langle\psi| + \hat{P}_{T_\psi\mathcal{M}} + \sum_i$ 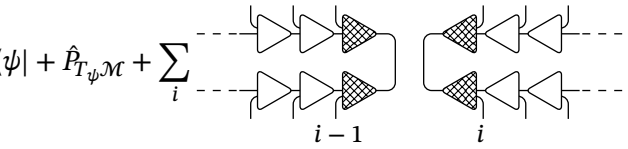

$+\sum_i$ 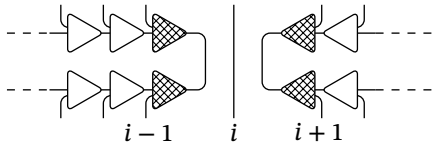 $+\sum_i$ 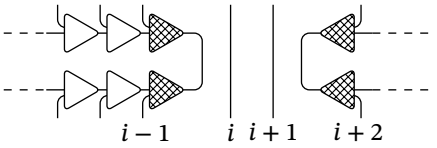 $+ \ldots .$ (3.3.21)

The infinite sum in the second line vanishes in calculating $(1-\hat{P}_{T_\psi\mathcal{M}})\hat{h}_i|\psi\rangle$ for $\forall i$ since $(1_{D\times D}|\mathcal{T}^{A_{\mathrm{L}}}_{V_{\mathrm{L}}} = 0$ and $\mathcal{T}^{A_{\mathrm{R}}}_{V_{\mathrm{R}}}|1_{D\times D}) = 0$. Thus, the error vector can be written as

$|\gamma\rangle = (1 - \hat{P}_{T_\psi\mathcal{M}})(-\mathrm{i}\hat{H})|\psi\rangle = -\mathrm{i}\sum_i$ 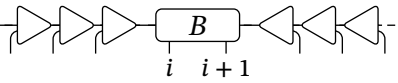 , (3.3.22)

where B is depicted by the diagram

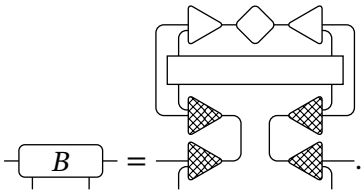 . (3.3.23)

Since $(1_{D\times D}|\mathcal{T}^{B}_{A_{\mathrm{L}}A'} = 0$ and $\mathcal{T}^{B}_{A'A_{\mathrm{R}}}|1_{D\times D}) = 0$ hold for any $A' \in \mathbb{C}^{D\times D\times d}$, the inner product of $|\gamma\rangle$ can be written as

$$\langle\gamma|\gamma\rangle = |\mathbb{Z}|(1_{D\times D}|\mathcal{T}^{B}_{B}|1_{D\times D}). \tag{3.3.24}$$

In the case of conservation enforcing TDVP discussed in Section 3.1.2, $\dot{A}_{\mathrm{L}}$ is shifted by a tensor $\dot{A}'_{\mathrm{L}}$. For this case, we can obtain the error vector by considering a shift $-\mathrm{i}B \to -\mathrm{i}B + A_{\mathrm{L}}\dot{A}'_{\mathrm{L}}$.

3.4 Chaos and thermalization in semiclassical dynamics

In this section, we introduce previous studies that used TDVP for the uniform MPS to study thermalization and quantum many-body chaos [116, 117].

In these studies, the one-dimensional Ising model with longitudinal and transverse fields

$$\hat{H} = \sum_i J\sigma^z_i\sigma^z_{i+1} + h^z\sigma^z_i + h^x\sigma^x_i \tag{3.4.1}$$

has been investigated. Here, σ denotes the Pauli operator. This model is known to be non-integrable for finite h^z and integrable for zero h^z. Because of the simplicity and the tunability of the integrability, many studies about quantum many-body thermalization have been carried out for this model [15, 150–152].

In Ref. [117], long-time dynamics of this model up until the thermalization was calculated by TDVP for MPS. In general, an MPS-based real-time simulation requires exponentially large bond dimensions with the time because of the linear growth of the entanglement entropy [153]. On the other hand, the late-time dynamics near the thermalization should be characterized by emergent classical hydrodynamics since the thermal state is characterized by local observables, as we show in Section 2.1.1. In Ref. [117], the chaotic semiclassical dynamics obtained by TDVP for MPS was shown to be a good approximation of the emergent hydrodynamics. This is because the TDVP dynamics is chaotic and conserves all local symmetries. They calculated the real-time evolution with several bond dimensions and checked the convergence. If we focus on the time evolution of the entanglement entropy, it does not converge with increasing bond dimension. It grows linearly with time and saturates around the maximum value proportional to the log of the bond dimensions. However, the time evolution of classical quantities like local observables and energy transport converged well for a small bond dimension around $D = 4$.

In [116], the Lyapunov exponent and the Kolmogorov-Sinai (KS) entropy [154], the sum of the positive Lyapunov exponents of TDVP for MPS, were investigated for several bond dimensions. They obtained a scaling relation between the bond dimension and the KS entropy. They also derived a scaling relation between the saturated entanglement entropy and the bond dimension. They speculated the relationship between the KS entropy, the bond dimension, and the increase rate of entanglement entropy. By combining them, they obtained a differential equation of the entanglement entropy. The resulting differential equation can explain the crossover between the initial entanglement growth described by semiclassical chaos with strong nonlinearity and the late-time entanglement growth obtained by many-body chaos theory like the ETH.

In both researches, the scaling analysis of the bond dimension occupies an important position. In general, the extrapolation of the bond dimension is necessary to obtain accurate results with the uniform MPS in the thermodynamic limit. This kind of extrapolation has been studied well in the field of the ground-state calculation [155–157].

4 | Numerical Exploration of Periodic Orbits

In this chapter, we explain our algorithm to explore periodic orbits in uniform MPS manifolds and show the results. In Section 4.1, we introduce the objective of our exploration. In Section 4.2, we describe the strategy and details of our algorithm. In Section 4.3, we show the obtained result and discussions.

4.1 Objective

As we saw in Section 2.2.2, the analysis of the quantum-classical correspondence in QMBS based on TDVP for MPS plays a significant role in understanding QMBS in depth. However, as emphasized in Section 3.4, to properly understand the thermodynamic limit behavior with this approach, extrapolation of the bond dimension is necessary. Previous studies of QMBS have lacked this perspective. Our research aims to fill this gap. For this purpose, as a first step, we investigate the properties of periodic orbits in semiclassical dynamical systems obtained by TDVP for uniform MPS manifold with general bond dimensions. The first obstacle of this study is the difficulty in finding periodic orbits in the manifolds with large bond dimensions. Large dimensions of manifolds make it impossible to draw flow diagrams or Poincaré maps, which help us find periodic orbits manually with human eyes and have been used in the previous studies of the PXP model discussed in Section 2.2.2. Thus, we have to construct an algorithm to mechanically find periodic orbits in the MPS manifold. To show the validity of our method, we apply it to the PXP model.

4.2 Strategy of exploration

In the study of chaotic dynamical systems, researchers have found efficient algorithms to find periodic orbits numerically [158–160]. These algorithms are designed for dynamical systems in flat spaces like the Lorenz system in $\mathbb{R}^3$. In these algorithms, we consider the time-evolution function from $\mathbf{x}_0$ with time T denoted by $f(T, \mathbf{x}_0)$ and try to solve $\mathbf{x}_0 = f(T, \mathbf{x}_0)$. Since it is impossible to obtain the exact formula of f, we consider linearization of f around $(T, \mathbf{x}_0)$ and solve it approximately. Since the result does not indicate an accurate periodic orbit at this time, we repeat this step until convergence and obtain the final result. This method is called the Newton-Raphson-Mees algorithm. However, we cannot simply apply this method to our problem. In TDVP for MPS, we have to consider a curved manifold with gauge degrees of freedom. Because of the unitary gauge degrees of freedom, $A_0 \neq f(T, A_0)$ can hold even when A_0 and $f(T, A_0)$ denote the equivalent state even after gauge fixing.

To overcome this difficulty, we consider the optimization problem instead. We define a cost function $\mathrm{cost}(A, T)$ as the difference between $|\psi(A(0))\rangle$ and $|\psi(A(T))\rangle$ where $|\psi(A(t))\rangle$ denotes a trajectory satisfying $A(0) = A$ obtained by TDVP. The initial state A and the period of orbits T are obtained so as to minimize the cost function. We can avoid the problem caused by gauge degrees of freedom by defining the gauge-invariant cost function. This optimization-based approach has another advantage. Time evolution and energy optimization of MPS have been

investigated extensively so far. We can divert the knowledge of optimization algorithms for the MPS by considering our problem as an optimization problem. However, a lot of ingenuity is required to make this approach actually work. In this section, we discuss them.

In Section 4.2.1, we discuss the relation between the dynamics of the PXP model in the constrained and unconstrained Hilbert space. In Section 4.2.2, we introduce a subspace of MPS with zero energy expectation value. In Section 4.2.3, we discuss the concrete formulation of the distance between two MPSs. In Sections 4.2.4 and 4.2.5, we introduce two important concepts of numerical optimization, a continuous optimization on Riemannian manifolds and automatic differentiation. In Section 4.2.6, we will discuss how to prepare the initial state of the optimization.

4.2.1 Time evolution in projected space

In our exploration, we consider states with unit cells of two sites. Thus, we regard two adjacent sites as a single site as $|\circ\bullet\rangle_i \coloneqq |\circ\rangle_{2i-1} \otimes |\bullet\rangle_{2i}$. The local Hilbert space $\mathcal{H}_i$ of this paired site is defined as $\mathcal{H}_i \coloneqq \mathrm{span}\{|\circ\circ\rangle_i, |\circ\bullet\rangle_i, |\bullet\circ\rangle_i\}$, where the adjacent excitation $|\bullet\bullet\rangle_i$ is excluded because of the constraint $\hat{\mathcal{P}}_{\mathrm{RB}}$. We rewrite the Hamiltonian of the PXP model defined in Eq. (2.2.4) to the nearest neighbor interacting Hamiltonian as

$$\begin{aligned}
\hat{H}_{\mathrm{PXP}} &= \sum_{j=1}^{2N} |\circ\rangle\langle\circ|_{j-1} \otimes (|\circ\rangle\langle\bullet|_j + |\bullet\rangle\langle\circ|_j) \otimes |\circ\rangle\langle\circ|_{j+1} \\
&= \sum_{i=1}^{N} (|\circ\circ\rangle\langle\circ\bullet|_i + |\circ\bullet\rangle\langle\circ\circ|_i) \otimes (|\circ\circ\rangle\langle\circ\circ|_{i+1} + |\circ\bullet\rangle\langle\circ\bullet|_{i+1}) \\
&\quad + (|\circ\circ\rangle\langle\circ\circ|_i + |\bullet\circ\rangle\langle\bullet\circ|_i) \otimes (|\circ\circ\rangle\langle\bullet\circ|_{i+1} + |\bullet\circ\rangle\langle\circ\circ|_{i+1}) \\
&=: \sum_{i=1}^{N} \hat{h}_{i,i+1},
\end{aligned} \tag{4.2.1}$$

where j denote the index of the original site and i denote that of the redefined one. We also rewrite the projection operator $\hat{\mathcal{P}}_{\mathrm{RB}}$ defined in Eq. (2.2.3) as

$$\begin{aligned}
\hat{\mathcal{P}}_{\mathrm{RB}} &= \prod_{j=1}^{2N} (\hat{1}_{j,j+1} - |\bullet\rangle\langle\bullet|_j \otimes |\bullet\rangle\langle\bullet|_{j+1}) \\
&= \mathrm{Tr}\left[\prod_{i=1}^{N} \begin{pmatrix} 1 - |\circ\bullet\rangle\langle\circ\bullet|_i & |\circ\bullet\rangle\langle\circ\bullet|_i \\ |\circ\circ\rangle\langle\circ\circ|_i & |\circ\bullet\rangle\langle\circ\bullet|_i \end{pmatrix} \right].
\end{aligned} \tag{4.2.2}$$

The projected Hilbert space of $\hat{\mathcal{P}}_{\mathrm{RB}}$ cannot be considered as the product of local Hilbert spaces since the pattern $|\circ\bullet\rangle_i \otimes |\bullet\circ\rangle_{i+1}$ is eliminated. On the other hand, an MPS represents a state of the total Hilbert space $\bigotimes_i \mathcal{H}_i$. Thus, we have to fill this gap to obtain the TDVP dynamics on the projected Hilbert space.

There are two strategies to obtain the dynamics on the projected Hilbert space by using TDVP for MPS. The first idea is to replace the variational manifold $\{|\psi(A)\rangle\}$ by the projected one $\{\hat{\mathcal{P}}_{\mathrm{RB}}|\psi(A)\rangle / \|\hat{\mathcal{P}}_{\mathrm{RB}}|\psi(A)\rangle\|\}$, where $|\psi(A)\rangle$ denotes the ordinary uniform MPS. The previous study we discussed in Section 2.2.2 can be regarded as the $D = 1$ case of this strategy. The problem of it is that the numerical calculation based on this idea is inefficient and hard to apply for large D. In ordinary TDVP for MPS, we can skip calculating the inverse of the Gram matrix defined in Eq. (3.3.5) by considering the parameterization $B(X)$ of the tangent vector, which makes the Gram matrix proportional to the identity matrix. We can no longer use this technique for the projected variational manifold and have to calculate the inverse of the Gram matrix explicitly in each time step. It makes the calculation very inefficient and unstable.

Therefore, we adopt the other approach in this study. In the exact quantum mechanics of the PXP model, if the time-dependent state $|\psi(t)\rangle$ satisfies the Schrödinger equation, $\hat{\mathcal{P}}_{\mathrm{RB}}|\psi(t)\rangle$ also satisfies it, owing to the linearity of the quantum mechanics and the commutation relation $[\hat{\mathcal{P}}_{\mathrm{RB}}, \hat{H}_{\mathrm{PXP}}] = 0$. The second strategy is based on this fact. First, we consider the TDVP dynamics $|\psi(A(t))\rangle$ defined on the total Hilbert space $\bigotimes_i \mathcal{H}_i$. As we mentioned, the total Hilbert space contains the patterns with the adjacent excitation $|\circ\bullet\rangle|\bullet\circ\rangle$. We note that this pattern cuts the Hamiltonian $\hat{H}_{\mathrm{PXP}}$ into two independent parts as

$$\begin{aligned}&\hat{H}_{\mathrm{PXP}}(\dots|\circ\bullet\rangle|\circ\circ\rangle|\circ\bullet\rangle|\bullet\circ\rangle|\bullet\circ\rangle|\circ\circ\rangle\dots)\\&=\hat{H}_{\mathrm{PXP}}(\dots|\circ\bullet\rangle|\circ\circ\rangle|\circ\bullet\rangle)\otimes\hat{H}_{\mathrm{PXP}}(|\bullet\circ\rangle|\bullet\circ\rangle|\circ\circ\rangle\dots),\end{aligned} \tag{4.2.3}$$

since $\hat{h}_{i,i+1}|\circ\bullet\rangle_i|\bullet\circ\rangle_{i+1} = 0$ holds. After that, we obtain the dynamics on the projected Hilbert space as $\hat{\mathcal{P}}_{\mathrm{RB}}|\psi(A(t))\rangle$. In this approach, we can skip the calculation of the Gram matrix.

The problem of the second approach is that the norm of $\hat{\mathcal{P}}_{\mathrm{RB}}|\psi(A(t))\rangle$ is not conserved in the ordinary TDVP dynamics as discussed in Section 3.3.3. It makes the analysis in Chapter 5 very complicated. This is because the projection operator $\hat{\mathcal{P}}_{\mathrm{RB}}$ is a non-local operator represented as the matrix product operator. Here, we can use the conservation law enforcing discussed in Section 3.1.2 to overcome this problem. As we already mentioned, the enforcement of conservation laws may cause a violation of energy conservation. In our case, by considering zero-energy subspace as we discuss in Section 4.2.2, we can guarantee energy conservation. Although the second approach seems less natural than the first one, it is efficient and works well for large bond dimensions.

4.2.2 Zero-energy subspace

In the previous study reviewed in Section 2.2.2, we consider the zero-energy subspace of the variational manifold by fixing the phase factor $\phi = 0$. In the same manner, we consider the zero-energy subspace of the MPS manifold and restrict our optimization in it. To obtain the zero-energy subspace, we define a local unitary operator $\hat{R}_i$ acting on unit cell i as

$$\hat{R}_i := |\circ\circ\rangle\langle\circ\circ|_i - \mathrm{i}|\circ\bullet\rangle\langle\circ\bullet|_i - \mathrm{i}|\bullet\circ\rangle\langle\bullet\circ|_i, \tag{4.2.4}$$

and define a state with tilde as

$$|\widetilde{\psi}\rangle := \hat{\mathcal{R}}|\psi\rangle := \prod_i \hat{R}_i|\psi\rangle. \tag{4.2.5}$$

We define the transformed Hamiltonian $\hat{J}_{\mathrm{PXP}}$ as the sum of local operators $\hat{j}_{i,i+1}$:

$$\hat{J}_{\mathrm{PXP}} = \sum_i \hat{j}_{i,i+1} := \mathrm{i}\hat{\mathcal{R}}\hat{H}_{\mathrm{PXP}}\hat{\mathcal{R}}^\dagger = \sum_i \hat{R}_i\hat{R}_{i+1}\hat{h}_{i,i+1}\hat{R}_i^\dagger\hat{R}_{i+1}^\dagger. \tag{4.2.6}$$

The equation of motion of $|\widetilde{\psi}\rangle$ can be written as

$$|\dot{\widetilde{\psi}}\rangle = -\hat{J}_{\mathrm{PXP}}|\widetilde{\psi}\rangle \tag{4.2.7}$$

by considering

$$\hat{\mathcal{R}}(|\dot{\psi}\rangle + \mathrm{i}\hat{H}_{\mathrm{PXP}}|\psi\rangle) = |\dot{\widetilde{\psi}}\rangle + \mathrm{i}\hat{\mathcal{R}}\hat{H}_{\mathrm{PXP}}\hat{\mathcal{R}}^\dagger|\widetilde{\psi}\rangle = |\dot{\widetilde{\psi}}\rangle + \hat{J}_{\mathrm{PXP}}|\widetilde{\psi}\rangle = 0. \tag{4.2.8}$$

We note that all matrix elements of $\hat{j}$ are real:

$$\begin{aligned}\hat{j}_{i,i+1} = &(|\circ\circ\rangle\langle\circ\bullet|_i - |\circ\bullet\rangle\langle\circ\circ|_i)\otimes(|\circ\circ\rangle\langle\circ\circ|_{i+1} + |\circ\bullet\rangle\langle\circ\bullet|_{i+1})\\&+(|\circ\circ\rangle\langle\circ\circ|_i + |\bullet\circ\rangle\langle\bullet\circ|_i)\otimes(|\circ\circ\rangle\langle\bullet\circ|_{i+1} - |\bullet\circ\rangle\langle\circ\circ|_{i+1}).\end{aligned} \tag{4.2.9}$$

Now, let us consider the following relation:

$$\langle\psi|\hat{H}_{\mathrm{PXP}}|\psi\rangle = -\mathrm{i}\langle\widetilde{\psi}|\hat{J}_{\mathrm{PXP}}|\widetilde{\psi}\rangle. \tag{4.2.10}$$

The left-hand side is surely real. Here, we assume that $|\widetilde{\psi}\rangle$ is described by uniform MPS with tensor $A \in \mathbb{R}^{D\times D\times 3}$. Then, the right-hand side is pure imaginary because all the elements of $|\widetilde{\psi}\rangle$ and $\hat{J}_{\mathrm{PXP}}$ are real. By combining these results, we can conclude $\langle\psi|\hat{H}|\psi\rangle = \langle\widetilde{\psi}|\hat{J}_{\mathrm{PXP}}|\widetilde{\psi}\rangle = 0$ in this case.

Thus, hereafter we consider the manifold of real-valued uniform MPS and consider the dynamics Eq. (4.2.7).

4.2.3 Cost function

The objective function of our optimization is defined as $\mathrm{cost}(A(0), T) \coloneqq d(A(0), A(T))$, where d denotes a distance-like function satisfying $d(A, A') \geq 0$ and $d(A, A') = 0 \Leftrightarrow |\psi(A)\rangle \sim |\psi(A')\rangle$. Here, $A(T)$ is obtained by the TDVP equation. The problem is how to choose the function d. The simplest way is to consider the inner product

$$\langle\psi(A')|\psi(A)\rangle = \mathrm{Tr}[(\mathcal{T}_{A'}^{A})^N] \approx \lambda_{\mathrm{LM}}(\mathcal{T}_{A'}^{A})^N. \tag{4.2.11}$$

In the thermodynamic limit, $\langle\psi(A')|\psi(A)\rangle$ takes a finite value only when $|\lambda_{\mathrm{LM}}(\mathcal{T}_{A'}^{A})| = 1$. Thus, we can define the distance function as

$$d(A, A') = -\ln|\lambda_{\mathrm{LM}}(\mathcal{T}_{A'}^{A})|. \tag{4.2.12}$$

Finally, we use this simple cost function in our optimization.

In the present study, we also consider other distance functions that are more sensitive to the difference. We assume that the two tensors A and A' are left canonical and related by the gauge transformation as

$$(1_{D\times D}|\mathcal{T}_{A}^{A} = (1_{D\times D}|\mathcal{T}_{A'}^{A'} = (1_{D\times D}|, \quad UAU^{-1} = A', \tag{4.2.13}$$

where U is proportional to some unitary matrix. Then, we can obtain U by solving the dominant eigenvalue problem because of the following equation:

$$(U|\mathcal{T}_{A'}^{A} = (1_{D\times D}|\mathcal{T}_{A'}^{UAU^{-1}U} = (1_{D\times D}|\mathcal{T}_{A'}^{A'U} = (1_{D\times D}|\mathcal{T}_{1}^{U} = (U|. \tag{4.2.14}$$

Therefore, for given A and A', we define a distance-like function as follows:

$$d_g(A, A') = \|UA - A'U\| \tag{4.2.15}$$

where U is obtained by solving the dominant eigenvalue problem of $\mathcal{T}_{A'}^{A}$. Note that the choice of the norm is arbitrary. The unitarity of U defined as

$$d_u(A, A') = \left\| \frac{UU^\dagger}{\|UU^\dagger\|} - \frac{1_{D\times D}}{\|1_{D\times D}\|} \right\| \tag{4.2.16}$$

is also useful to measure the difference. We use d_g and d_u with the Frobenius norm to verify the recurrence of our results.

4.2.4 Continuous optimization on a Riemannian manifold

Here, we use a matrix form of tensor $\mathcal{A}_{(l,s),r} = A^s_{l,r}$. The optimization problem we have to solve can be written as a constrained optimization problem

$$\underset{\substack{\mathcal{A}\in\mathbb{R}^{3D\times D}\\ T\in\mathbb{R}^{>\epsilon}}}{\text{minimize}} \quad \text{cost}(\mathcal{A}, T) \quad \text{subject to} \quad \mathcal{A}^\dagger\mathcal{A} = 1_{D\times D}, \tag{4.2.17}$$

where $\mathbb{R}^{>\epsilon}$ denotes $\{x \in \mathbb{R} : x > \epsilon\}$ with small positive ϵ to eliminate the trivial result $\text{cost}(\mathcal{A}, 0) = 0$. The set of matrices satisfying $\mathcal{A}^\dagger\mathcal{A} = 1_{D\times D}$ can be regarded as a Riemannian matrix manifold called the Stiefel manifold $\text{St}(3D, D)$. Thus, we can rewrite our optimization problem as an unconstrained optimization problem

$$\underset{(\mathcal{A},T)\,\in\,\text{St}(3D,D)\times\mathbb{R}^{>\epsilon}}{\text{minimize}} \text{cost}(\mathcal{A}, T). \tag{4.2.18}$$

When a continuous function is defined on a manifold, we can use continuous optimization algorithms on the Riemannian manifold, which have been well investigated in recent years [161–165].

Before discussing the optimization on the manifold, we briefly review the continuous optimization on the flat Euclid space [166]. We consider an objective function $f : \mathbb{R}^n \to \mathbb{R}$ to minimize. The steepest-decent method is a fundamental method for obtaining the minimum of f numerically. First, we take some initial point $\mathbf{x}_0 \in \mathbb{R}^n$ and calculate $f(\mathbf{x}_0)$ and $\nabla f(\mathbf{x}_0)$. We define the steepest-decent direction $\mathbf{d}_0$ as $\mathbf{d}_0 = -\nabla f(\mathbf{x}_0)/\|\nabla f(\mathbf{x}_0)\|$. Then, we define a single argument function $g_0(\alpha) \coloneqq f(\mathbf{x}_0 + \alpha\mathbf{d}_0)$. Ideally, we solve the one-argument minimization $\alpha_0 = \arg\min_\alpha g_0(\alpha)$ and obtain the updated point $\mathbf{x}_1 = \mathbf{x}_0 + \alpha_0\mathbf{d}_0$. In practice, we try to numerically obtain α_0 making the decrease $g(0) - g(\alpha_0)$ large enough. This step is called line search. Because of the definition of $g_0(\alpha)$, $0 > g_0'(0)$ holds and $g_0(0) > g_0(\alpha)$ is guaranteed for enough small $\alpha > 0$. However, a too-small value of α makes the optimization inefficient. On the other hand, a too large value of α may not satisfy $g_0(0) > g_0(\alpha)$. Some heuristic conditions, such as the Armijo condition, Wolfe condition, and Goldstein condition, are known to check that α is large enough and not too large. A typical strategy to determine α is called the backtracking method: take a large α first and check the condition. If the condition holds, we adopt it as α_0. If the condition does not satisfy, we reduce α to $\rho\alpha$ with $0 < \rho < 1$, and check the condition again. After obtaining α_0, we update the point as $\mathbf{x}_1 = \mathbf{x}_0 + \alpha_0\mathbf{d}_0$ and go to the next iteration. Once $\mathbf{x}_k$ satisfies $\|\nabla f(\mathbf{x}_k)\| < \epsilon$ with given threshold ϵ, we stop the iteration.

Although the idea of the steepest descent method is simple and fundamental for continuous optimization, the convergence becomes slow for ill-conditioned cases; in other words, the case of the contour line of the objective function around the extrema becomes thin as depicted in Fig. 4.1. We can overcome this problem by using the conjugate-gradient (CG) method or the (quasi-)Newton method. If we can efficiently calculate the Hessian of f, the Newton method can be a good choice. In the Newton method, we approximate the objective function by the second-order Taylor expansion and calculate the minimum point of the polynomial. In each step, we would have to calculate the inverse of the Hessian. Both the CG method and the quasi-Newton method have been developed to skip the calculation of Hessian and its inverse. In the CG method, we determine the search direction $\mathbf{d}_i$ by approximating the Newton method's update direction combining $\mathbf{d}_{i-1}$, $\nabla f(\mathbf{x}_{i-1})$, and $\nabla f(\mathbf{x}_i)$. In the quasi-Newton method, on the other hand, we approximate the inverse of Hessian by a positive definite matrix obtained from the previous gradients and the search directions. The Limited-memory Broyden-Fletcher-Goldfarb-Shanno (L-BFGS) method is a well-known method to approximate the positive definite matrix in the quasi-Newton method. In the L-BFGS method, we record only m recent gradients and search directions and discard the oldest one as the iteration proceeds.

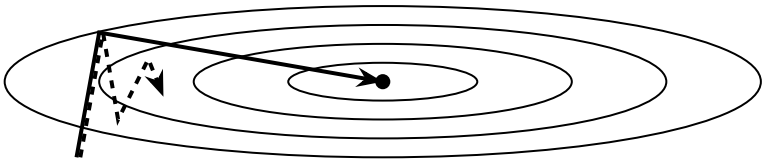

Figure 4.1: Schematic picture of gradient decent algorithms for ill-conditioned cases. A dashed line denotes the steepest-decent method. In the CG method and the L-BFGS method, the search direction is corrected to the direction to the minimum point as a solid line.

Next, let us consider the continuous optimization on a Riemannian manifold. On a Riemannian manifold, we can define the distance between two points by considering the metric. A geodesic $\gamma_0(t)$ of the manifold $\mathcal{M}$ is defined as a curve on the manifold that connects given two points $x_0 = \gamma_0(0)$ and $x_1 = \gamma_0(1)$ with the smallest distance. It is a counterpart of a straight line in the Euclid space. We can define the geodesic on the manifold from the initial point x_0 and the velocity vector $v_0 = \dot{\gamma}_0(0)$ defined on the tangent space of the initial point. A point transport along this geodesic is called the exponential map as $x_1 = \exp_{x_0}(v_0)$ depicted in Fig. 4.2. In the continuous optimization on the Riemannian manifold, we replace the line search on Euclid space by the search along the geodesic with the exponential map. By this replacement, we can generalize the steepest-descent algorithm to the manifold. We note that the geodesic depends on the choice of metric. In the CG or L-BFGS method, we use the information of the gradients and the search directions in the previous steps to determine the next search direction. However, the directions and gradients are defined as the tangent vector on different points of manifold. Thus, we have to consider the transport of the tangent vector to generalize the CG or L-BFGS methods. If two points x_0 and x_1 on the manifold are connected by a curve γ, we can consider a parallel transport of the tangent vector along the curve $\Gamma^{\gamma}_{x_0 \to x_1}$. The CG and L-BFGS algorithms on the manifold are defined by considering a parallel transport along a geodesic.

In some cases, the calculation of exponential maps and parallel transports becomes inefficient. A retraction $R_{x_0}(v)$ is an approximation of an exponential map that behaves similar to the exponential map up to the first order. A vector transport τ_{x_0,v_0} is defined as an approximation of parallel transport. These approximations are often used to solve real-world problems. We depicted the schematic pictures of retraction and vector transport in Fig. 4.2.

Application of optimization in Riemannian manifolds to the isometric tensor network states, including a canonical form of MPS, has been actively discussed in recent years [122, 127]. To implement these algorithms, we used the package OptimKit.jl [167].

4.2.5 Automatic differentiation

In the continuous optimization method discussed in Section 4.2.4, we would have to know the gradients of the cost functions. In our case, the cost function is defined through numerical dynamics. Thus, it is impossible to write down an explicit form of the gradient. In such a case, one of the simplest choices is to use the numerical differentiation that estimates the derivatives by the finite-difference calculation. However, the accuracy and efficiency of numerical differentiation are not sufficient for our optimization. The time evolution in the present simulation is a combination of a considerable number of simple tensor operations such as contraction, multiplication, QR decomposition, and solving linear equations. Since we know the differentiation rules of each operation, we can mechanically obtain the derivative in principle. This dependency structure of elemental functions is called the computational graph. By using the chain rule of differentiation, we can obtain a computational graph of the gradient systematically. This method is called symbolic differentiation, implemented in various computer

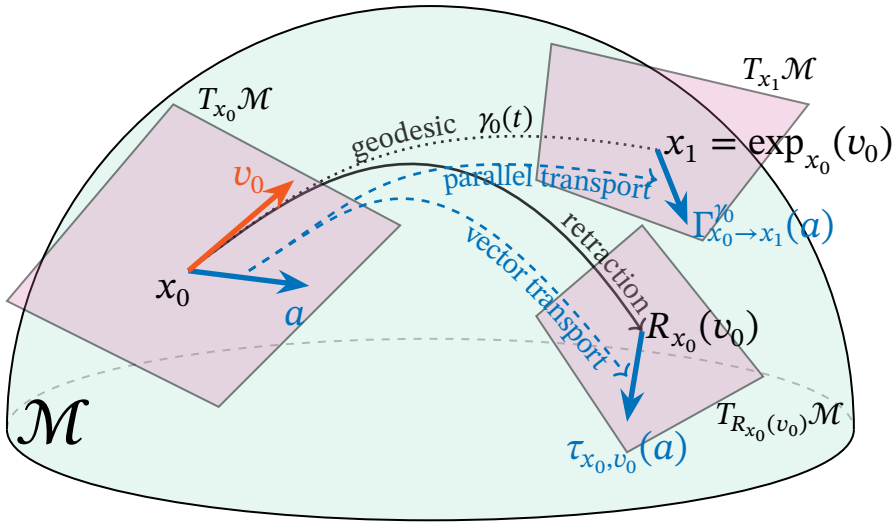

Figure 4.2: Schematic picture of retraction and vector transport

algebra systems such as Mathematica, MATLAB, and SymPy [168]. However, it is impractical to use symbolic differentiation to obtain a gradient of the complicated cost function in the present problem, since the computational graph of the gradient becomes huge. To carry out the optimization, we only need to know the value of the gradient, not the symbolic expression. In the automatic differentiation (AD) method [169], we calculate the gradient by combining the chain rule and the differential rules of elemental functions as well as the symbolic differentiation. However, in contrast to the symbolic one, we transform a computer program corresponding to the cost function into a program that calculates its gradient.

There are two kinds of implementation of AD, the forward mode and the backward mode. If the input parameter dimension is larger than the output dimension, the backward mode is more efficient. Since this is a typical situation in machine learning using neural networks, a number of high-performance AD libraries have been developed as open-source machine learning frameworks; Pytorch [170], TensorFlow [171], Jax [172], and Zygote.jl [173].

As an example, let us consider a function $J(F(G(x), H(x)), I(x)) \in \mathbb{R}$, where x and the output of F, G, H, I can be arrays or sets of arrays. For simplicity, we denote the value of each function by a small letter as $g = G(x)$ and $f = F(g, h)$. We define the adjoint form as $\overline{\star} := \partial J/\partial \star$. Here obviously $\bar{J} = 1$ holds. When the set of values $(y_1, \ldots, y_k)$ depends on x,

$$\bar{x} = \frac{\partial J}{\partial x} = \sum_i \frac{\partial J}{\partial y_i}\frac{\partial y_i}{\partial x} = \sum_i \bar{y}_i \frac{\partial y_i}{\partial x} \tag{4.2.19}$$

holds. In other words, $\bar{x}$ is obtained by the vector-Jacobian product of its children. Our purpose is to obtain $\bar{x} = \partial J/\partial x$. In the backward mode AD, we define differentiation rule of function $z = Z(x)$ as a functional that returns a function calculating the vector-Jacobian product $Z_{\mathrm{vjp}}[x]$ defined as

$$Z_{\mathrm{vjp}}[x](\bar{z}) = \bar{z}\frac{\partial z}{\partial x}. \tag{4.2.20}$$

In our example, first we calculate j and record the intermediate values f, g, h, i. Since the children of x are g, h, i, it holds that

$$\bar{x} = \bar{g}\frac{\partial g}{\partial x} + \bar{h}\frac{\partial h}{\partial x} + \bar{i}\frac{\partial i}{\partial x} = G_{\mathrm{vjp}}[x](\bar{g}) + H_{\mathrm{vjp}}[x](\bar{h}) + I_{\mathrm{vjp}}[x](\bar{i}). \tag{4.2.21}$$

Furthermore, $(\bar{g}, \bar{h}) = F_{\mathrm{vjp}}[(g,h)](\bar{f})$ holds since f is the only child of the pair (g,h). Similarly, $(\bar{f}, \bar{i}) = J_{\mathrm{vjp}}[(f,i)](\bar{j}) = J_{\mathrm{vjp}}[(f,i)](1)$ holds. By using these equations in the reverse direction, we can calculate the value of $\bar{x} = \partial J/\partial x$. Zygote.jl, an AD library for the programming language Julia [174], realizes the backward AD by the compile-time transformation of the program. In the simulation in the present thesis, we use Zygote.jl for evaluating the gradient of our cost function.

The application of AD is one of the currently most debated issues in tensor-network community. In appendix A, we present the differentiation rules needed for tensor-network algorithms, including TDVP.

4.2.6 Initial state preparation

Since gradient-based methods can easily be stacked at a local minimum of the cost function, it is necessary to prepare a good initial state near the global minimum. In our problem, we can use the result of the restricted $D = 2$ MPS discussed in Chapter 2. We use this state as the initial state of the optimization in the general $D = 2$ MPS manifold.

Note that preparing an initial state with larger bond dimensions is not very straightforward. MPS with bond dimension D can be regarded as an MPS with bond dimension $D + \Delta D$ naturally. However, it is nontrivial to obtain canonical $D + \Delta D$ MPS from D MPS denoted by $\{A_{\mathrm{L}}, A_{\mathrm{R}}, A_{\mathrm{C}}, C\}$. We use the method called the subspace expansion for this purpose [145, 175, 176]. Here, we consider $\mathcal{B}_{(l,s),(r,t)} = B^{s,t}_{l,r}$ defined in Eq. (3.3.23) and its SVD $\mathcal{B}_{(l,s),(r,t)} = \sum_x \mathcal{U}_{(l,s),x} \Sigma_x \mathcal{V}_{x,(r,t)}$. We assume that the singular value Σ is ordered in descent order. Then, we can obtain $D \times \Delta D \times d$ tensor $U^s_{l,x}$ and $\Delta D \times D \times d$ tensor $V^s_{x,r}$ by restricting x from 1 to ΔD. Then, we can obtain the mixed canonical MPS with bond dimension $D + \Delta D$

$$\tilde{A}^s_{\mathrm{L}} = \begin{pmatrix} A^s_{\mathrm{L}} & U^s \\ 0_{\Delta D \times D} & 0_{\Delta D \times \Delta D} \end{pmatrix}, \quad \tilde{A}^s_{\mathrm{R}} = \begin{pmatrix} A^s_{\mathrm{R}} & 0_{D \times \Delta D} \\ V^s & 0_{\Delta D \times \Delta D} \end{pmatrix}, \quad \tilde{C} = \begin{pmatrix} C & 0_{D \times \Delta D} \\ 0_{\Delta D \times D} & 0_{\Delta D \times \Delta D} \end{pmatrix}. \tag{4.2.22}$$

However, this enlarged MPS is not optimal for the initial state since this state is singular, i.e., $\tilde{C}$ is non-invertible. Thus, we first calculate the time evolution for a while as depicted in Fig. 4.3. Here, we consider the pseudo-inverse of $\tilde{C}$ instead of the inverse. Thus, the time is the parameter of the initial state.

4.3 Numerical results

We have succeeded in finding periodic orbits in the cases $D = 2, 3, 4$. In Section 4.3.1, we compare the optimization algorithms and different ways of preparing initial states. In Section 4.3.2, we discuss the properties of the periodic orbits that we obtained.

4.3.1 Optimization

First, we show the results of our optimization. In Fig. 4.4, we compare four optimization algorithms. As a benchmark problem, we consider optimization of the cost function for the $D = 3$ manifold. The result suggests that the L-BFGS method with enough large history size is optimal for our problem. The steepest-descent method does not converge in a reasonable number of steps. The CG method, which is roughly equivalent to $m = 1$ L-BFGS, converges but takes more steps. By comparing the L-BFGS method with $m = 10$ and $m = 100$, the latter makes the convergence more than twice faster. In the case $m = 100$, the number of steps until convergence is smaller than the history size. From this benchmark result, we decided to use the L-BFGS method with history size $m = 100$. This history size $m = 100$ is relatively larger

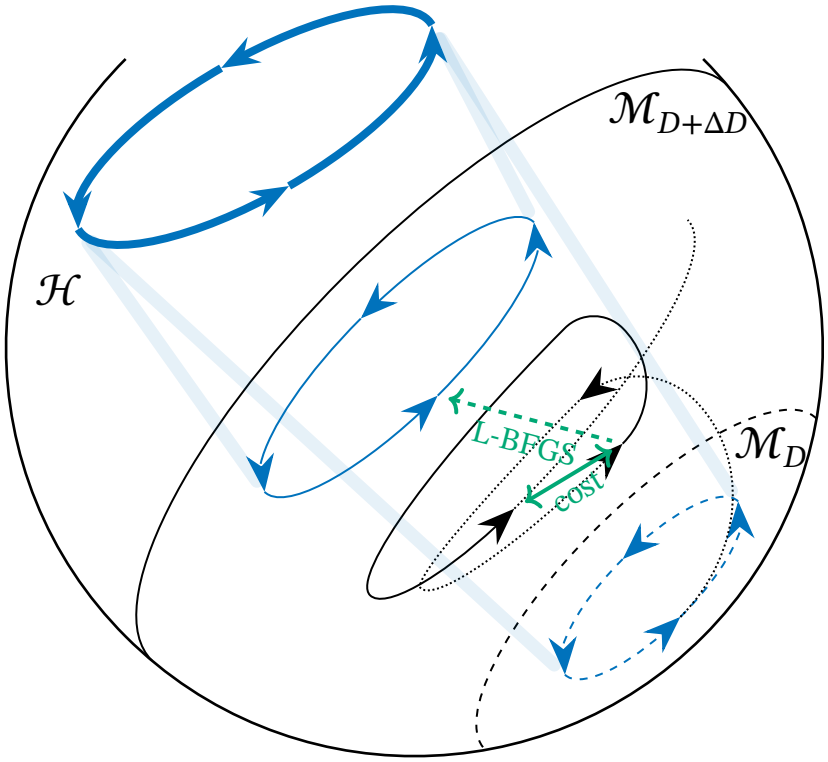

Figure 4.3: Schematic picture of optimization and initial-state preparation. We start from a periodic orbit in $\mathcal{M}_D$, a uniform MPS manifold with bond dimension D. We regard a state in this orbit as a state in $\mathcal{M}_{D+\Delta D}$ by using the subspace-expansion method. Then, we perform the real-time evolution in $\mathcal{M}_{D+\Delta D}$ for a while and obtain the initial state of the optimization. By repeating this process and obtaining a series of periodic orbits, we can approach an authentic periodic orbit in the total Hilbert space $\mathcal{H}$.

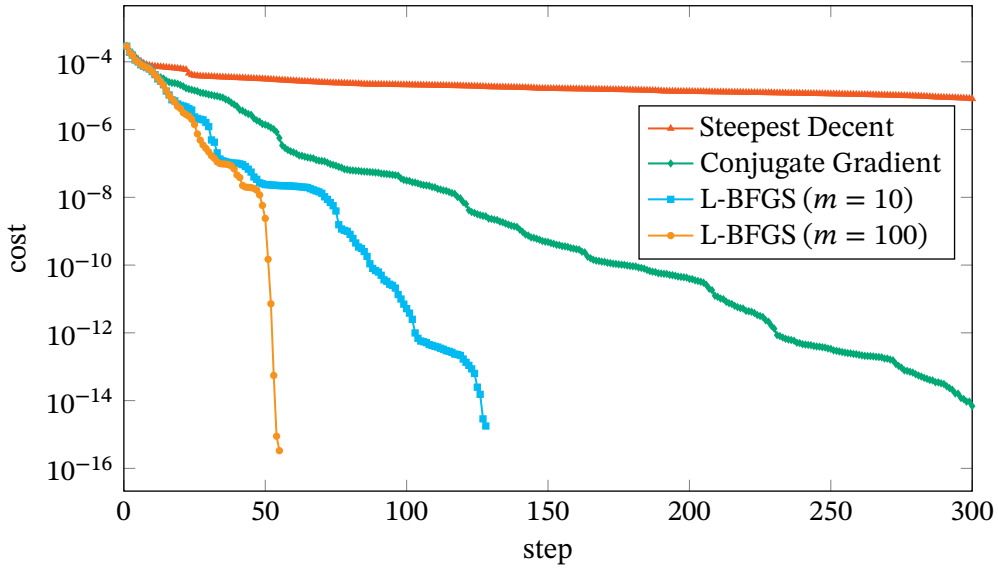

Figure 4.4: A comparison of convergence in optimizing the cost function of $D = 3$ uniform MPS using L-BFGS algorithms (with memory size 10 and 100), the CG algorithm, and the steepest-descent algorithm from a similar initial state. The initial state is prepared as follows: First, we choose a point on the periodic orbit in $D = 2$ and regard it as a state in $D = 3$ uniform MPS manifold by using subspace expansion. After that, the state is evolved in $D = 3$ manifold in one period of the original $D = 2$ periodic orbit.

than the well-known results in continuous optimization study, for which it is said that $m < 10$ is sufficient in general cases. One possible reason for this discrepancy is the dependence on the benchmark problems. In continuous optimization studies, researchers consider cost functions with huge degrees of freedom, for which the memory usage of the algorithm becomes a bottleneck. In our problem, the dimension of the manifold is not that large. Instead, we require high accuracy since our final purpose is to solve the equation $\mathrm{cost}(\mathcal{A}, T) = 0$.

In Fig. 4.5, we show the dependence of the optimization on the initial states. Here, we consider the optimization in $D = 4$, a more difficult task than the previous benchmark. We can see a strong dependence on the length of the time evolution after subspace expansion. We have not found a good heuristic method for determining the length of the time evolution in general cases. In the following, we try a grid search to obtain a good initial condition of the optimization.

We consider that the difficulty of preparing initial states is the reason why the optimization for $D > 4$ is not successful so far. One possible solution to this problem is using a more robust algorithm against local minima.

4.3.2 Periodic orbits

In our optimization, we succeeded to obtain periodic orbits in the uniform MPS manifolds with bond dimension $D = 2, 3, 4$.

In our TDVP calculation, there are several numerical parameters corresponding to the accuracy of the time evolution. The first one is the step number of the time evolution. We start the optimization with 5000 time steps. It corresponds to $\delta t = T/5000 \approx 4.7/5000 \approx 0.001$. After the cost function becomes smaller than the computer epsilon of double-precision floating-point number $\epsilon \approx 2.2 \times 10^{-16}$, we make the number of time steps twice larger. This change makes the evaluated cost a finite value smaller than 10^{-10}. We enlarged the step number

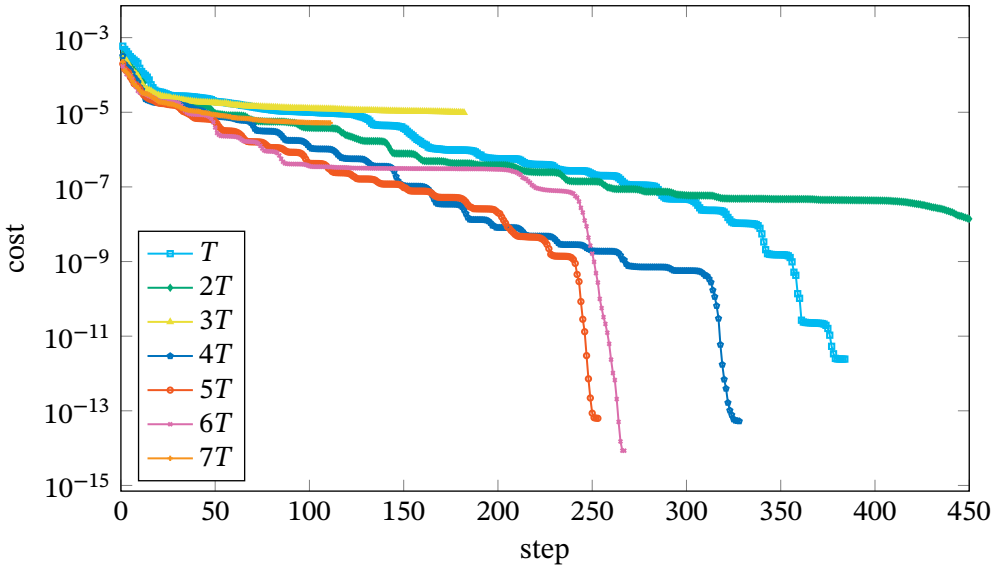

Figure 4.5: Comparison of convergence in optimizing the cost function of $D = 3$ uniform MPS using L-BFGS algorithm with memory size 100 from various initial states. The initial states are prepared as follows: First, we choose a point on the periodic orbit in $D = 2$ and regard it as a state in $D = 4$ uniform MPS manifold using subspace expansion. After that, the state is evolved in the $D = 4$ manifold in n times of the period of the original periodic orbit T in $D = 2$ where $n \in [1, 7] \cap \mathbb{N}$.

Fig. 2.4	$D = 2$	$D = 3$	$D = 4$
$1.51\pi \approx 4.7438$	4.7357	4.7259	4.7272

Table 4.1: Periods of periodic orbits.

as 10000 → 20000 → 40000 → 50000 and obtained converged results for each. The result of 50000 step is adopted as the final result. To verify the result, we calculated the cost of the obtained result with 100000 to 500000 steps and checked that the results behave non-monotonically with the step number and the values were sufficiently small around 10^{-14}. It suggests that we were not able to make the result more accurate by making the step number larger. The other parameter is the threshold of symmetric integration and canonicalization defined in Section 3.3.2. We take these values $\epsilon \times \sqrt{3D^2}$, where ϵ denotes the computer epsilon.

Now, let us discuss the physical properties of the periodic orbits that we obtained. In Table 4.1, we show their periods. These values are smaller than the value of the previous study and seem to converge around $T \approx 4.73$. The time evolution of the probabilities of the single-site measurement, i.e., the expectation values of $|\circ\circ\rangle\langle\circ\circ|$, $|\circ\bullet\rangle\langle\circ\bullet|$ and $|\bullet\circ\rangle\langle\bullet\circ|$, is shown in Fig. 4.6. These curves also well converge already in $D = 4$.

In the previous study [99] reviewed in Section 2.2.2, we considered the variational manifold parameterized by two real parameters. This manifold is a submanifold of the MPS manifold with $D = 2$. In this case, the periodic orbit goes through the $|\mathbb{Z}_2\rangle$ state exactly. In this section, we consider the MPS manifolds with the greater expressive power even in the case of $D = 2$. Thus, the periodic orbits that we obtained do not go through the $|\mathbb{Z}_2\rangle$ exactly but pass by it.

In Fig. 4.7, we show the time evolution of the quantum leakage. Compared to Fig. 2.4b,

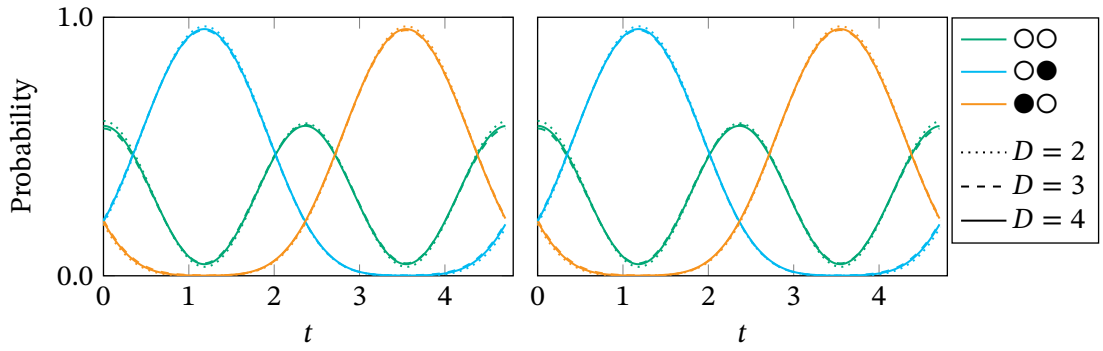

Figure 4.6: Time evolutions of the probabilities of the single-site measurement, i.e., the expectation values of $|\bigcirc\bigcirc\rangle\langle\bigcirc\bigcirc|$, $|\bigcirc\bullet\rangle\langle\bigcirc\bullet|$ and $|\bullet\bigcirc\rangle\langle\bullet\bigcirc|$, of periodic orbits that we found in $D = 2, 3, 4$: (left) probabilities of $|\psi(t)\rangle$. (right) probabilities of $\hat{\mathcal{P}}_{\mathrm{RB}}|\psi(t)\rangle/\|\hat{\mathcal{P}}_{\mathrm{RB}}|\psi(t)\rangle\|$.

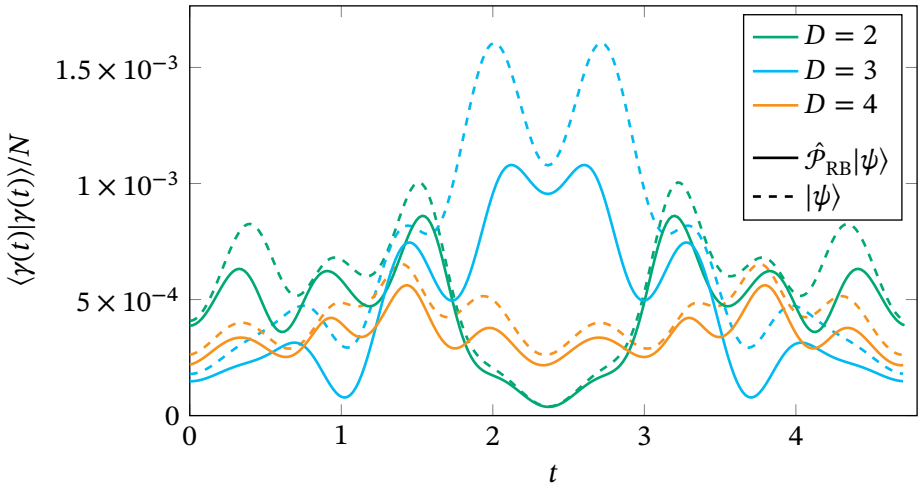

Figure 4.7: Time evolutions of leakages per unit-cell size calculated by Eq. (3.3.24) for periodic orbits that we found in $D = 2, 3, 4$. Dashed lines denote the leakages of the original states $|\psi(t)\rangle$ and solid lines denote those of the projected states $\hat{\mathcal{P}}_{\mathrm{RB}}|\psi(t)\rangle/\|\hat{\mathcal{P}}_{\mathrm{RB}}|\psi(t)\rangle\|$.

they take smaller values by a few orders of magnitude. Comparing the results of $D = 2$ and $D = 4$, we can see the decrease of the leakage in many moments. This result suggests the existence of a periodic orbit without leakage in $D \to \infty$. On the other hand, we can see that the orbit in $D = 2$ gives the smallest leakage at some moments around $t = 2$. To discuss the decrease of leakage, we have to consider some integrated values of them. In the previous study, the simple integral $\int_0^T \mathrm{d}t\sqrt{\langle\gamma(t)|\gamma(t)\rangle/N}$ had been discussed. In Chapter 5, we show that the weighted integral of leakage as a characteristic of each orbit and show the decrease. The leakage in the $D = 3$ orbit looks larger than the others. One possible reason for it is the parity of the bond dimension. In the calculation of the ground state, the results can become worse by increasing the bond dimension, if the increased dimension is incompatible with the symmetry. We infer that this kind of non-monotonic behavior is easy to occur in a small D region as we consider. Although the entanglement entropy depicted in Fig. 4.8 also shows the non-monotonic behavior, we can say the results converge here.

Finally, we show the time evolution of the Schmidt coefficients in Fig. 4.9. The Schmidt coefficients converge in order from larger to smaller as the bond dimension increase. This result suggests that we already captured the essential part of the periodic orbit in the $D \to \infty$ limit.

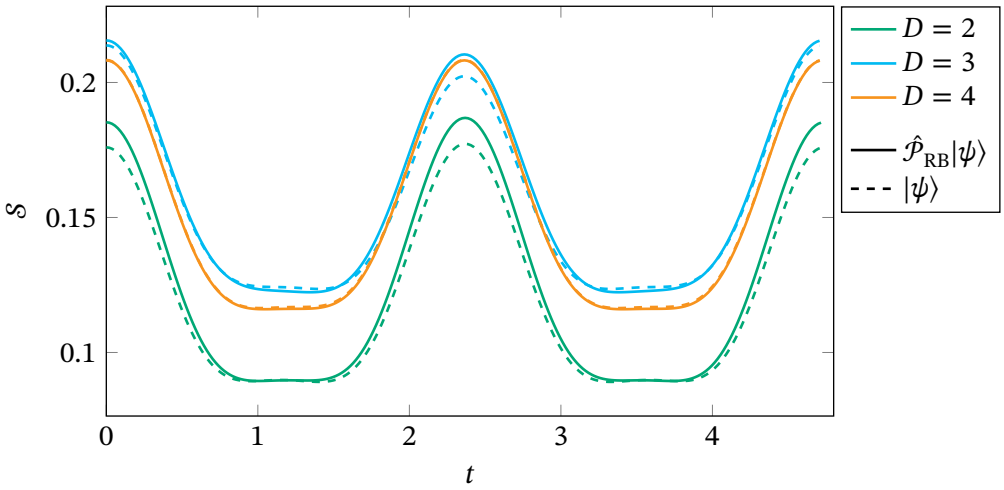

Figure 4.8: Time evolutions of von Neumann bipartite entanglement entropies for periodic orbits we found in $D = 2, 3, 4$. Dashed lines denote leakages of the original states $|\psi(t)\rangle$ and solid lines denote those of the projected states $\hat{\mathcal{P}}_{\mathrm{RB}}|\psi(t)\rangle/\|\hat{\mathcal{P}}_{\mathrm{RB}}|\psi(t)\rangle\|$.

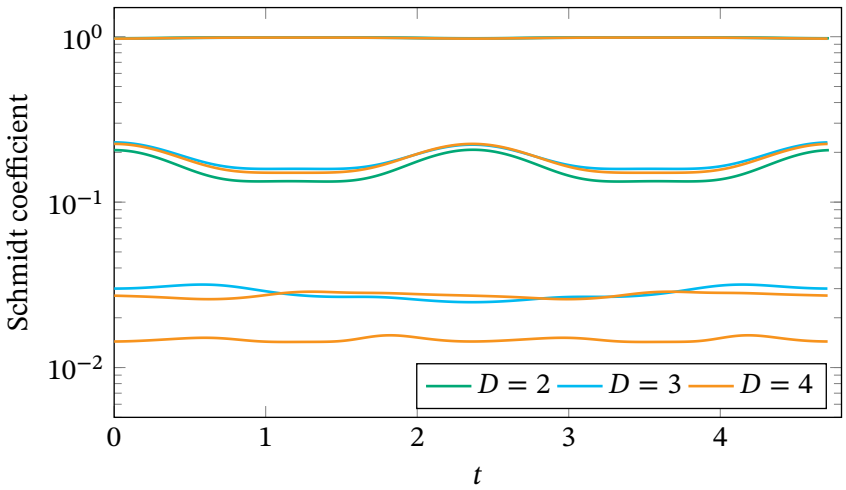

Figure 4.9: Time evolutions of Schmidt coefficients for periodic orbits we found in $D = 2, 3, 4$.

5 | Scarred Eigenstate as a Superposition of Periodic Orbits

In this chapter, we consider the relation between the scarred eigenstates discussed in Chapter 2 and the semiclassical periodic orbits we discovered in Chapter 4. In Section 5.1, we construct an approximate eigenstate by considering a superposition of periodic orbits. We calculate the energy variance of the obtained states to discuss the accuracy of the approximation. In Section 5.2, we calculate the bipartite entanglement entropy of the obtained eigenstates to verify that they are scarred eigenstates. In Section 5.3, we note the finite-energy eigenstates with superposition and its "tower" structure.

5.1 Superposition of periodic orbits

In this section, we consider a superposition of periodic orbits defined as

$$|\Psi\rangle \coloneqq \int_0^T \mathrm{d}t\, |\psi(t)\rangle = \int_0^T \mathrm{d}t \sum_{\{s\}} \mathrm{Tr}\left[\prod_{i=1}^{N} A_{\mathrm{L}}(t)^{s_i}\right] |\{s\}\rangle. \tag{5.1.1}$$

As shown below, $|\Psi\rangle$ and $\hat{\mathcal{P}}_{\mathrm{RB}}|\Psi\rangle$ can be regarded as approximations of the energy eigenstate of $\hat{H}_{\mathrm{PXP}}$. If the TDVP dynamics perfectly coincides with the true quantum dynamics, i.e., $-\mathrm{i}\hat{H}_{\mathrm{PXP}}|\psi(t)\rangle = (\mathrm{d}/\mathrm{d}t)|\psi(t)\rangle$ holds, $|\Psi\rangle$ should be the zero-energy eigenstate of $\hat{H}_{\mathrm{PXP}}$ because

$$\hat{H}_{\mathrm{PXP}}|\Psi\rangle = \mathrm{i}\int_0^T \mathrm{d}t\, (-\mathrm{i}\hat{H}_{\mathrm{PXP}})|\psi(t)\rangle = \mathrm{i}\int_0^T \mathrm{d}t\, \frac{\mathrm{d}}{\mathrm{d}t}|\psi(t)\rangle = \mathrm{i}|\psi(T)\rangle - \mathrm{i}|\psi(0)\rangle = 0. \tag{5.1.2}$$

We note that $|\psi(0)\rangle$ and $|\psi(T)\rangle$ are equal including global phase factor since $\langle\psi(t)|\hat{H}_{\mathrm{PXP}}|\psi(t)\rangle = 0$ holds for our case. The other state $\hat{\mathcal{P}}_{\mathrm{RB}}|\Psi\rangle$ is also the zero-energy eigenstate since $[\hat{\mathcal{P}}_{\mathrm{RB}}, \hat{H}_{\mathrm{PXP}}] = 0$ holds.

However, for the case of finite bond dimension, a finite error exists between the TDVP dynamics and the true quantum dynamics. We already define the error vector $|\gamma(t)\rangle$ as

$$|\gamma(t)\rangle \coloneqq \frac{\mathrm{d}}{\mathrm{d}t}|\psi(t)\rangle + \mathrm{i}\hat{H}_{\mathrm{PXP}}|\psi(t)\rangle. \tag{5.1.3}$$

In this case, $|\Psi\rangle$ is no-longer an exact eigenstate, but an approximation of it. The accuracy of this approximation can be estimated by the energy variance

$$\frac{\langle\Psi|\hat{H}_{\mathrm{PXP}}^2|\Psi\rangle}{\langle\Psi|\Psi\rangle} = \frac{\langle\Psi|(\mathrm{i}\hat{H}_{\mathrm{PXP}})(-\mathrm{i}\hat{H}_{\mathrm{PXP}})|\Psi\rangle}{\langle\Psi|\Psi\rangle} = \frac{1}{\langle\Psi|\Psi\rangle}\iint_0^T \mathrm{d}t\mathrm{d}u\, \langle\gamma(t)|\gamma(u)\rangle \tag{5.1.4}$$

$$\frac{(\langle\Psi|\hat{\mathcal{P}}_{\mathrm{RB}})\hat{H}_{\mathrm{PXP}}^2(\hat{\mathcal{P}}_{\mathrm{RB}}|\Psi\rangle)}{(\langle\Psi|\hat{\mathcal{P}}_{\mathrm{RB}})(\hat{\mathcal{P}}_{\mathrm{RB}}|\Psi\rangle)} = \frac{\langle\Psi|(\mathrm{i}\hat{H}_{\mathrm{PXP}})\hat{\mathcal{P}}_{\mathrm{RB}}(-\mathrm{i}\hat{H}_{\mathrm{PXP}})|\Psi\rangle}{\langle\Psi|\hat{\mathcal{P}}_{\mathrm{RB}}|\Psi\rangle} = \frac{1}{\langle\Psi|\hat{\mathcal{P}}_{\mathrm{RB}}|\Psi\rangle}\iint_0^T \mathrm{d}t\mathrm{d}u\, \langle\gamma(t)|\hat{\mathcal{P}}_{\mathrm{RB}}|\gamma(u)\rangle. \tag{5.1.5}$$

In the rest of this section, we derive the asymptotic form of these variances in the thermodynamic limit.

As discussed in Section 3.3.4, since $\hat{H}_{\mathrm{PXP}}$ is the sum of nearest-neighbor interactions, $|\gamma(t)\rangle$ in the thermodynamic limit can be represented as

$$|\gamma(t)\rangle = \sum_{j=0}^{N-1} \hat{T}^j \sum_{\{s\}} \mathrm{Tr}\left[B(t)^{s_1,s_2} C(t)^{-1} \left[\prod_{i=3}^{N} A_{\mathrm{L}}(t)^{s_i} \right] \right] |\{s\}\rangle, \tag{5.1.6}$$

where $\hat{T}$ denotes one unit-cell translation operator and B is defined in Eq. (3.3.23). Here, $(1_{D\times D}|\mathcal{T}^{B}_{A_{\mathrm{L}}A} = 0$ satisfies for any tensor A and $\langle\gamma(t)|\gamma(t)\rangle = N(1_{D\times D}|\mathcal{T}^{B}_{B}|1_{D\times D})$ holds in the thermodynamic limit.

To discuss the denominator of the Eq. (5.1.4), we consider $\lambda_{\mathrm{LM}}(A_{\mathrm{L}}(t), A_{\mathrm{L}}(u))$, the eigenvalue of transfer matrix $\mathcal{T}^{A_{\mathrm{L}}(t)}_{A_{\mathrm{L}}(u)}$ with the largest magnitude. It holds that $\lambda_{\mathrm{LM}}(A_{\mathrm{L}}(t), A_{\mathrm{L}}(t)) = 1$ and $\lambda_{\mathrm{LM}}(A_{\mathrm{L}}(t), A_{\mathrm{L}}(u)) \leq 1$ because of the normalization. To consider series expansion

$$\lambda_{\mathrm{LM}}(A_{\mathrm{L}}(t), A_{\mathrm{L}}(t+\epsilon)) = 1 + \lambda^{(1)}(t)\epsilon + \lambda^{(2)}(t)\epsilon^2 + \dots, \tag{5.1.7}$$

we use the perturbation theory of non-Hermitian matrix [177]. We denote the eigenvalues and eigenvectors of a non-Hermitian matrix $X \in \mathbb{C}^{d\times d}$ as

$$X|r_i) = \lambda_i|r_i), \quad (l_i|X = \lambda_i(l_i|, \quad (l_i|r_j) = \delta_{i,j}, \quad |\lambda_1| > |\lambda_2| \geq |\lambda_3| \geq \dots \tag{5.1.8}$$

and define the projector $\mathcal{P}$ and the reduced resolvent $\mathcal{S}$ as

$$\mathcal{P} = |r_1)(l_1|, \quad \mathcal{S} = \sum_{i=2}^{d} \frac{1}{\lambda_1 - \lambda_i} |r_i)(l_i|. \tag{5.1.9}$$

Then, the non-Hermitian perturbation theory says

$$\begin{aligned} &\lambda_1(X + \epsilon X^{(1)} + \epsilon^2 X^{(2)} + \dots) - \lambda_1(X) \\ &= \epsilon\,\mathrm{Tr}[X^{(1)}\mathcal{P}] + \epsilon^2 \left(\mathrm{Tr}[X^{(2)}\mathcal{P}] + \mathrm{Tr}[X^{(1)}\mathcal{S}X^{(1)}\mathcal{P}]\right) + \dots \\ &= \epsilon(l_1|X^{(1)}|r_1) + \epsilon^2 \left((l_1|X^{(2)}|r_1) + (l_1|X^{(1)}\mathcal{S}X^{(1)}|r_1)\right) + \dots. \end{aligned} \tag{5.1.10}$$

By substituting $X = \mathcal{T}_{A_{\mathrm{L}}}^{A_{\mathrm{L}}}, X^{(1)} = \mathcal{T}_{A_{\mathrm{L}}}^{\dot{A}_{\mathrm{L}}}, X^{(2)} = \mathcal{T}_{A_{\mathrm{L}}}^{\ddot{A}_{\mathrm{L}}/2}$ and using $(l_1|\mathcal{T}_{A_{\mathrm{L}}}^{\dot{A}_{\mathrm{L}}} = 0$, we derive $\lambda^{(1)} = 0$ and $\lambda^{(2)} = (l_1|\mathcal{T}_{A_{\mathrm{L}}}^{\ddot{A}_{\mathrm{L}}}|r_1)/2$. We remove $\ddot{A}_{\mathrm{L}}$ by considering the time derivative of $(l_1|\mathcal{T}_{A_{\mathrm{L}}}^{\dot{A}_{\mathrm{L}}}|r_1)$

$$\frac{\mathrm{d}}{\mathrm{d}t}(l_1|\mathcal{T}_{A_{\mathrm{L}}}^{\dot{A}_{\mathrm{L}}}|r_1) = (l_1|\mathcal{T}_{A_{\mathrm{L}}}^{\ddot{A}_{\mathrm{L}}}|r_1) + (l_1|\mathcal{T}_{\dot{A}_{\mathrm{L}}}^{\dot{A}_{\mathrm{L}}}|r_1) + (\dot{l}_1|\mathcal{T}_{A_{\mathrm{L}}}^{\dot{A}_{\mathrm{L}}}|r_1) + (l_1|\mathcal{T}_{A_{\mathrm{L}}}^{\dot{A}_{\mathrm{L}}}|\dot{r}_1) = 0 \tag{5.1.11}$$

and substituting $(l_1| = (1_{D\times D}|$, $(\dot{l}_1| = 0$, and $|r_1) = |CC^\dagger)$ as

$$(l_1|\mathcal{T}_{A_{\mathrm{L}}}^{\ddot{A}_{\mathrm{L}}}|r_1) = -(l_1|\mathcal{T}_{\dot{A}_{\mathrm{L}}}^{\dot{A}_{\mathrm{L}}}|r_1) = -(1|\mathcal{T}_{\dot{A}_{\mathrm{L}}C}^{\dot{A}_{\mathrm{L}}C}|1). \tag{5.1.12}$$

By defining

$$a(t) \coloneqq -\lambda^{(2)}(t) = (1_{D\times D}|\mathcal{T}_{\dot{A}_{\mathrm{L}}C}^{\dot{A}_{\mathrm{L}}C}|1_{D\times D})/2, \tag{5.1.13}$$

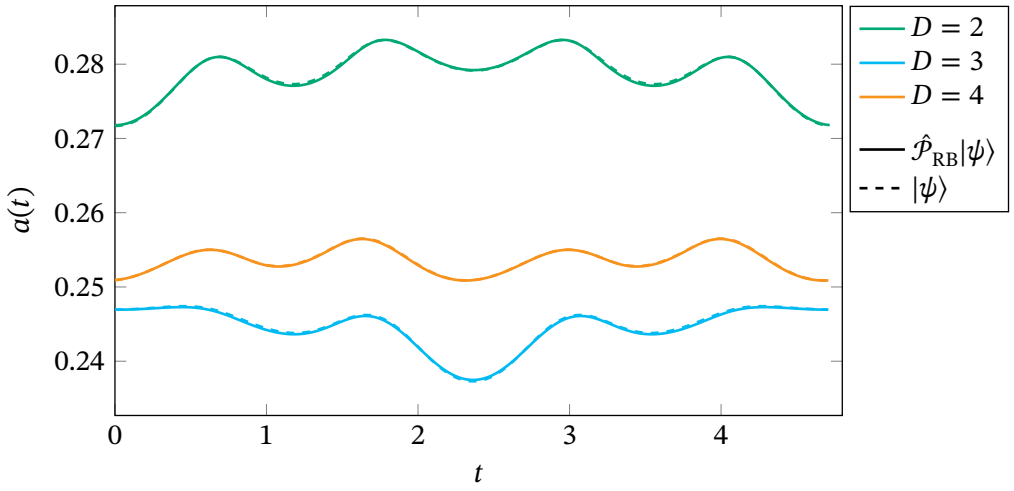

Figure 5.1: Time evolutions of $a(t)$ defined in Eq. (5.1.13).

the denominator of the variance defined in the Eq. (5.1.4) can be calculated as

$$\begin{aligned}
\langle\Psi|\Psi\rangle &= \iint_0^T \mathrm{d}t\mathrm{d}u\, \mathrm{Tr}\left[\left(\mathcal{T}_{A_{\mathrm{L}}(u)}^{A_{\mathrm{L}}(t)}\right)^N\right] \\
&\sim \iint_0^T \mathrm{d}t\mathrm{d}u\, \lambda_{\mathrm{LM}}(A_{\mathrm{L}}(t), A_{\mathrm{L}}(u))^N \\
&\sim \int_0^T \mathrm{d}t \int \mathrm{d}\delta t \exp\left(N\log(1-a(t)\delta t^2)\right) \\
&\sim \int_0^T \mathrm{d}t \int \mathrm{d}\delta t \exp\left(-Na(t)\delta t^2\right) \\
&= \int_0^T \mathrm{d}t \sqrt{\frac{\pi}{Na(t)}} = \sqrt{\frac{\pi}{N}} \int_0^T \mathrm{d}t\, a(t)^{-1/2}.
\end{aligned} \tag{5.1.14}$$

Because λ^N has a finite value only around $t \approx u$, we can estimate the numerator of the variance as

$$\begin{aligned}
\langle\Psi|\hat{H}_{\mathrm{PXP}}^2|\Psi\rangle &\sim \int_0^T \mathrm{d}t\, \langle\gamma(t)|\gamma(t)\rangle \int \mathrm{d}\delta t \exp\left(-Na(t)\delta t^2\right) \\
&= \sqrt{\frac{\pi}{N}} \int_0^T \mathrm{d}t\, \langle\gamma(t)|\gamma(t)\rangle a(t)^{-1/2} \\
&= N\sqrt{\frac{\pi}{N}} \int_0^T \mathrm{d}t\, (1_{D\times D}|\mathcal{T}_{B(t)}^{B(t)}|1_{D\times D}) a(t)^{-1/2}.
\end{aligned} \tag{5.1.15}$$

By combining these results, we can estimate the energy variance of the state $|\Psi\rangle$ per unit cell in the thermodynamic limit.

To calculate the norm and energy variance of $\hat{\mathcal{P}}_{\mathrm{RB}}|\Psi\rangle$, we have to use a little trick. Let us remember that the projection operator $\hat{\mathcal{P}}_{\mathrm{RB}}$ can be represented in terms of the matrix product operator (MPO) as

$$\hat{\mathcal{P}}_{\mathrm{RB}} = \sum_{\{s\},\{t\}} \mathrm{Tr}\left[\prod_i (W_{\hat{\mathcal{P}}_{\mathrm{RB}}})^{s_i,t_i}\right] |\{s\}\rangle\langle\{t\}| := \mathrm{Tr}\left[\prod_i \begin{pmatrix} 1 - |\circ\bullet\rangle\langle\circ\bullet|_i & |\circ\bullet\rangle\langle\circ\bullet|_i \\ |\circ\circ\rangle\langle\circ\circ|_i & |\circ\bullet\rangle\langle\circ\bullet|_i \end{pmatrix}\right]. \tag{5.1.16}$$

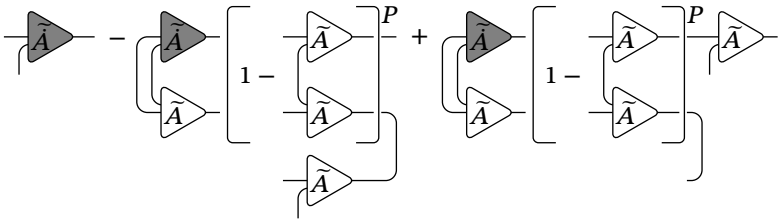

Figure 5.2: Diagram representation of tangent-vector transformation to make the left canonical form.

The MPS representation of the projected state $\hat{\mathcal{P}}_{\mathrm{RB}}|\psi\rangle/\|\hat{\mathcal{P}}_{\mathrm{RB}}|\psi\rangle\|$ is given by a tensor $\widetilde{A}(t)$ defined as

$$A_{\mathrm{L}}(t)[W]^{s}_{(l,l'),(r,r')} \coloneqq \sum_{t} W^{s,t}_{l',r'} A_{\mathrm{L}}(t)^{t}_{l,r} \tag{5.1.17}$$

$$\widetilde{A}(t) \coloneqq \frac{A_{\mathrm{L}}(t)[W_{\hat{\mathcal{P}}_{\mathrm{RB}}}]}{\sqrt{\lambda_{\mathrm{LM}}(A_{\mathrm{L}}(t)[W_{\hat{\mathcal{P}}_{\mathrm{RB}}}])}} = \frac{A_{\mathrm{L}}(t)[W_{\hat{\mathcal{P}}_{\mathrm{RB}}}]}{\sqrt{\lambda_{\mathrm{LM}}(A_{\mathrm{L}}(0)[W_{\hat{\mathcal{P}}_{\mathrm{RB}}}])}}. \tag{5.1.18}$$

Here, $\lambda_{\mathrm{LM}}(A_{\mathrm{L}}(t)[W_{\hat{\mathcal{P}}_{\mathrm{RB}}}])$ is time independent since $\langle\hat{\mathcal{P}}_{\mathrm{RB}}\rangle$ conserves in our algorithm. We make $\widetilde{A}$ left canonical as $\widetilde{A}_{\mathrm{L}} = \sqrt{\tilde{l}}\widetilde{A}\sqrt{\tilde{l}}^{-1}$, where $\tilde{l}$ denotes a dominant left eigenvector of $\mathcal{T}^{\widetilde{A}}_{\widetilde{A}}$. We can obtain the time derivative of $\widetilde{A}_{\mathrm{L}}$ as

$$\dot{\widetilde{A}}_{\mathrm{L}}(t)^{s} = \frac{\sqrt{\tilde{l}}(\dot{A}_{\mathrm{L}}(t)[W_{\hat{\mathcal{P}}_{\mathrm{RB}}}]^{s})\sqrt{\tilde{l}}^{-1}}{\sqrt{\lambda_{\mathrm{LM}}(A_{\mathrm{L}}(0)[W_{\hat{\mathcal{P}}_{\mathrm{RB}}}])}}. \tag{5.1.19}$$

However, this tensor $\dot{\widetilde{A}}_{\mathrm{L}}$ does not satisfy the canonical condition $(1_{D\times D}|\mathcal{T}^{\widetilde{A}_{\mathrm{L}}}_{\widetilde{A}_{\mathrm{L}}} = 0$. Since $\dot{\widetilde{A}}_{\mathrm{L}} + X\widetilde{A}_{\mathrm{L}} - \widetilde{A}_{\mathrm{L}}X$ for any matrix X gives the same tangent vector, we can transform $\dot{\widetilde{A}}_{\mathrm{L}}$ to satisfy the canonical condition. This transformation can be depicted as Fig. 5.2.

We can apply a similar transformation for $\widetilde{B}$, defined as

$$B(t)[W]^{s,t}_{(l,l'),(r,r')} \coloneqq \sum_{u,w,c,c'} W^{s,u}_{l',c'} W^{t,w}_{c',r'} B(t)^{u,w}_{l,c} (C(t)^{-1})_{c,r} \tag{5.1.20}$$

$$\widetilde{B}(t)^{s,t} \coloneqq \frac{\sqrt{\tilde{l}}(B(t)[W_{\hat{\mathcal{P}}_{\mathrm{RB}}}]^{s,t})\sqrt{\tilde{r}}}{\lambda_{\mathrm{LM}}(A_{\mathrm{L}}(0)[W_{\hat{\mathcal{P}}_{\mathrm{RB}}}])}, \tag{5.1.21}$$

to make it satisfy $(1_{D\times D}|\mathcal{T}^{\widetilde{B}}_{\widetilde{A}_{\mathrm{L}}X} = 0$ for any tensor X. Here we use the two-site gauge invariance: $\widetilde{B}^{st}$ and $\widetilde{B}^{st} + X^{s}\widetilde{A}^{t}_{\mathrm{R}} - \widetilde{A}^{s}_{\mathrm{L}}X^{t}$ gives a same $|\gamma\rangle$ for any tensor X. See the Fig. 5.3 for more details. Thus, we can calculate the energy variance of $\hat{\mathcal{P}}_{\mathrm{RB}}|\Psi\rangle$ as well as $|\Psi\rangle$.

In Table 5.1, we show the integrated values of the periodic orbits that we obtained. We can see the decrease of the energy variance between $D = 2$ and $D = 4$.

As the end of the section, we verify the asymptotic expansions defined in Eqs. (5.1.14) and (5.1.15) by comparing with finite-size results. We already know the MPO representation of $\hat{\mathcal{P}}_{\mathrm{RB}}$. General locally interacting Hamiltonian also has MPO representation [178–184]. In the case of periodic boundary conditions (PBC), MPO of nearest-neighbor interaction $\hat{H}$ =

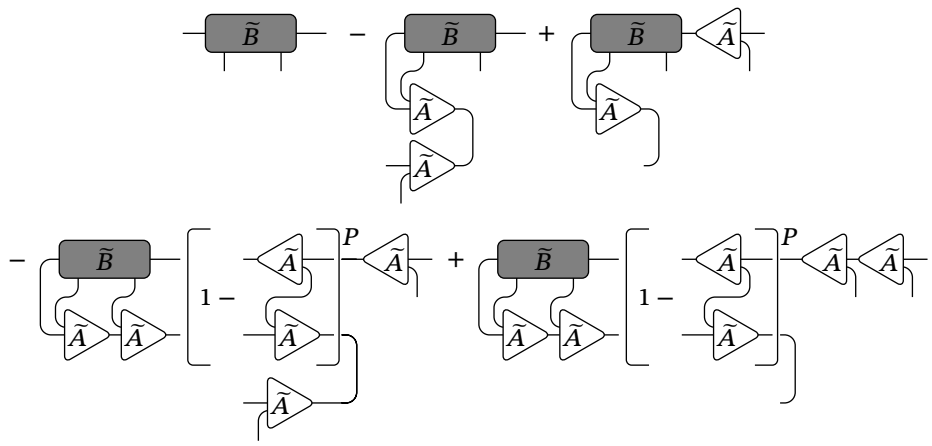

Figure 5.3: Diagram representation of residual-vector transformation to make the left canonical form.

$\frac{1}{N}\frac{\langle\Psi\vert\hat{H}^2_{\mathrm{PXP}}\vert\Psi\rangle}{\langle\Psi\vert\Psi\rangle}$	$D=2$	$D=3$	$D=4$
$\vert\Psi\rangle$	5.55029×10^{-4}	7.07532×10^{-4}	4.23941×10^{-4}
$\hat{\mathcal{P}}_{\mathrm{RB}}\vert\Psi\rangle$	4.59314×10^{-4}	4.76534×10^{-4}	3.43175×10^{-4}

Table 5.1: Energy variances of the superposition.

$\sum_{i=1}^{N}\sum_{k=1}^{K}\hat{X}_i^{(k)}\hat{Y}_{i+1}^{(k)}$ is given by

$$\mathrm{Tr}\left[\prod_{i=1}^{N}W_{\hat{H}}\right] \coloneqq \mathrm{Tr}\left[\left[\prod_{i=1}^{N-1}\begin{pmatrix}\hat{1}_i & & & & \\ \hat{Y}_i^{(1)} & & & & \\ \vdots & & 0 & & \\ \hat{Y}_i^{(K)} & & & & \\ 0 & \hat{X}_i^{(1)} & \dots & \hat{X}_i^{(K)} & \hat{1}_i\end{pmatrix}\right]\begin{pmatrix}0 & \hat{X}_N^{(1)} & \dots & \hat{X}_N^{(K)} & \hat{1}_N \\ & & & & \hat{Y}_i^{(1)} \\ & & 0 & & \vdots \\ & & & & \hat{Y}_i^{(K)} \\ & & & & 0\end{pmatrix}\right]. \tag{5.1.22}$$

Thus, we can calculate $\langle\Psi|\Psi\rangle$, $\langle\Psi|\hat{\mathcal{P}}_{\mathrm{RB}}|\Psi\rangle$, $\langle\Psi|\hat{H}^2_{\mathrm{PXP}}|\Psi\rangle$, and $\langle\Psi|\hat{\mathcal{P}}_{\mathrm{RB}}\hat{H}^2_{\mathrm{PXP}}\hat{\mathcal{P}}_{\mathrm{RB}}|\Psi\rangle$ for finite N by taking integral $\iint \mathrm{d}t\mathrm{d}u$ of $\mathrm{Tr}[(\mathcal{T}_{A_{\mathrm{L}}(u)}^{A_{\mathrm{L}}(t)})^N]$ and $\mathrm{Tr}[(\mathcal{T}_{A_{\mathrm{L}}(u)}^{A_{\mathrm{L}}(t)[W]})^N]$ with $W_{\hat{\mathcal{P}}_{\mathrm{RB}}}$, $W_{\hat{H}^2_{\mathrm{PXP}}}$, and $W_{\hat{\mathcal{P}}_{\mathrm{RB}}\hat{H}^2_{\mathrm{PXP}}\hat{\mathcal{P}}_{\mathrm{RB}}}$ defined as

$$(W_{\hat{H}^2_{\mathrm{PXP}}})^{s,u}_{(l,l'),(r,r')} = (W_{\hat{H}_{\mathrm{PXP}}})^{s,t}_{l,r}(W_{\hat{H}_{\mathrm{PXP}}})^{t,u}_{l',r'} \tag{5.1.23}$$

$$(W_{\hat{\mathcal{P}}_{\mathrm{RB}}\hat{H}^2_{\mathrm{PXP}}\hat{\mathcal{P}}_{\mathrm{RB}}})^{s,w}_{(l,l',l''),(r,r',r'')} = (W_{\hat{\mathcal{P}}_{\mathrm{RB}}})^{s,t}_{l,r}(W_{\hat{H}^2_{\mathrm{PXP}}})^{t,u}_{l',r'}(W_{\hat{\mathcal{P}}_{\mathrm{RB}}})^{u,w}_{l'',r''}. \tag{5.1.24}$$

In Fig. 5.4, we show the norm of $|\Psi\rangle$ in the finite-size system calculated by the first line of Eq. (5.1.14) and compare it to the asymptotic form defined in the last line of Eq. (5.1.14). We also show the difference between the energy variance in finite-size systems defined in the first line of Eq. (5.1.15) and the asymptotic form defined in the last line of Eq. (5.1.15) in Fig. 5.5.

5.2 Bipartite entanglement entropy

Our main claim is that $|\Psi\rangle$ corresponds to the scarred eigenstate. To clarify it, we calculate Rényi bipartite entanglement entropy (EE) of $|\Psi\rangle$ and show the sub-volume law of it. As we

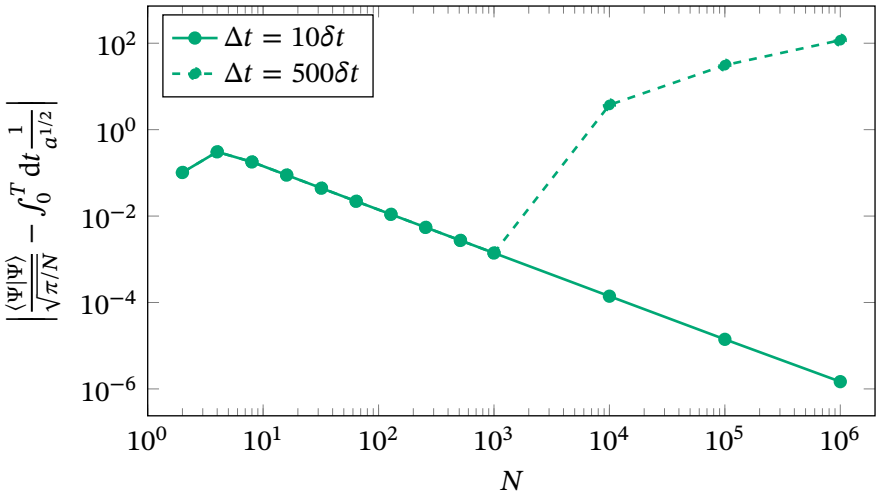

Figure 5.4: Difference between the asymptotic form defined in the last line of Eq. (5.1.14) and the result for the finite-size systems obtained by the first line of Eq. (5.1.14) for the periodic orbit with bond-dimension $D = 2$ without projection $\hat{\mathcal{P}}_{\mathrm{RB}}$. The original trajectory was obtained by TDVP algorithm with 50000 time steps ($\delta t \approx 9.5 \times 10^{-4}$). In numerical calculation of the first line of Eq. (5.1.14), we use rectangular integration with step width $\Delta t = 10 \times \delta t$ (solid line) and $\Delta t = 500 \times \delta t$ (dashed line). The result suggest $\Delta t = 500 \times \delta t$ is small enough to obtain accurate result for $N \lessapprox 10^3$.

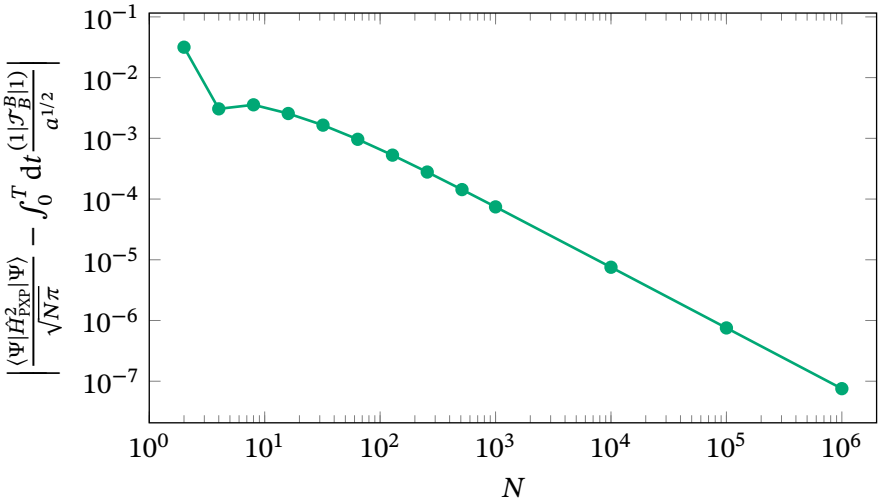

Figure 5.5: Difference between the asymptotic form defined in the last line of Eq. (5.1.15) and the result for the finite-size systems defined in the first line of Eq. (5.1.15) for the periodic orbit with bond dimension $D = 2$ without projection $\hat{\mathcal{P}}_{\mathrm{RB}}$. The original trajectory was obtained by TDVP algorithm with 50000 time steps ($\delta t \approx 9.5 \times 10^{-4}$). In numerical calculation of the first line of Eq. (5.1.15), we use rectangular integration with step width $\Delta t = 10 \times \delta t$.

discussed in Section 2.1.1, eigenstates that satisfy ETH show the volume-law EE, and the sub-volume law means the violation of ETH.

At the beginning, we consider the Rényi-2 EE. We divide the system into two parts as

$$|\Psi\rangle \coloneqq \int_0^T \mathrm{d}t|\psi(t)\rangle = \int_0^T \mathrm{d}t \sum_{\mathbf{i}} |\psi_{\mathrm{L}}(t)_{\mathbf{i}}\rangle \otimes |\psi_{\mathrm{R}}(t)_{\mathbf{i}}\rangle$$
$$= \int_0^T \mathrm{d}t$$

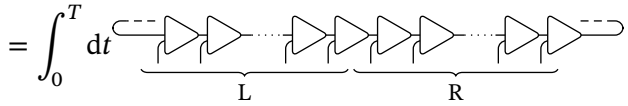

(5.2.1)

where $|\psi_{\mathrm{L}}\rangle$ and $|\psi_{\mathrm{R}}\rangle$ are defined as

$$|\psi_{\mathrm{L}}(t)_{\mathbf{i}}\rangle = |\psi_{\mathrm{L}}(t)_{(i,i')}\rangle \coloneqq \sum_{\{s\}_{\mathrm{L}}} \left[\prod_{i=1}^{\lfloor N/2 \rfloor} A^{s_i}(t)\right]_{i,i'} |\{s\}_{\mathrm{L}}\rangle, \tag{5.2.2}$$

$$|\psi_{\mathrm{R}}(t)_{\mathbf{j}}\rangle = |\psi_{\mathrm{R}}(t)_{(j,j')}\rangle \coloneqq \sum_{\{s\}_{\mathrm{R}}} \left[\prod_{i=\lceil N/2 \rceil}^{N} A^{s_i}(t)\right]_{j',j} |\{s\}_{\mathrm{R}}\rangle. \tag{5.2.3}$$

We define the partial trace of $|\Psi\rangle$ as

$$\hat{\rho}_{\mathrm{L}} \coloneqq \mathrm{Tr}_{\mathrm{R}}[|\Psi\rangle\langle\Psi|] = \iint_0^T \mathrm{d}t\mathrm{d}u$$

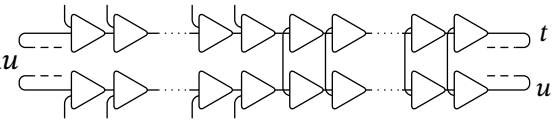

(5.2.4)

The Rényi-2 bipartite EE S_2 is defined in terms of

$$\mathrm{Tr}[\hat{\rho}_{\mathrm{L}}^2] = \iiiint_0^T \mathrm{d}t\mathrm{d}u\mathrm{d}v\mathrm{d}w$$

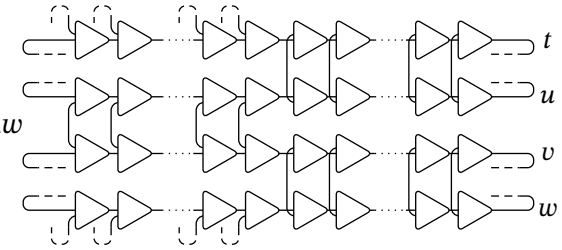

$$= \iiiint_0^T \mathrm{d}t\mathrm{d}u\mathrm{d}v\mathrm{d}w$$

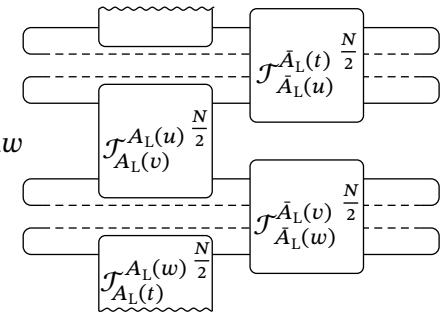

(5.2.5)

as

$$S_2 \coloneqq -\ln \frac{\mathrm{Tr}[\hat{\rho}_{\mathrm{L}}^2]}{\mathrm{Tr}[\hat{\rho}_{\mathrm{L}}]^2}. \tag{5.2.6}$$

We already derived the asymptotic form of $\mathrm{Tr}[\hat{\rho}_{\mathrm{L}}] = \langle\Psi|\Psi\rangle$ in Section 5.1. As well as the energy variance, EE of $|\Psi\rangle$ in the thermodynamic limit can be calculated as a weighted integral of EE of the integrand $|\psi(t)\rangle$. Since it holds that $(\mathcal{T}_{A_{\mathrm{L}}}^{A_{\mathrm{L}}})^{N/2} \to |CC^\dagger)(1_{D\times D}|$, the Rényi-2 EE of $|\psi(t)\rangle$

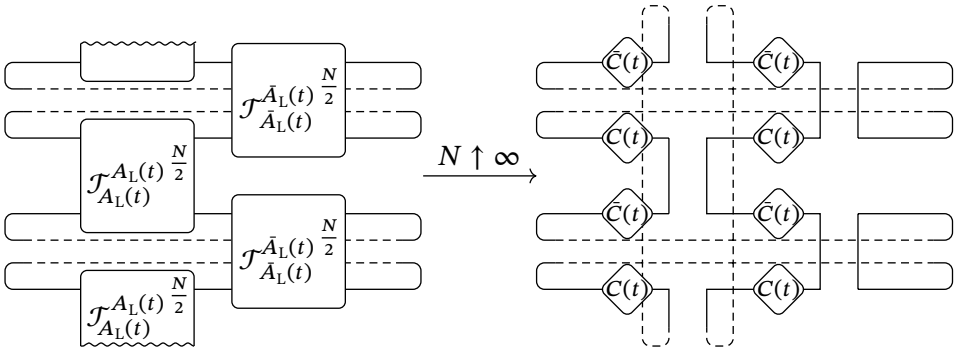

Figure 5.6: Schematic picture of the Rényi-2 entanglement entropy of the left canonical uniform MPS in the thermodynamic limit.

is equal to $\mathrm{Tr}[(C(t)C(t)^\dagger)^2]^2$ as depicted in Fig. 5.6. Then, we can estimate $\mathrm{Tr}[\hat{\rho}_L^2]$ as

$$\begin{aligned}
\mathrm{Tr}[\hat{\rho}_L^2] &\approx \iiiint_0^T \mathrm{d}t\mathrm{d}u\mathrm{d}v\mathrm{d}w\, \mathrm{Tr}[(C(t)C(t)^\dagger)^2]^2\, (\lambda(t,u)\lambda(u,v)\lambda(v,w)\lambda(w,t))^{N/2} \\
&\sim \int_0^T \mathrm{d}t\, \mathrm{Tr}[(C(t)C(t)^\dagger)^2]^2 \iiint \mathrm{d}\delta t\mathrm{d}\delta t'\mathrm{d}\delta t'' \\
&\quad \exp\left(-\frac{Na(t)}{2}(\delta t^2 + (\delta t'' - \delta t)^2 + (\delta t' - \delta t'')^2 + \delta t'^2)\right) \\
&= \int_0^T \mathrm{d}t\, \mathrm{Tr}[(C(t)C(t)^\dagger)^2]^2 \frac{1}{2}\left(\frac{2\pi}{Na(t)}\right)^{3/2} \\
&= \frac{(2\pi)^{3/2}}{2} N^{-3/2} \int_0^T \mathrm{d}t\, \mathrm{Tr}[(C(t)C(t)^\dagger)^2]^2 a(t)^{-3/2},
\end{aligned} \tag{5.2.7}$$

where we introduce $\delta t \coloneqq u - t$, $\delta t' \coloneqq v - t$, and $\delta t'' \coloneqq w - t$ and use $u - v = \delta t - \delta t'$ and $v - w = \delta t' - \delta t''$. Finally, we obtain the asymptotic form of EE as

$$\mathcal{S}_2 = -\ln \frac{\mathrm{Tr}[\hat{\rho}_L^2]}{\mathrm{Tr}[\hat{\rho}_L]^2} = \frac{1}{2}\ln N - \ln \frac{(2\pi)^{1/2} \int_0^T \mathrm{d}t\, \mathrm{Tr}[(CC^\dagger)^2]^2 a^{-3/2}}{\left(\int_0^T \mathrm{d}t a^{-1/2}\right)^2}. \tag{5.2.8}$$

It is straightforward to generalize this derivation for Rényi-α EE

$$\mathcal{S}_\alpha \coloneqq \frac{1}{1-\alpha} \ln \frac{\mathrm{Tr}[\hat{\rho}_L^\alpha]}{\mathrm{Tr}[\hat{\rho}_L]^\alpha} \tag{5.2.9}$$

for integers $\alpha > 2$. As well as Eq. (5.2.7), the numerator is estimated as

$$\begin{aligned}
\mathrm{Tr}[\hat{\rho}_L^\alpha] &\sim \int \mathrm{d}t\, \mathrm{Tr}[(C(t)C(t)^\dagger)^\alpha]^2 \\
&\quad \int \mathrm{d}^{\alpha-1}\vec{\delta t} \exp\left(-\frac{Na(t)}{2}\left(\delta t_1^2 + \left(\sum_{i=1}^{2\alpha-2} (\delta t_{i+1} - \delta t_i)^2\right) + \delta t_{2\alpha-1}^2\right)\right) \\
&= \int \mathrm{d}t\, \mathrm{Tr}[(C(t)C(t)^\dagger)^\alpha]^2 \sqrt{\frac{(2\pi)^{2\alpha-1}}{2\alpha(Na(t))^{2\alpha-1}}} \\
&= \frac{(2\pi)^{\frac{2\alpha-1}{2}}}{\sqrt{2\alpha}} N^{-\frac{2\alpha-1}{2}} \int \mathrm{d}t\, \mathrm{Tr}[(C(t)C(t)^\dagger)^\alpha]^2 a(t)^{-\frac{2\alpha-1}{2}},
\end{aligned} \tag{5.2.10}$$

where we use the matrix form

$$\delta t_1^2 + \left(\sum_{i=1}^{2\alpha-2} (\delta t_{i+1} - \delta t_i)^2 \right) + \delta t_{2\alpha-1}^2 = {}^t\vec{\delta t} \begin{bmatrix} 2 & -1 & & \\ -1 & \ddots & \ddots & \\ & \ddots & 2 \end{bmatrix} \vec{\delta t} \tag{5.2.11}$$

and its determinant

$$\begin{vmatrix} 2 & -1 & & \\ -1 & \ddots & \ddots & \\ & \ddots & 2 \end{vmatrix} = 2\alpha. \tag{5.2.12}$$

Finally, we obtain the asymptotic form

$$\mathrm{Tr}[\hat{\rho}_{\mathrm{L}}]^\alpha \sim \left(\sqrt{\frac{\pi}{N}} \int_0^T \mathrm{d}t a(t)^{-1/2} \right)^\alpha \tag{5.2.13}$$

and

$$\begin{aligned} \mathcal{S}_\alpha &= \frac{1}{1-\alpha} \ln \frac{\frac{(2\pi)^{\frac{2\alpha-1}{2}}}{\sqrt{2\alpha}} N^{-\frac{2\alpha-1}{2}} \int \mathrm{d}t\, \mathrm{Tr}[(C(t)C(t)^\dagger)^\alpha]^2 a(t)^{-\frac{2\alpha-1}{2}}}{\left(\sqrt{\frac{\pi}{N}} \int_0^T \mathrm{d}t a(t)^{-1/2} \right)^\alpha} \\ &= \frac{1}{2} \ln N + \frac{1}{1-\alpha} \ln \frac{\frac{(2\pi)^{\frac{\alpha-1}{2}}}{\sqrt{\alpha/2^{\alpha-1}}} \int_0^T \mathrm{d}t\, \mathrm{Tr}[(C(t)C(t)^\dagger)^\alpha]^2 a(t)^{-\frac{2\alpha-1}{2}}}{\left(\int_0^T \mathrm{d}t a(t)^{-1/2} \right)^\alpha}. \end{aligned} \tag{5.2.14}$$

The first term is the logarithmic term in the system size. This term is independent of the choice of α. It suggests that the von Neumann EE also has the same logarithmic term since the von Neumann entropy can be regarded as the $\alpha \to 1$ limit of the Rényi entropy. In the previous study [132], the logarithmic correction of the von Neumann EE of the scarred eigenstates of the PXP model is estimated as $\mathcal{S} \sim 0.48 \ln N$ by the finite-size scaling. Our result is compatible with it.

The second term is a weighted integral of the Rényi-α EE of each point along the periodic orbit. To show that the EE of $|\Psi\rangle$ satisfies the sub-volume law, it is necessary to check that this term converges to the $\mathcal{O}(1)$ value in the limit $D \to \infty$. In Fig. 5.7, we show the results of this term for various α for the periodic orbits that we obtained. For each α, the result converges already in $D = 4$. The value of this constant term of the von Neumann EE can be discussed by taking extrapolation of $\alpha \to 1$, but it is difficult to determine how to take this limit from Fig. 5.7. This is an important future work.

Finally, we verify that the asymptotic form of the Rényi EE is correct. In Fig. 5.8, we show the comparison of Rényi-2 EE between the last line of Eq. (5.2.7) and the finite-size result. The plot suggests that the difference vanishes in the thermodynamic limit.

5.3 Tower of scarred eigenstates

The other important feature of the scarred eigenstates is the "tower" structure of it. In this section, we depict that this structure can be reproduced by the superposition with a phase factor.

We define $|\Psi_k\rangle$ with $k \in \mathbb{Z}$ as

$$|\Psi_k\rangle := \int_0^T \mathrm{d}t\, e^{\frac{2\pi k \mathrm{i}}{T} t} |\psi(t)\rangle. \tag{5.3.1}$$

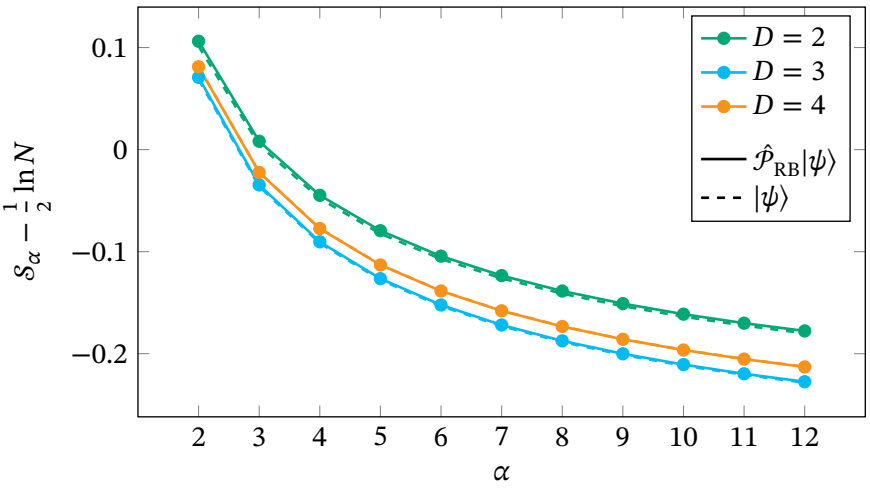

Figure 5.7: Rényi-α entanglement entropies of the superpositions $|\Psi\rangle$ (dashed lines) and $\hat{\mathcal{P}}_{\mathrm{RB}}|\Psi\rangle$ (solid lines).

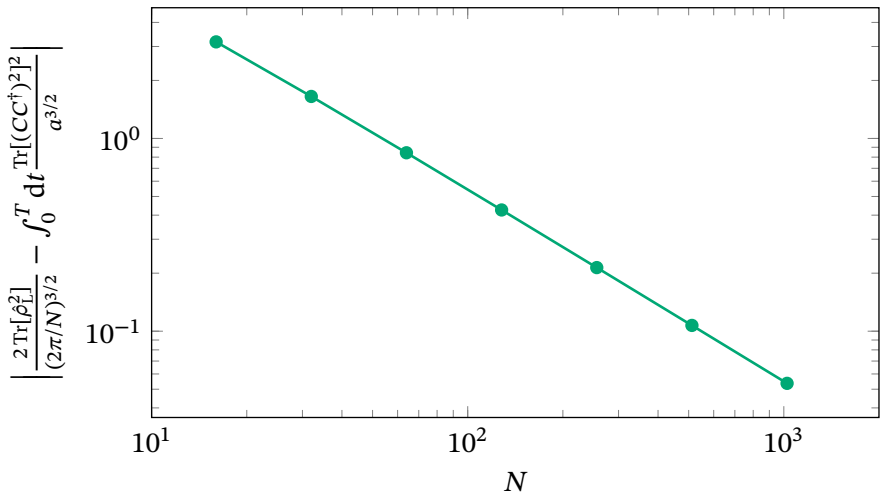

Figure 5.8: Difference between the asymptotic form defined in the last line of Eq. (5.2.7) and the result for the finite-size systems calculated by the last line of Eq. (5.2.5) for the periodic orbit with bond dimension $D = 2$ without projection $\hat{\mathcal{P}}_{\mathrm{RB}}$. The original trajectory was obtained by TDVP algorithm with 50000 time steps ($\delta t \approx 9.5 \times 10^{-4}$). In numerical calculation of the last line of Eq. (5.2.5), we use rectangular integration with step width $\Delta t = 500 \times \delta t$ to reduce the computational cost. Fig. 5.4 suggests this Δt is small enough to obtain good results for $N \lessapprox 10^3$.

If the TDVP dynamics is perfect, $|\Psi_k\rangle$ is an energy eigenstate with energy $2\pi k/T$:

$$\begin{aligned}\hat{H}_{\mathrm{PXP}}|\Psi_k\rangle &= \mathrm{i}\int_0^T \mathrm{d}t\, e^{\frac{2\pi k\mathrm{i}}{T}t}|\dot{\psi}(t)\rangle \\ &= \mathrm{i}(e^{2\pi k\mathrm{i}}|\psi(T)\rangle - |\psi(0)\rangle) - \mathrm{i}\int_0^T \frac{2\pi k\mathrm{i}}{T} e^{\frac{2\pi k\mathrm{i}}{T}t}|\psi(t)\rangle \\ &= \frac{2\pi k}{T}|\Psi_k\rangle.\end{aligned} \tag{5.3.2}$$

Thus, we can construct the scarred eigenstates with finite energy in the same manner of the zero-energy one. The relation between the spacing of the eigenvalues and the period is also compatible with the previous study [132]. It is also possible to obtain the asymptotic forms of them. As long as $k = \mathcal{O}(1)$ holds, the asymptotic forms are equal to those of the zero-energy eigenstate $|\Psi\rangle$.

By using quantum mechanics, when the energy eigenstates with equal energy intervals exist, we can construct the initial state corresponding to the periodic dynamics by taking a superposition of them [35, 133]. Therefore, the results in this chapter can be regarded as the reproduction of the quantum result by the semiclassical analysis with TDVP. Thus, it suggests the adequacy of the aim of our research to investigate the quantum-classical correspondence of QMBS through the analysis of the bond-dimension dependence, which we depicted in Table 2.2.

6 | Conclusion

In the present thesis, we developed a generic method of investigating periodic orbits in the semiclassical dynamics obtained by the time-dependent variational principle (TDVP) for the matrix product state (MPS). We applied this method to the PXP model, a typical model of the quantum many-body scar (QMBS), and found periodic orbits in general bond dimensions. Furthermore, we showed that the characteristic structure of eigenstates in QMBS can be reproduced by a combination of the classical picture based on TDVP and the analysis of the bond-dimensional dependence.

In Chapter 2, we reviewed the basics of the theory of thermalization in isolated quantum many-body systems and introduced the important concept of the eigenstate thermalization hypothesis (ETH). We introduced the QMBS, a new mechanism of ETH and ergodicity breaking, and emphasized the importance of the quantum-classical correspondence. In Chapter 3, we reviewed the TDVP algorithm and its application to the MPS. We introduced the method of enforcing conservation laws in the TDVP algorithm and its importance for QMBS problems. We also reviewed the previous studies investigating the quantum many-body thermalization problems with TDVP for MPS. We indicated the importance of the extrapolation of bond dimensions.

In Chapter 4, we proposed a numerical method to obtain periodic orbit in a semiclassical manifold defined by the uniform MPS. The basic idea is simple, solving the optimization problem to find the perfect recurrence, but there are many obstacles to carrying it out in practice. In Section 4.2.2, we construct a zero energy subspace parameterized by real-valued MPS. In Sections 4.2.4 and 4.2.5, we introduced two important concepts of the numerical calculation: continuous optimization on a Riemannian manifold and automatic differentiation. The research of these concepts has been evolved significantly in recent years, inspired by machine learning and artificial intelligence development. Importing these outstanding achievements is an essential theme of computational physics. In Section 4.3, we revealed the usefulness of the developed method by finding periodic orbits of the PXP model.

In Chapter 5, we approximately reproduced the characteristic structure of the scarred eigenstate of the PXP model from the periodic orbits that we obtained. This reproduction becomes more accurate as the bond dimension increases. Therefore, in the limit of the infinite bond dimension, it should come down to the purely quantum picture based on the eigenstates. Thus, in understanding QMBS in a semiclassical picture, we can regard the bond dimension as a parameter that determines the strength of the quantum nature, like the Planck constant in the discussion of the single-particle quantum scar.

An important prospect of the present study is to obtain a quantitative understanding of the analogy between the bond dimension in QMBS and the Planck constant in the single-particle quantum scar. It would enable us to apply extensive knowledge on single-particle quantum chaos to the study of thermalization and QMBS. For this purpose, we have to find periodic orbits with bond dimensions larger than four and perform a quantitative analysis of the bond-dimensional dependence. It will require further improvements to the algorithm.

As shown in the main text, the proper operation of our optimization depends heavily on the choice of the initial state. As long as we use the gradient method, the risk of being trapped

in a locally optimal solution remains large. We can consider using other algorithms to avoid this problem, such as simulated annealing, optimization based on Bayesian estimation, and neural network-based algorithms.

To handle larger bond dimensions, it would be necessary to estimate the accuracy of the numerical integration. In this thesis, we estimated it by varying the width of the time step and checking the convergence of the results. However, as the bond dimension increases, the errors caused by matrix operations may become non-negligible. It would be crucial to estimate the source and magnitude of the error by comparing the results with validated numerics or multiple-precision arithmetic.

Our analysis focused only on the periodic orbits and did not deal with what was happening outside of them. However, to discuss the stability against perturbations, it is essential to know the properties of the semiclassical dynamical system outside of the periodic orbit. It would be necessary to develop a framework to discuss it. We also did not discuss the uniqueness of the periodic orbit. Understanding their statistical properties would also be essential if there are multiple periodic orbits.

It is important to note that our method is adaptable to general many-body Hamiltonians, including non-integrable and integrable systems. Despite that the importance of the quantum-classical correspondence in QMBS has been widely pointed out, concrete semiclassical dynamical systems have been constructed only for the PXP model and its variants. It contrasts with the fact that many methods have been developed to construct new kinds of QMBS. We hope to deeply understand QMBS and the thermal equilibration problem of non-integrable systems by applying our method to more general models. The versatility of our method also allows us to analyze experimental Hamiltonians that are not idealized for theoretical analysis.

A | Reverse-Mode Differential Rules for Tensor Network Algorithm

In this appendix, we introduce the forms of vector-Jacobian products of tensor operations that are needed to make the TDVP algorithm differentiable.

A.1 Matrix decomposition

Differential rules for QR decomposition, symmetric eigenvalue decomposition, and SVD have been discussed in Ref. [126]. These rules have already been implemented for major AD libraries [170, 171, 173, 185]. However, sometimes, the implementation for complex-valued matrices is lacking. The detailed derivation of the complex SVD can be found in Ref. [186].

Many AD libraries have functions to add user-defined differentiation rules and test the rules by comparing with the results of the numerical differential method. However, we have to test the rule of complex SVD carefully. Let us assume the SVD of a complex square matrix M is given as $M = U\Sigma V^\dagger$, where U and V are unitary matrices and Σ is a real-valued diagonal matrix. Since Σ is diagonal,

$$U\Sigma V^\dagger = (U\,\mathrm{diag}(e^{\mathrm{i}\phi_1}, e^{\mathrm{i}\phi_2}, \dots))\Sigma(V\,\mathrm{diag}(e^{\mathrm{i}\phi_1}, e^{\mathrm{i}\phi_2}, \dots))^\dagger \tag{A.1.1}$$

holds for any set of real numbers $\{\phi_i\}$. Since the right-hand side also fulfills the definition of SVD, this equation means that the complex SVD has a continuous degree of freedom of phases. Thus, to test the differentiation rule of the complex SVD, we have to define some real-valued function that is invariant with respect to the phase factor and compare the results of its derivative between AD and numerical differentiation.

A.2 Einstein summation

Any tensor contraction written by the Einstein summation can be written as a combination of tensor reshaping and matrix-matrix multiplication. Thus, we can use the reverse-mode differential rule of matrix-matrix multiplication

$$C = \mathrm{matmul}(A, B) \coloneqq AB \quad \Rightarrow \quad \mathrm{matmul}_{\mathrm{vjp}}[(A, B)](\bar{C}) = (\bar{C}B^\dagger, A^\dagger\bar{C}). \tag{A.2.1}$$

However, it is more efficient to use the differentiation rule of the Einstein summation itself. We consider the function defined by the Einstein summation

$$B_{\mathbb{b}} = b(A_1, A_2, A_3, \dots)_{\mathbb{b}} = \sum_{(\bigcup_i \mathbb{a}_i)\setminus\mathbb{b}} \prod_i (A_i)_{\mathbb{a}_i}, \tag{A.2.2}$$

where $\mathbb{a}$ and $\mathbb{b}$ denote the symbols of the tensor indices. For example, by taking $\mathbb{a}_1 = (i, j)$, $\mathbb{a}_2 = (j, k)$, and $\mathbb{b} = (i, k)$, b denotes the matrix-matrix multiplication as

$$b(A_1, A_2)_{i,k} = \sum_j (A_1)_{i,j}(A_2)_{j,k}. \tag{A.2.3}$$

Under this notation, the vector-Jacobian product of this function can be written as

$$b_{\mathrm{vjp}}[(A_1, A_2, A_3, \dots)](\bar{B}) = \left(\sum_{(\bigcup_i \mathbb{a}_i)\cup\mathbb{b}\setminus\mathbb{a}_1} \bar{B}_{\mathbb{b}} \prod_{i\neq 1} (A_i^*)_{\mathbb{a}_i}, \sum_{(\bigcup_i \mathbb{a}_i)\cup\mathbb{b}\setminus\mathbb{a}_2} \bar{B}_{\mathbb{b}} \prod_{i\neq 2} (A_i^*)_{\mathbb{a}_i}, \dots \right). \tag{A.2.4}$$

By using this form, we can optimize the contraction order for the reverse mode calculation with some optimization algorithm [187].

A.3 Dominant eigenvalue problem of transfer matrices

The differential rule of general dominant eigenvalue problem of non-Hermitian matrices has been introduced in Ref. [123]. If the matrix is given as a transfer matrix defined in Eq. (3.2.4), we can calculate the differentiation without explicitly constructing the transfer matrix. This formula helps in combining with the matrix-free solver such as Arpack [188].

First, we consider the dominant eigenvectors l and r and eigenvalue λ:

$$f(A, B) = (\lambda, l, r) \quad \Rightarrow \quad (l|\mathcal{T}_B^A = \lambda(l|, \quad \mathcal{T}_B^A|r) = \lambda|r), \quad (l|r) = u. \tag{A.3.1}$$

Here, we assume the eigenvalue λ is non-degenerate. Then, the differential rule can be written as

$$f_{\mathrm{vjp}}[(A, B)](\bar{\lambda}, \bar{l}, \bar{r}) = \left(\frac{\bar{\lambda}}{u^*}, \quad \bar{\lambda} l^\dagger B r^\dagger - l^\dagger B \xi_l - \xi_r B r^\dagger, \quad \bar{\lambda}^* l A r - l A \xi_l^\dagger - \xi_r^\dagger A r \right), \tag{A.3.2}$$

where $(lAr)^s_{l,r}$ denotes $= \sum_{x,y} l_{i,x} A^s_{x,y} r_{y,j}$ and ξs are defined as the result of the following:

$$\left[\mathcal{T}_B^A - \lambda + |r)(l|\right]\left[|\xi_l^\dagger) + |r)(l|\bar{l}^\dagger)\right] = |\bar{l}^\dagger), \tag{A.3.3}$$

$$\left[(\xi_r^\dagger| + (\bar{r}^\dagger|r)(l|\right]\left[\mathcal{T}_B^A - \lambda + |r)(l|\right] = (\bar{r}^\dagger|. \tag{A.3.4}$$

These calculations are similar to those of the infinite boundary conditions defined in Eq. (3.3.14). Note that we have to consider some gauge-invariant functions to test the implementation and the complex SVD.

A.4 Orthogonal basis of null space

An orthogonal basis of the null space of a full rank matrix $A \in \mathbb{F}^{m\times n}$ $(m < n)$ is denoted by $N \in \mathbb{F}^{n\times(n-m)}$ satisfying $AN = 0$ and $N^\dagger N = 1_{(n-m)\times(n-m)}$, where $\mathbb{F}$ denotes $\mathbb{R}$ or $\mathbb{C}$. N is calculated by the full SVD, decompose A into $U\Sigma V^\dagger$, where $U \in \mathrm{U}(m)$, $\Sigma = [\mathrm{diag}(\sigma_1, \dots, \sigma_m)|0_{m\times(n-m)}] \in \mathbb{R}^{m\times n}$, and $V \in \mathrm{U}(n)$. We can consider V is joined by two semi-unitary matrices $V_1 \in \mathbb{F}^{n\times m}$ and $V_2 \in \mathbb{F}^{n\times(n-m)}$ as $V = [V_1|V_2]$. Then, V_2 is nothing but N.

We can find the definition of the reverse-mode differential rule of full SVD in Ref. [189]. We can check that no new terms originate from the complex differential. The differentiation rule of the null space is obtained as

$$\mathrm{nullspace}_{\mathrm{vjp}}[A](\bar{N}) = -U\,\mathrm{diag}(1/\sigma_1, \dots, 1/\sigma_m) V_1^\dagger \bar{N} N^\dagger. \tag{A.4.1}$$

Note that we have to use a function invariant under the transformation $N \to Nu$ where $u \in \mathrm{U}(n-m)$ to test this rule.

Bibliography

[1] M. Rigol, V. Dunjko, and M. Olshanii, "Thermalization and its mechanism for generic isolated quantum systems", Nature **452**, 854 (2008).

[2] C. Gogolin and J. Eisert, "Equilibration, thermalisation, and the emergence of statistical mechanics in closed quantum systems", Rep. Prog. Phys. **79**, 056001 (2016).

[3] L. D'Alessio, Y. Kafri, A. Polkovnikov, and M. Rigol, "From quantum chaos and eigenstate thermalization to statistical mechanics and thermodynamics", Adv. Phys. **65**, 239 (2016).

[4] T. Mori, T. N. Ikeda, E. Kaminishi, and M. Ueda, "Thermalization and prethermalization in isolated quantum systems: a theoretical overview", J. Phys. B **51**, 112001 (2018).

[5] D. A. Abanin, E. Altman, I. Bloch, and M. Serbyn, "Colloquium: Many-body localization, thermalization, and entanglement", Rev. Mod. Phys. **91**, 021001 (2019).

[6] S. Trotzky, Y.-A. Chen, A. Flesch, I. P. McCulloch, U. Schollwöck, J. Eisert, and I. Bloch, "Probing the relaxation towards equilibrium in an isolated strongly correlated one-dimensional Bose gas", Nat. Phys. **8**, 325 (2012).

[7] A. M. Kaufman, M. E. Tai, A. Lukin, M. Rispoli, R. Schittko, P. M. Preiss, and M. Greiner, "Quantum thermalization through entanglement in an isolated many-body system", Science **353**, 794 (2016).

[8] G. Clos, D. Porras, U. Warring, and T. Schaetz, "Time-Resolved Observation of Thermalization in an Isolated Quantum System", Phys. Rev. Lett. **117**, 170401 (2016).

[9] C. Neill, P. Roushan, M. Fang, Y. Chen, M. Kolodrubetz, Z. Chen, A. Megrant, R. Barends, B. Campbell, B. Chiaro, A. Dunsworth, E. Jeffrey, J. Kelly, J. Mutus, P. J. J. O'Malley, C. Quintana, D. Sank, A. Vainsencher, J. Wenner, T. C. White, A. Polkovnikov, and J. M. Martinis, "Ergodic dynamics and thermalization in an isolated quantum system", Nat. Phys. **12**, 1037 (2016).

[10] J. v. Neumann, "Beweis des Ergodensatzes und desH-Theorems in der neuen Mechanik", Zeitschrift für Physik **57**, 30 (1929).

[11] J. M. Deutsch, "Quantum statistical mechanics in a closed system", Phys. Rev. A **43**, 2046 (1991).

[12] M. Srednicki, "Chaos and quantum thermalization", Phys. Rev. E **50**, 888 (1994).

[13] H. Tasaki, "From Quantum Dynamics to the Canonical Distribution: General Picture and a Rigorous Example", Phys. Rev. Lett. **80**, 1373 (1998).

[14] H. Tasaki, "Typicality of Thermal Equilibrium and Thermalization in Isolated Macroscopic Quantum Systems", J. Stat. Phys. **163**, 937 (2016).

[15] H. Kim, T. N. Ikeda, and D. A. Huse, "Testing whether all eigenstates obey the eigenstate thermalization hypothesis", Phys. Rev. E **90**, 052105 (2014).

[16] W. Beugeling, R. Moessner, and M. Haque, "Finite-size scaling of eigenstate thermalization", Phys. Rev. E **89**, 042112 (2014).

[17] M. Rigol, "Breakdown of thermalization in finite one-dimensional systems", Phys. Rev. Lett. **103**, 100403 (2009).

[18] L. F. Santos and M. Rigol, "Localization and the effects of symmetries in the thermalization properties of one-dimensional quantum systems", Phys. Rev. E **82**, 031130 (2010).

[19] G. Biroli, C. Kollath, and A. M. Läuchli, "Effect of rare fluctuations on the thermalization of isolated quantum systems", Phys. Rev. Lett. **105**, 250401 (2010).

[20] R. Steinigeweg, J. Herbrych, and P. Prelovšek, "Eigenstate thermalization within isolated spin-chain systems", Phys. Rev. E **87**, 012118 (2013).

[21] A. Pal and D. A. Huse, "Many-body localization phase transition", Phys. Rev. B **82**, 174411 (2010).

[22] E. Altman and R. Vosk, "Universal Dynamics and Renormalization in Many-Body-Localized Systems", Annu. Rev. Condens. Matter Phys. **6**, 383 (2015).

[23] R. Nandkishore and D. A. Huse, "Many-Body Localization and Thermalization in Quantum Statistical Mechanics", Annu. Rev. Condens. Matter Phys. **6**, 15 (2015).

[24] J. Z. Imbrie, V. Ros, and A. Scardicchio, "Local integrals of motion in many-body localized systems", Ann. Phys. **529**, 1600278 (2017).

[25] D. A. Abanin and Z. Papić, "Recent progress in many-body localization", Ann. Phys. **529**, 1700169 (2017).

[26] F. Alet and N. Laflorencie, "Many-body localization: An introduction and selected topics", Comptes Rendus Physique **19**, 498 (2018).

[27] M. Rigol, V. Dunjko, V. Yurovsky, and M. Olshanii, "Relaxation in a completely integrable many-body quantum system: an ab initio study of the dynamics of the highly excited states of 1D lattice hard-core bosons", Phys. Rev. Lett. **98**, 050405 (2007).

[28] A. C. Cassidy, C. W. Clark, and M. Rigol, "Generalized thermalization in an integrable lattice system", Phys. Rev. Lett. **106**, 140405 (2011).

[29] P. Calabrese, F. H. L. Essler, and M. Fagotti, "Quantum quench in the transverse-field Ising chain", Phys. Rev. Lett. **106**, 227203 (2011).

[30] F. H. L. Essler and M. Fagotti, "Quench dynamics and relaxation in isolated integrable quantum spin chains", J. Stat. Mech. **2016**, 064002 (2016).

[31] N. Shiraishi and T. Mori, "Systematic Construction of Counterexamples to the Eigenstate Thermalization Hypothesis", Phys. Rev. Lett. **119**, 030601 (2017).

[32] T. Mori and N. Shiraishi, "Thermalization without eigenstate thermalization hypothesis after a quantum quench", Phys Rev E **96**, 022153 (2017).

[33] H. Bernien, S. Schwartz, A. Keesling, H. Levine, A. Omran, H. Pichler, S. Choi, A. S. Zibrov, M. Endres, M. Greiner, V. Vuletić, and M. D. Lukin, "Probing many-body dynamics on a 51-atom quantum simulator", Nature **551**, 579 (2017).

[34] N. Shiraishi, "Connection between quantum-many-body scars and the Affleck–Kennedy–Lieb–Tasaki model from the viewpoint of embedded Hamiltonians", J. Stat. Mech. **2019**, 083103 (2019).

[35] S. Moudgalya, B. Andrei Bernevig, and N. Regnault, "Quantum Many-Body Scars and Hilbert Space Fragmentation: A Review of Exact Results", arXiv:2109.00548 [cond-mat.str-el].

[36] Z. Papić, "Weak ergodicity breaking through the lens of quantum entanglement", arXiv:2108.03460 [cond-mat.quant-gas].

[37] M. Serbyn, D. A. Abanin, and Z. Papić, "Quantum many-body scars and weak breaking of ergodicity", Nat. Phys. **17**, 675 (2021).

[38] R. Nandkishore, *Quantum scars and partial breaking of ergodicity*, http://dx.doi.org/10.36471/JCCM_April_2020_01.

[39] K. Bull, I. Martin, and Z. Papić, "Systematic Construction of Scarred Many-Body Dynamics in 1D Lattice Models", Phys. Rev. Lett. **123**, 030601 (2019).

[40] M. Schecter and T. Iadecola, "Weak Ergodicity Breaking and Quantum Many-Body Scars in Spin-1 XY Magnets", Phys. Rev. Lett. **123**, 147201 (2019).

[41] T. Iadecola, M. Schecter, and S. Xu, "Quantum many-body scars from magnon condensation", Phys. Rev. B **100**, 184312 (2019).

[42] S. Ok, K. Choo, C. Mudry, C. Castelnovo, C. Chamon, and T. Neupert, "Topological many-body scar states in dimensions one, two, and three", Phys. Rev. Research **1**, 033144 (2019).

[43] T. Iadecola and M. Schecter, "Quantum many-body scar states with emergent kinetic constraints and finite-entanglement revivals", Phys. Rev. B **101**, 024306 (2020).

[44] H. Zhao, J. Vovrosh, F. Mintert, and J. Knolle, "Quantum Many-Body Scars in Optical Lattices", Phys. Rev. Lett. **124**, 160604 (2020).

[45] K. Bull, J.-Y. Desaules, and Z. Papić, "Quantum scars as embeddings of weakly broken Lie algebra representations", Phys. Rev. B **101**, 165139 (2020).

[46] N. Shibata, N. Yoshioka, and H. Katsura, "Onsager's Scars in Disordered Spin Chains", Phys. Rev. Lett. **124**, 180604 (2020).

[47] S. Chattopadhyay, H. Pichler, M. D. Lukin, and W. W. Ho, "Quantum many-body scars from virtual entangled pairs", Phys. Rev. B **101**, 174308 (2020).

[48] B. Mukherjee, S. Nandy, A. Sen, D. Sen, and K. Sengupta, "Collapse and revival of quantum many-body scars via Floquet engineering", Phys. Rev. B **101**, 245107 (2020).

[49] A. Hudomal, I. Vasić, N. Regnault, and Z. Papić, "Quantum scars of bosons with correlated hopping", Communications Physics **3**, 99 (2020).

[50] K. Lee, R. Melendrez, A. Pal, and H. J. Changlani, "Exact three-colored quantum scars from geometric frustration", Phys. Rev. B **101**, 241111 (2020).

[51] C.-J. Lin, V. Calvera, and T. H. Hsieh, "Quantum many-body scar states in two-dimensional Rydberg atom arrays", Phys. Rev. B **101**, 220304 (2020).

[52] C.-J. Lin, A. Chandran, and O. I. Motrunich, "Slow thermalization of exact quantum many-body scar states under perturbations", Phys. Rev. Research **2**, 033044 (2020).

[53] S. Moudgalya, E. O'Brien, B. A. Bernevig, P. Fendley, and N. Regnault, "Large classes of quantum scarred Hamiltonians from matrix product states", Phys. Rev. B **102**, 085120 (2020).

[54] S. Moudgalya, N. Regnault, and B. A. Bernevig, "η-pairing in Hubbard models: From spectrum generating algebras to quantum many-body scars", Phys. Rev. B **102**, 085140 (2020).

[55] K. Mizuta, K. Takasan, and N. Kawakami, "Exact Floquet quantum many-body scars under Rydberg blockade", Phys. Rev. Research **2**, 033284 (2020).

[56] D. K. Mark and O. I. Motrunich, "η-pairing states as true scars in an extended Hubbard model", Phys. Rev. B **102**, 075132 (2020).

[57] S. Moudgalya, B. A. Bernevig, and N. Regnault, "Quantum many-body scars in a Landau level on a thin torus", Phys. Rev. B **102**, 195150 (2020).

[58] N. O'Dea, F. Burnell, A. Chandran, and V. Khemani, "From tunnels to towers: Quantum scars from Lie algebras and q-deformed Lie algebras", Phys. Rev. Research **2**, 043305 (2020).

[59] K. Pakrouski, P. N. Pallegar, F. K. Popov, and I. R. Klebanov, "Many-Body Scars as a Group Invariant Sector of Hilbert Space", Phys. Rev. Lett. **125**, 230602 (2020).

[60] P. A. McClarty, M. Haque, A. Sen, and J. Richter, "Disorder-free localization and many-body quantum scars from magnetic frustration", Phys. Rev. B **102**, 224303 (2020).

[61] J. Ren, C. Liang, and C. Fang, "Quasisymmetry Groups and Many-Body Scar Dynamics", Phys. Rev. Lett. **126**, 120604 (2021).

[62] D. Banerjee and A. Sen, "Quantum Scars from Zero Modes in an Abelian Lattice Gauge Theory on Ladders", Phys. Rev. Lett. **126**, 220601 (2021).

[63] H. Singh, B. A. Ware, R. Vasseur, and A. J. Friedman, "Subdiffusion and Many-Body Quantum Chaos with Kinetic Constraints", Phys. Rev. Lett. **127**, 230602 (2021).

[64] V. Karle, M. Serbyn, and A. A. Michailidis, "Area-Law Entangled Eigenstates from Nullspaces of Local Hamiltonians", Phys. Rev. Lett. **127**, 060602 (2021).

[65] J. Ren, C. Liang, and C. Fang, "Deformed Symmetry Structures and Quantum Many-body Scar Subspaces", arXiv:2108.07817 [cond-mat.str-el].

[66] H. Zhao, A. Smith, F. Mintert, and J. Knolle, "Orthogonal Quantum Many-Body Scars", Phys. Rev. Lett. **127**, 150601 (2021).

[67] H. Labuhn, D. Barredo, S. Ravets, S. de Léséleuc, T. Macrì, T. Lahaye, and A. Browaeys, "Tunable two-dimensional arrays of single Rydberg atoms for realizing quantum Ising models", Nature **534**, 667 (2016).

[68] P. Schauß, M. Cheneau, M. Endres, T. Fukuhara, S. Hild, A. Omran, T. Pohl, C. Gross, S. Kuhr, and I. Bloch, "Observation of spatially ordered structures in a two-dimensional Rydberg gas", Nature **491**, 87 (2012).

[69] A. Browaeys and T. Lahaye, "Many-body physics with individually controlled Rydberg atoms", Nat. Phys. **16**, 132 (2020).

[70] S. Ji, C. Ates, and I. Lesanovsky, "Two-dimensional Rydberg gases and the quantum hard-squares model", Phys. Rev. Lett. **107**, 060406 (2011).

[71] I. Lesanovsky, "Many-body spin interactions and the ground state of a dense Rydberg lattice gas", Phys. Rev. Lett. **106**, 025301 (2011).

[72] R. M. Nandkishore and M. Hermele, "Fractons", Annu. Rev. Condens. Matter Phys. **10**, 295 (2019).

[73] M. Pretko, X. Chen, and Y. You, "Fracton phases of matter", Int. J. Mod. Phys. A **35**, 2030003 (2020).

[74] A. Prem, J. Haah, and R. Nandkishore, "Glassy quantum dynamics in translation invariant fracton models", Phys. Rev. B **95**, 155133 (2017).

[75] S. Moudgalya, A. Prem, R. Nandkishore, N. Regnault, and B. A. Bernevig, "Thermalization and Its Absence within Krylov Subspaces of a Constrained Hamiltonian", in *Memorial Volume for Shoucheng Zhang* (WORLD SCIENTIFIC, Nov. 2020), pp. 147–209.

[76] F. Pietracaprina and N. Laflorencie, "Hilbert-space fragmentation, multifractality, and many-body localization", Ann. Phys., 168502 (2021).

[77] S. Pai and M. Pretko, "Dynamical Scar States in Driven Fracton Systems", Phys. Rev. Lett. **123**, 136401 (2019).

[78] A. Morningstar, V. Khemani, and D. A. Huse, "Kinetically constrained freezing transition in a dipole-conserving system", Phys. Rev. B **101**, 214205 (2020).

[79] K. Lee, A. Pal, and H. J. Changlani, "Frustration-induced emergent Hilbert space fragmentation", Phys. Rev. B **103**, 235133 (2021).

[80] L. Herviou, J. H. Bardarson, and N. Regnault, "Many-body localization in a fragmented Hilbert space", Phys. Rev. B **103**, 134207 (2021).

[81] C. M. Langlett and S. Xu, "Hilbert space fragmentation and exact scars of generalized Fredkin spin chains", Phys. Rev. B **103**, L220304 (2021).

[82] D. Hahn, P. A. McClarty, and D. J. Luitz, "Information dynamics in a model with Hilbert space fragmentation", SciPost Phys. **11**, 74 (2021).

[83] B. Mukherjee, D. Banerjee, K. Sengupta, and A. Sen, "Minimal model for Hilbert space fragmentation with local constraints", Phys. Rev. B **104**, 155117 (2021).

[84] J. P. Garrahan, P. Sollich, and C. Toninelli, "Kinetically constrained models", in *Dynamical Heterogeneities in Glasses, Colloids, and Granular Media* (Oxford University Press, Sept. 2010).

[85] J. P. Garrahan, R. L. Jack, V. Lecomte, E. Pitard, K. van Duijvendijk, and F. van Wijland, "First-order dynamical phase transition in models of glasses: an approach based on ensembles of histories", J. Phys. A **42**, 075007 (2009).

[86] P. Chleboun, A. Faggionato, and F. Martinelli, "Time scale separation in the low temperature East model: rigorous results", J. Stat. Mech. **2013**, L04001 (2013).

[87] H. Kim, M. C. Bañuls, J. I. Cirac, M. B. Hastings, and D. A. Huse, "Slowest local operators in quantum spin chains", Phys. Rev. E **92**, 012128 (2015).

[88] S. Gopalakrishnan, D. A. Huse, V. Khemani, and R. Vasseur, "Hydrodynamics of operator spreading and quasiparticle diffusion in interacting integrable systems", Phys. Rev. B **98**, 220303 (2018).

[89] S. Gopalakrishnan, "Operator growth and eigenstate entanglement in an interacting integrable Floquet system", Phys. Rev. B **98**, 060302 (2018).

[90] M. C. Bañuls and J. P. Garrahan, "Using Matrix Product States to Study the Dynamical Large Deviations of Kinetically Constrained Models", Phys. Rev. Lett. **123**, 200601 (2019).

[91] Z. Lan, M. van Horssen, S. Powell, and J. P. Garrahan, "Quantum Slow Relaxation and Metastability due to Dynamical Constraints", Phys. Rev. Lett. **121**, 040603 (2018).

[92] N. Pancotti, G. Giudice, J. I. Cirac, J. P. Garrahan, and M. C. Bañuls, "Quantum East Model: Localization, Nonthermal Eigenstates, and Slow Dynamics", Phys. Rev. X **10**, 021051 (2020).

[93] E. J. Heller, "Bound-State Eigenfunctions of Classically Chaotic Hamiltonian Systems: Scars of Periodic Orbits", Phys. Rev. Lett. **53**, 1515 (1984).

[94] M. V. Berry, "Quantum scars of classical closed orbits in phase space", Proc. R. Soc. Lond. A Math. Phys. Sci. **423**, 219 (1989).

[95] L. Bunimovich, "Dynamical billiards", Scholarpedia J. **2**, 1813 (2007).

[96] P. So, "Unstable periodic orbits", Scholarpedia J. **2**, 1353 (2007).

[97] C. J. Turner, J.-Y. Desaules, K. Bull, and Z. Papić, "Correspondence Principle for Many-Body Scars in Ultracold Rydberg Atoms", Phys. Rev. X **11**, 021021 (2021).

[98] A. A. Michailidis, C. J. Turner, Z. Papić, D. A. Abanin, and M. Serbyn, "Slow Quantum Thermalization and Many-Body Revivals from Mixed Phase Space", Phys. Rev. X **10**, 011055 (2020).

[99] W. W. Ho, S. Choi, H. Pichler, and M. D. Lukin, "Periodic Orbits, Entanglement, and Quantum Many-Body Scars in Constrained Models: Matrix Product State Approach", Phys. Rev. Lett. **122**, 040603 (2019).

[100] Y. Werman, "Quantum Chaos in a Rydberg Atom System", arXiv:2001.06110 [quant-ph].

[101] R. Orús, "A practical introduction to tensor networks: Matrix product states and projected entangled pair states", Ann. Phys. **349**, 117 (2014).

[102] J. C. Bridgeman and C. T. Chubb, "Hand-waving and interpretive dance: an introductory course on tensor networks", J. Phys. A **50**, 223001 (2017).

[103] R. Orús, "Tensor networks for complex quantum systems", Nature Reviews Physics **1**, 538 (2019).

[104] C.-J. Lin and O. I. Motrunich, "Exact Quantum Many-Body Scar States in the Rydberg-Blockaded Atom Chain", Phys. Rev. Lett. **122**, 173401 (2019).

[105] L. Hackl, T. Guaita, T. Shi, J. Haegeman, E. Demler, and I. Cirac, "Geometry of variational methods: dynamics of closed quantum systems", SciPost Phys. **9**, 48 (2020).

[106] P. Kramer and M. Saraceno, *Geometry of the Time-Dependent Variational Principle in Quantum Mechanics*, edited by P. Kramer and M. Saraceno (Springer, Berlin, Heidelberg, Apr. 1981).

[107] A. D. McLachlan, "A variational solution of the time-dependent Schrodinger equation", Mol. Phys. **8**, 39 (1964).

[108] P. A. M. Dirac, "Note on Exchange Phenomena in the Thomas Atom", Math. Proc. Cambridge Philos. Soc. **26**, 376 (1930).

[109] J. Frenkel, *Wave mechanics, advanced general theory*, Vol. 1 (Oxford, 1934).

[110] J. Haegeman, J. I. Cirac, T. J. Osborne, I. Pižorn, H. Verschelde, and F. Verstraete, "Time-dependent variational principle for quantum lattices", Phys. Rev. Lett. **107**, 070601 (2011).

[111] J. Haegeman, T. J. Osborne, and F. Verstraete, "Post-matrix product state methods: To tangent space and beyond", Phys. Rev. B **88**, 075133 (2013).

[112] L. Vanderstraeten, J. Haegeman, and F. Verstraete, "Tangent-space methods for uniform matrix product states", SciPost Phys. Lect. Notes, 7 (2019).

[113] J. Haegeman, C. Lubich, I. Oseledets, B. Vandereycken, and F. Verstraete, "Unifying time evolution and optimization with matrix product states", Phys. Rev. B **94**, 165116 (2016).

[114] J. Haegeman, M. Mariën, T. J. Osborne, and F. Verstraete, "Geometry of matrix product states: Metric, parallel transport, and curvature", J. Math. Phys. **55**, 021902 (2014).

[115] Y. Wu, "Time-dependent variational principle for mixed matrix product states in the thermodynamic limit", Phys. Rev. B **102**, 134306 (2020).

[116] A. Hallam, J. G. Morley, and A. G. Green, "The Lyapunov spectra of quantum thermalisation", Nat. Commun. **10**, 2708 (2019).

[117] E. Leviatan, F. Pollmann, J. H. Bardarson, D. A. Huse, and E. Altman, "Quantum thermalization dynamics with Matrix-Product States", arXiv:1702.08894 [cond-mat.stat-mech].

[118] C. Geng, H.-Y. Hu, and Y. Zou, "Differentiable Programming of Isometric Tensor Networks", arXiv:2110.03898 [quant-ph].

[119] B. Ponsioen, F. Assaad, and P. Corboz, "Automatic differentiation applied to excitations with projected entangled pair states", SciPost Phys. **12**, 6 (2022).

[120] C. Guo and D. Poletti, "Scheme for automatic differentiation of complex loss functions with applications in quantum physics", Phys. Rev. E **103**, 013309 (2021).

[121] C. Boeddeker, P. Hanebrink, L. Drude, J. Heymann, and R. Haeb-Umbach, "On the Computation of Complex-valued Gradients with Application to Statistically Optimum Beamforming", arXiv:1701.00392 [cs.NA].

[122] I. A. Luchnikov, M. E. Krechetov, and S. N. Filippov, "Riemannian geometry and automatic differentiation for optimization problems of quantum physics and quantum technologies", New J. Phys. **23**, 073006 (2021).

[123] H. Xie, J.-G. Liu, and L. Wang, "Automatic differentiation of dominant eigensolver and its applications in quantum physics", Phys. Rev. B **101**, 245139 (2020).

[124] B.-B. Chen, Y. Gao, Y.-B. Guo, Y. Liu, H.-H. Zhao, H.-J. Liao, L. Wang, T. Xiang, W. Li, and Z. Y. Xie, "Automatic differentiation for second renormalization of tensor networks", Phys. Rev. B **101**, 220409 (2020).

[125] G. Torlai, J. Carrasquilla, M. T. Fishman, R. G. Melko, and M. P. A. Fisher, "Wavefunction positivization via automatic differentiation", Phys. Rev. Research **2**, 032060 (2020).

[126] H.-J. Liao, J.-G. Liu, L. Wang, and T. Xiang, "Differentiable Programming Tensor Networks", Phys. Rev. X **9**, 031041 (2019).

[127] M. Hauru, M. Van Damme, and J. Haegeman, "Riemannian optimization of isometric tensor networks", SciPost Phys. **10**, 40 (2021).

[128] T. Mori, "Weak eigenstate thermalization with large deviation bound", arXiv:1609.09776 [cond-mat.stat-mech].

[129] E. Iyoda, K. Kaneko, and T. Sagawa, "Fluctuation Theorem for Many-Body Pure Quantum States", Phys. Rev. Lett. **119**, 100601 (2017).

[130] J.-Y. Desaules, F. Pietracaprina, Z. Papić, J. Goold, and S. Pappalardi, "Quantum many-body scars have extensive multipartite entanglement", arXiv:2109.09724 [quant-ph].

[131] V. Khemani, C. R. Laumann, and A. Chandran, "Signatures of integrability in the dynamics of Rydberg-blockaded chains", Phys. Rev. B **99**, 161101 (2019).

[132] C. J. Turner, A. A. Michailidis, D. A. Abanin, M. Serbyn, and Z. Papić, "Quantum scarred eigenstates in a Rydberg atom chain: Entanglement, breakdown of thermalization, and stability to perturbations", Phys. Rev. B **98**, 155134 (2018).

[133] S. Choi, C. J. Turner, H. Pichler, W. W. Ho, A. A. Michailidis, Z. Papić, M. Serbyn, M. D. Lukin, and D. A. Abanin, "Emergent SU(2) Dynamics and Perfect Quantum Many-Body Scars", Phys. Rev. Lett. **122**, 220603 (2019).

[134] C. J. Turner, A. A. Michailidis, D. A. Abanin, M. Serbyn, and Z. Papić, "Weak ergodicity breaking from quantum many-body scars", Nat. Phys. **14**, 745 (2018).

[135] M. Gutzwiller, "Quantum chaos", Scholarpedia J. **2**, 3146 (2007).

[136] L. Kaplan, "Scars in quantum chaotic wavefunctions", Nonlinearity **12**, R1 (1999).

[137] E. B. Bogomolny, "Smoothed wave functions of chaotic quantum systems", Physica D **31**, 169 (1988).

[138] R. Martinazzo and I. Burghardt, "Local-in-Time Error in Variational Quantum Dynamics", Phys. Rev. Lett. **124**, 150601 (2020).

[139] U. Schollwöck, "The density-matrix renormalization group in the age of matrix product states", Ann. Phys. **326**, 96 (2011).

[140] J. I. Cirac, D. Pérez-García, N. Schuch, and F. Verstraete, "Matrix product states and projected entangled pair states: Concepts, symmetries, theorems", Rev. Mod. Phys. **93**, 045003 (2021).

[141] S. Paeckel, T. Köhler, A. Swoboda, S. R. Manmana, U. Schollwöck, and C. Hubig, "Time-evolution methods for matrix-product states", Ann. Phys. **411**, 167998 (2019).

[142] U. Schollwöck, "The density-matrix renormalization group", Rev. Mod. Phys. **77**, 259 (2005).

[143] S. R. White, "Density matrix formulation for quantum renormalization groups", Phys. Rev. Lett. **69**, 2863 (1992).

[144] M. Fannes, B. Nachtergaele, and R. F. Werner, "Finitely correlated states on quantum spin chains", Commun. Math. Phys. **144**, 443 (1992).

[145] V. Zauner-Stauber, L. Vanderstraeten, M. T. Fishman, F. Verstraete, and J. Haegeman, "Variational optimization algorithms for uniform matrix product states", Phys. Rev. B **97**, 045145 (2018).

[146] H. N. Phien, G. Vidal, and I. P. McCulloch, "Infinite boundary conditions for matrix product state calculations", Phys. Rev. B **86**, 245107 (2012).

[147] S. R. White and A. E. Feiguin, "Real-time evolution using the density matrix renormalization group", Phys. Rev. Lett. **93**, 076401 (2004).

[148] G. Vidal, "Efficient classical simulation of slightly entangled quantum computations", Phys. Rev. Lett. **91**, 147902 (2003).

[149] C. Hubig, J. Haegeman, and U. Schollwöck, "Error estimates for extrapolations with matrix-product states", Phys. Rev. B **97**, 045125 (2018).

[150] D. A. Roberts, D. Stanford, and L. Susskind, "Localized shocks", J. High Energy Phys. **2015**, 51 (2015).

[151] M. C. Bañuls, J. I. Cirac, and M. B. Hastings, "Strong and weak thermalization of infinite nonintegrable quantum systems", Phys. Rev. Lett. **106**, 050405 (2011).

[152] H. Nakano, T. Shirai, and T. Mori, "Tensor network approach to thermalization in open quantum many-body systems", Phys Rev E **103**, L040102 (2021).

[153] T. Prosen and M. Znidaric, "Is the efficiency of classical simulations of quantum dynamics related to integrability?", Phys. Rev. E **75**, 015202 (2007).

[154] Y. Sinai, "Kolmogorov-Sinai entropy", Scholarpedia J. **4**, 2034 (2009).

[155] L. Tagliacozzo, T. R. de Oliveira, S. Iblisdir, and J. I. Latorre, "Scaling of entanglement support for matrix product states", Phys. Rev. B **78**, 024410 (2008).

[156] M. M. Rams, P. Czarnik, and L. Cincio, "Precise Extrapolation of the Correlation Function Asymptotics in Uniform Tensor Network States with Application to the Bose-Hubbard and XXZ Models", Phys. Rev. X **8**, 041033 (2018).

[157] H. Yang, H. Nakano, and H. Katsura, "Symmetry-protected topological phases in spinful bosons with a flat band", Phys. Rev. Research **3**, 023210 (2021).

[158] A. Abad, R. Barrio, and A. Dena, "Computing periodic orbits with arbitrary precision", Phys. Rev. E **84**, 016701 (2011).

[159] Y. Saiki, "Numerical detection of unstable periodic orbits in continuous-time dynamical systems with chaotic behaviors", Nonlinear Process. Geophys. **14**, 615 (2007).

[160] Y. Saiki and K.-I. Ishiyama, "RECOGNITION OF TRANSITION PATTERNS IN A BUSINESS CYCLE MODEL USING UNSTABLE PERIODIC ORBITS", Int. J. Bifurcat. Chaos **21**, 1203 (2011).

[161] J. Li, F. Li, and S. Todorovic, "Efficient Riemannian Optimization on the Stiefel Manifold via the Cayley Transform", in International Conference on Learning Representations (2020).

[162] G. Becigneul and O.-E. Ganea, "Riemannian Adaptive Optimization Methods", in International Conference on Learning Representations (2019).

[163] H. D. Tagare, *Notes on Optimization on Stiefel Manifolds*, `http://noodle.med.yale.edu/hdtag/notes/steifel_notes.pdf`.

[164] A. Edelman, T. A. Arias, and S. T. Smith, "The Geometry of Algorithms with Orthogonality Constraints", SIAM J. Matrix Anal. Appl. **20**, 303 (1998).

[165] P.-A. Absil, R. Mahony, and R. Sepulchre, *Optimization Algorithms on Matrix Manifolds* (Princeton University Press, USA, Dec. 2007).

[166] M. J. Kochenderfer and T. A. Wheeler, *Algorithms for Optimization* (MIT Press, Mar. 2019).

[167] J. Haegeman, *OptimKit: A blissfully ignorant Julia package for gradient optimization*, `https://github.com/Jutho/OptimKit.jl`.

[168] A. Meurer, C. P. Smith, M. Paprocki, O. Čertík, S. B. Kirpichev, M. Rocklin, A. Kumar, S. Ivanov, J. K. Moore, S. Singh, T. Rathnayake, S. Vig, B. E. Granger, R. P. Muller, F. Bonazzi, H. Gupta, S. Vats, F. Johansson, F. Pedregosa, M. J. Curry, A. R. Terrel, Š. Roučka, A. Saboo, I. Fernando, S. Kulal, R. Cimrman, and A. Scopatz, "SymPy: symbolic computing in Python", PeerJ Comput. Sci. **3**, e103 (2017).

[169] A. G. Baydin, B. A. Pearlmutter, A. A. Radul, and J. M. Siskind, "Automatic differentiation in machine learning: a survey", J. Mach. Learn. Res. **18**, 5595 (2017).

[170] A. Paszke, S. Gross, F. Massa, A. Lerer, J. Bradbury, G. Chanan, T. Killeen, Z. Lin, N. Gimelshein, L. Antiga, A. Desmaison, A. Kopf, E. Yang, Z. DeVito, M. Raison, A. Tejani, S. Chilamkurthy, B. Steiner, L. Fang, J. Bai, and S. Chintala, "PyTorch: An Imperative Style, High-Performance Deep Learning Library", in Advances in Neural Information Processing Systems, Vol. 32, edited by H. Wallach, H. Larochelle, A. Beygelzimer, F. d'Alché-Buc, E. Fox, and R. Garnett (2019).

[171] M. Abadi, P. Barham, J. Chen, Z. Chen, A. Davis, J. Dean, M. Devin, S. Ghemawat, G. Irving, M. Isard, M. Kudlur, J. Levenberg, R. Monga, S. Moore, D. G. Murray, B. Steiner, P. Tucker, V. Vasudevan, P. Warden, M. Wicke, Y. Yu, and X. Zheng, "TensorFlow: a system for large-scale machine learning", in Proceedings of the 12th USENIX conference on Operating Systems Design and Implementation, OSDI'16 (Nov. 2016), pp. 265–283.

[172] J. Bradbury, R. Frostig, P. Hawkins, M. J. Johnson, C. Leary, D. Maclaurin, G. Necula, A. Paszke, J. VanderPlas, S. Wanderman-Milne, and Q. Zhang, *JAX: composable transformations of Python+NumPy programs*, http://github.com/google/jax.

[173] M. Innes, "Don't Unroll Adjoint: Differentiating SSA-Form Programs", arXiv:1810.07951 [cs.PL].

[174] J. Bezanson, A. Edelman, S. Karpinski, and V. B. Shah, "Julia: A Fresh Approach to Numerical Computing", SIAM Rev. **59**, 65 (2017).

[175] S. R. White, "Density matrix renormalization group algorithms with a single center site", Phys. Rev. B **72**, 180403 (2005).

[176] C. Hubig, I. P. McCulloch, U. Schollwöck, and F. A. Wolf, "Strictly single-site DMRG algorithm with subspace expansion", Phys. Rev. B **91**, 155115 (2015).

[177] T. Kato, *Perturbation Theory for Linear Operators* (Springer, Berlin, Heidelberg, 1995).

[178] I. P. McCulloch, "From density-matrix renormalization group to matrix product states", J. Stat. Mech. **2007**, P10014 (2007).

[179] B. Pirvu, V. Murg, J. I. Cirac, and F. Verstraete, "Matrix product operator representations", New J. Phys. **12**, 025012 (2010).

[180] F. Fröwis, V. Nebendahl, and W. Dür, "Tensor operators: Constructions and applications for long-range interaction systems", Phys. Rev. A **81**, 062337 (2010).

[181] G. M. Crosswhite, A. C. Doherty, and G. Vidal, "Applying matrix product operators to model systems with long-range interactions", Phys. Rev. B **78**, 035116 (2008).

[182] G. M. Crosswhite and D. Bacon, "Finite automata for caching in matrix product algorithms", Phys. Rev. A **78**, 012356 (2008).

[183] F. Verstraete, J. J. García-Ripoll, and J. I. Cirac, "Matrix product density operators: simulation of finite-temperature and dissipative systems", Phys. Rev. Lett. **93**, 207204 (2004).

[184] L. Michel and I. P. McCulloch, "Schur Forms of Matrix Product Operators in the Infinite Limit", arXiv:1008.4667 [cond-mat.stat-mech].

[185] L. White, M. Abbott, M. Zgubic, J. Revels, A. Arslan, S. Axen, S. Schaub, N. Robinson, Y. Ma, G. Dhingra, willtebbutt, N. Heim, A. D. W. Rosemberg, D. Widmann, N. Schmitz, C. Rackauckas, R. Heintzmann, frankschae, K. Fischer, A. Robson, mattBrzezinski, A. Zhabinski, M. Besançon, P. Vertechi, S. Gowda, A. Fitzgibbon, C. Lucibello, C. Vogt, D. Gandhi, and F. Chorney, *JuliaDiff/ChainRules.jl: v1.17.0*, https://zenodo.org/record/5780080.

[186] Z.-Q. Wan and S.-X. Zhang, "Automatic Differentiation for Complex Valued SVD", arXiv:1909.02659 [math.NA].

[187] R. N. C. Pfeifer, J. Haegeman, and F. Verstraete, "Faster identification of optimal contraction sequences for tensor networks", Phys. Rev. E **90**, 033315 (2014).

[188] K. J. Maschhoff and D. C. Sorensen, "P_ARPACK: An efficient portable large scale eigenvalue package for distributed memory parallel architectures", in *Applied Parallel Computing Industrial Computation and Optimization*, Lecture notes in computer science (Springer Berlin Heidelberg, Berlin, Heidelberg, 1996), pp. 478–486.

[189] M. Giles, *An extended collection of matrix derivative results for forward and reverse mode automatic differentiation*, https://ora.ox.ac.uk/objects/uuid:8d0c0a29-c92b-4153-a1d2-38b276e93124.